Geoinspired syntheses of materials and nanomaterials

David Portehault, Isabel Gómez-Recio, Marzena Baron, Valentina Musumeci, Cyril Aymonier, Virgile Rouchon, Yann Le Godec

REVIEW ARTICLE

Geoinspired syntheses of materials and nanomaterials

David Portehault, *[a] Isabel Gómez-Recio, [a] Marzena A. Baron, [a] Valentina Musumeci, [b] Cyril Aymonier, [b] Virgile Rouchon [c] and Yann Le Godec [d]

DOI: 10.1039/XXXXX

The search for new materials is intimately linked to the development of synthesis methods. In the current urge for the sustainable synthesis of materials, taking inspiration from Nature's ways to process matter appears as a virtuous approach. In this review, we address the concept of geoinspiration for the design of new materials and the exploration of new synthesis pathways. In geoinspiration, materials scientists take inspiration from the key features of various geological systems and processes occurring in nature, to trigger the formation of artificial materials and nanomaterials. We discuss several case studies of materials and nanomaterials to highlight the basic geoinspiration concepts underlying some synthesis methods: syntheses in water and supercritical water, thermal shock syntheses, molten salt synthesis and high pressure synthesis. We show that the materials emerging from geoinspiration exhibit properties differing from materials obtained by other pathways, thus demonstrating that the field opens up avenues to new families of materials and nanomaterials. This review focuses on synthesis methodologies, by drawing connections between geosciences and materials chemistry, nanosciences, green chemistry, and environmental sciences.

[a] *Sorbonne Université, CNRS, Laboratoire Chimie de la Matière Condensée de Paris (CMCP), 4 place Jussieu, 75005 Paris, France. E-mail: david.portehault@sorbonne-universite.fr*
[b] *Univ. Bordeaux, CNRS, Bordeaux INP, ICMCB, UMR 5026, F-33600 Pessac, France*
[c] *IFP Energies nouvelles (IFPEN), Rond point de l'échangeur de Solaize – BP 3, 69360 Solaize, France*
[d] *Sorbonne Université, CNRS, MNHN, IRD, Institut de Minéralogie, de Physique des Matériaux et de Cosmochimie (IMPMC), 4 place Jussieu, F-75005, Paris, France*

David Portehault

David Portehault is research director at the French National Centre for Scientific Research (CNRS) and at the Laboratory of Condensed Matter of Paris (LCMCP) hosted by Sorbonne University. He obtained his PhD in chemistry of materials at University Pierre and Marie Curie in 2008. He then became a senior postdoctoral fellow at the Max Planck Institute for Colloids and Interfaces until 2010, when he got appointed by the CNRS. He received the 2019 EuChemS Lecture Award and was granted a European Research Council Consolidator Grant the same year. His main current research topic is the exploration of new synthesis pathways at the edge of solid-state chemistry and solution chemistry, especially molten salts and aqueous chemistry, to discover original nanomaterials for energy-related properties, focused on electrocatalysis.

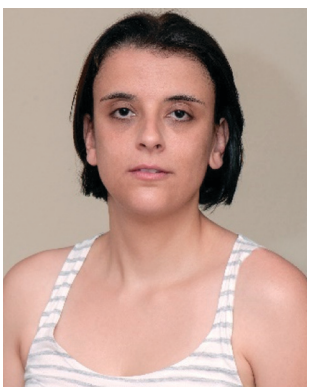

Isabel Gómez-Recio

Isabel Gómez Recio is a post-doctoral researcher of the Centre National de la Recherche Scientifique (CNRS), at the Laboratory Chimie de la Matière Condensée de Paris (LCMCP), hosted by Sorbonne Université. Her current research is focused on the synthesis of nanoparticles in liquid media, non-classical crystallization pathways as well as conventional and in situ electron microscopy. She obtained her PhD in 2018 at Universidad Complutense de Madrid (UCM) where she focused on synthesis and characterization of manganese oxide catalysts.

1. Introduction

Mankind is facing ecological crisis and needs to bring medicine, building engineering, information and communication technologies, among others, to the next level. The actual range of known materials has not proved to be sufficient to meet the demands emerging from these fields, thus calling for further exploration of new materials with specific properties. The range of solids that we can achieve is intimately linked to their synthesis processes. These methods encompass processes in the solid-state as in conventional solid-state chemistry, in the vapor-state such as vapor deposition processes, and in the liquid-state as in colloidal syntheses. This plethora of synthesis approaches however includes many procedures with a significant environmental impact. This has driven the emergence of low temperature solvent-free processes, such as mechanochemical synthesis, and the search for liquid media free of organic moieties.

Looking for alternative synthesis media and for novel ways to trigger chemical reactions also offers original reaction pathways, prone to deliver new solids and materials. In this sense, bioinspiration has proved to be a fruitful innovation

Marzena A. Baron

Marzena Anna Baron is a postdoctoral researcher of the Centre National de la Recherche Scientifique (CNRS), at the Laboratory Chimie de la Matière Condensée de Paris (LCMCP), hosted by Sorbonne Université. Her current research is focused on synthesis of geomaterials in link with nanoscience synthesis in liquid media, non-classical crystallization pathways as well as electron microscopy and synchrotron-based methods. She obtained her PhD in 2017 at University of Oslo in collaboration with University of Bristol, where she focused on high pressure and high temperature experimental research devoted to understanding lower mantle structure, composition and evolution.

Valentina Musumeci

Valentina Musumeci graduated in Condensed Matter Physics at the University of Catania in 2017. With her work on supercritical hydrothermal flow synthesis of calcium silicate hydrate nanominerals for applications in cement-based materials in the groups of Cyril Aymonier (ICMCB, Bordeaux) and the group of Dr. Jorge Sanchez Dolado (CFM, San Sebastian), she earned a PhD in Physical Chemistry of Condensed Matter from the University of Bordeaux and the University of Basque Country in 2021. Currently, she is working as a postdoctoral researcher in a project supported by CNRS, Technological Institute FCBA and Région Nouvelle-Aquitaine. Her research interests focus on nanostructured materials in respect of their syntheses, processing and applications.

Cyril Aymonier

Cyril Aymonier is senior CNRS researcher at the ''Institut de Chimie de la Matière Condensée de Bordeaux (ICMCB)''. He obtained his PhD in chemical engineering from University of Bordeaux (2000) where he focused on supercritical water oxidation of wastewater. He did a postdoctoral stay in Freiburg (2000–2002, Germany) where he developed novel approaches to design hybrid organic/inorganic nanoparticles. His current research interests are (i) the study of the chemistry, nucleation and growth mechanisms in supercritical fluids applied to the design of advanced nanostructured materials, (ii) the study of materials recycling using supercritical fluids and (iii) the development of the associated supercritical fluids-based technologies. He received the CNRS bronze medal (2011) and the Roy-Somiya award (2021) for his scientific achievements.

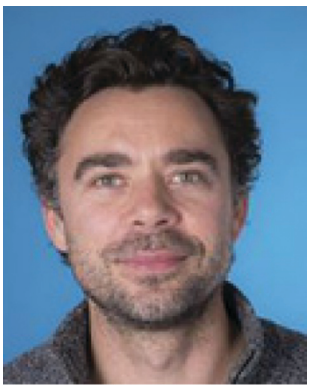

Virgile Rouchon

Virgile Rouchon obtained his PhD in 2008 in Earth Sciences at University Paris Sud – Orsay, where he developed geochemical proxies for evaluating the terrestrial environments coeval with the emergence of Life. He obtained a position at IFP Energies Nouvelles in 2008 where he focused his research in developing techniques in gas geochemistry for investigating the influence of non-hydrocarbon volatiles on sedimentary basins. Since 2018, he evolved towards materials sciences by taking over the electron microscopy lab of IFPEN, developing research in the fields of functional nanomaterials characterization.

field both in the discovery of new materials and their synthesis routes.[1] Hence, bioinspired materials show what a great source of inspiration Nature is.

Other natural events not involving biology can inspire the search for materials. In particular, the genesis of rocks can rely only on physicochemical processes. Just like bioinspiration differs from biomimetics in the sense that it does not search for precise replication of biological systems, we define *geoinspiration* as the development of materials and synthesis pathways by taking inspiration from the key features of geological systems. Geoinspiration differs from *geomimetics*, which aims at replicating whole sets of geological conditions.

Geoinspiration complements bioinspiration by largely extending the set of synthesis conditions and then by providing the frame to discover new materials. While the adjectives *geomimetic* and *geoinspired* appear seldomly in recent reports[2–4] in an interchangeable way, the relationship between some current synthesis methods and geological conditions is most of the time unnoticed. In fact a number of existing methods could actually be coined as geoinspired syntheses. For instance, molten salts emerge as liquid media for the synthesis of inorganic nanomaterials,[5,6] but their natural occurrence and importance in the growth of gems[7,8] are most of the time not suspected. This connection between state-of-the-art methods for materials, especially nanomaterials, and the processes occurring at geological timescales can inspire further development of synthesis protocols. Moreover, taking inspiration from geology can also be a fruitful approach to search for synthesis methods with low environmental cost.

In this review, we will show how geoinspiration triggers the synthesis of artificial materials, and especially nanomaterials, with new functions. To do so, we will use case-studies of (nano)materials to discuss the basic geoinspired concepts underlying some synthesis methods, the ways to control reaction pathways and the original properties that emerge from these routes. The materials discussed herein exhibit properties differing from not only naturally occurring materials but also from materials obtained by other pathways, thus showing that the field opens up avenues to new families of materials and nanomaterials. This review focuses on synthesis methodologies, by drawing connections between geoinspiration and materials chemistry, nanosciences, green chemistry, and environmental sciences. We then hope to raise awareness of geoinspiration to chemists and thus provide impetus to materials syntheses.

We specifically highlight some of the most important relationships between geological phenomena and chemical syntheses of materials (Fig. 1). The involved physicochemical conditions pertain to liquid mediated chemical reactions with aqueous and supercritical hydrothermal media, but also with thermal shocks and molten salt media. The last part of this review is more dedicated to solid-phase transformations, especially those occurring under high pressures and temperatures. Section 2 sets the stage by describing some main aspects of geological conditions. Each section from 3 to 7 is written with a focus on one synthesis method (Fig. 1) and with the aim of raising connections between different methods through their relations with geoscience. For the readers more interested in a given method, each of these sections can also be read independently from the others and then can be considered as a focused review on a specific synthesis approach.

2. Geology basics

Before discussing geoinspired synthesis methods, it is informative to draw the outline of geological events. The Earth's interior and surface are actually a dynamic material synthesis laboratory. They encompass various scales of time and space, gather an extreme variety of chemical environments, and are driven and stimulated by essentially all physical forces. These conditions have promoted a library of inorganic–organic chemical reactions that eventually led to the appearance of life. Across its 4.5 billion-year history, the Earth has generated very stable environments at the timescale of humanity and beyond. In geoinspiration, we draw from natural conditions some guide-

Yann Le Godec

Yann Le Godec is CNRS research director at the "Institut de Minéralogie, de Physique des Matériaux et de Cosmochimie" (IMPMC) hosted by Sorbonne University. He is an experienced user of large-scale instruments (synchrotrons and neutrons sources) for high-pressure research. During last years, he has used high pressure to synthesize and patent new materials with advanced mechanical and physical properties. He has been also leading in the development of original in situ high pressure-high temperature diffraction techniques, both for X-rays and neutron studies. He was also the president of the French "High Pressure Network" in France, a multidisciplinary network of approximately 250 scientists and engineers from all scientific departments of the CNRS. For his various studies, he received the CNRS "bronze medal" Award.

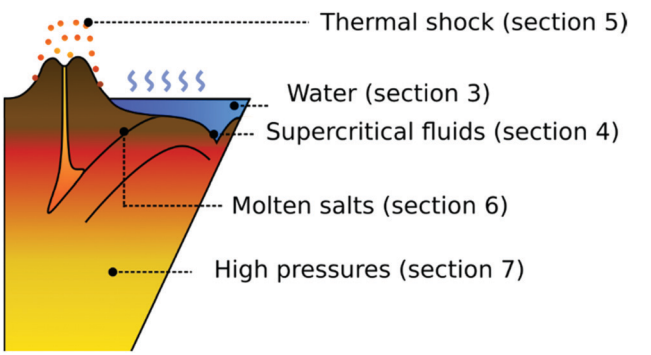

Fig. 1 Scheme of the geoinspired conditions discussed in this review for materials synthesis.

lines that help in identifying suitable conditions for materials synthesis. A system consisting of physicochemical conditions naturally occurring in the geosphere is not basically replicated at the laboratory scale, but it is broken down into its essential components from which only the parts required to synthesize the materials of interest are retained. Herein we underline how scientists can use these – sometimes unsuspected – relationships between geological and laboratory conditions to develop new materials and nanomaterials, in particular.

The Earth is composed of four main reservoirs, or envelopes, organized concentrically from the center to the periphery: the core, the mantle, the crust and the atmosphere (Fig. 2). This structure stabilized across the Hadean–Archean Eons some 4 billion years ago through a global scale transformation resulting from chemical and physical differentiation of the Earth's primordial matter. These planetary formation processes have involved mechanisms that are known and employed historically in the chemical sciences and industries for synthesizing materials, such as melting, vaporisation, precipitation, dissolution, and phase segregation. These elementary steps have been stimulated by a strong wholescale convection which has, at different scales of time and space, segregated, stabilized and destabilized very distinct and remarkable chemical environments representative of the four main envelopes of the Earth. In order for the reader to grasp the prevailing processes at the origin of and affecting these reservoirs, a short description of the most representative of them is provided in the next paragraphs.

The three solid envelopes of the Earth are chemically distinct and formed of different dominant mineral phases, assembled in typical rock types, so-called lithologies.

The crust, on which we are standing, forms essentially all continents (continental crust) and the ocean floor (oceanic crust). The crust concentrates chemical elements considered as ''lithophiles'', which are a large group of elements that were expelled from the mantle as a result of repeated and superimposed partial melting of the mantle rocks and extraction of the lower melting-point elements contained in the melt, in the course of magmatic events. The continental crust, which has formed over a billion years as a result of cumulative succession of tectonic accretion events at subduction or collision zones, is composed dominantly of silicon and aluminium oxides, the ''sialic crust'' (for silicon and aluminium), together with a good proportion of alkalis (Na and K) and less refractory metals such as Fe and Ti in minor abundance. The major minerals of the sialic crust are feldspar, quartz, and various Fe-rich or Fe-poor micas (biotite and muscovite), which has given rise to another nickname for the continental crust, the ''felsic crust'', as the typical mineral association of granites. The oceanic crust formed as the result of cooling and re-crystallizing mantle melts that contain magnesium and iron in high proportion (the ''mafic'' crust, for magnesium and iron) incorporated in mostly silicate minerals, such as olivine and pyroxenes, the major minerals of basalts.

The Earth's mantle, which is the largest envelope of the Earth both in mass and volume, is composed of the so-called ''ultra-mafic'' rocks, of which the most common rock-type in the upper mantle is peridotite, composed of mainly olivines and pyroxenes closest to their Mg-rich end-members as compared to the ones of the oceanic crust. The mantle lithologies undergo several phase transitions with increasing pressures and temperatures, which had been first observed by geophysical methods (*e.g.* seismic tomography) and then reproduced and understood in the laboratory experiments under elevated pressure and temperature conditions. At 410 km depth (15 GPa), the mantle transition zone starts with the first phase transition of olivine to wadsleite followed by ringwoodite at 550 km/19 GPa. The lower mantle starts below 670 km depth (24 GPa) where a major phase boundary opens the stability field of the most common mineral of the Earth: bridgmanite $(Mg,Fe)SiO_3$. The lower mantle is often referred to as pyrolytic in composition with minor contribution of ferropericlase and calcium perovskite. Geophysical observations indicate that the lower mantle is rather homogeneous, despite regions of recycling of oceanic plates where basaltic lithologies undergo subduction. At the lowermost part, the mantle interacts with the core with a steep temperature gradient where major lower mantle heterogeneities can be found.

The core is the sole envelope of the Earth that is dominantly chemically reduced. It is composed of Fe–Ni alloys in the inner core, and of their molten equivalents in the outer core. The Earth's outer core and inner core exhibit a density deficit relative to pure iron, attributed to the presence of substantial amounts of light elements, of which most potential candidates are silicon,

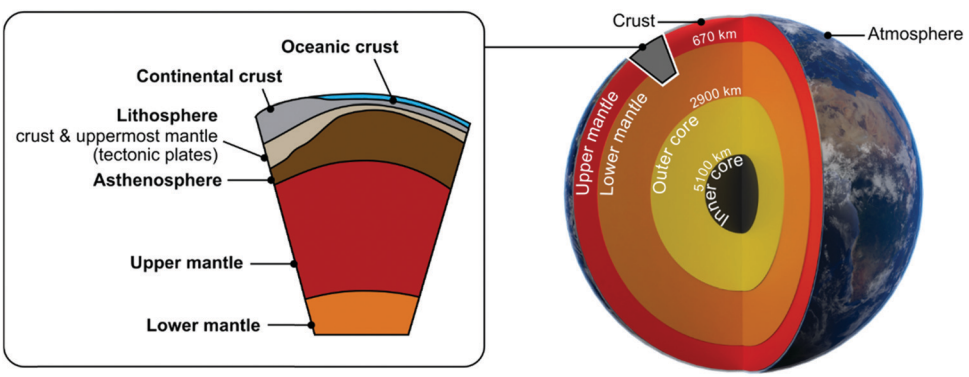

Fig. 2 Internal structure of the Earth. Inspired by ref. 9. The right panel has been created from the original Earth globe file from North.star (CC-BY 3.0).[10]

sulfur, oxygen, carbon and/or hydrogen. Current knowledge on the Earth's core[11] and on the core formation, mantle differentiation and properties of their constituents[12] has been reviewed recently.

It is worth noting that minerals are composed of an extremely large variety of chemical elements from major (0.1 > wt%), minor to trace (0.01 < wt% < 0.1) and ultra-trace (< 0.01 wt%) contents. Hence, the concept of "elemental purity" that is usually pursued in laboratory materials synthesis is hardly achieved in the natural formation of minerals. Although they may not constrain thermodynamic phase diagrams, these chemical impurities may play important roles, such as chemical buffers or catalysts.

Chemical buffering of the redox conditions in the various chemical environments described above is strong and mainly relies on the abundance and phase stability of elements capable of multiple oxidation states such as Fe, S and Mn. These elements modulate the fugacity of O_2 which is a conventional expression of the redox potential of terrestrial environments. Alternatively, the fugacity of H_2 may be employed under more reducing conditions. Redox buffer minerals have been defined as a representative or analog to the existing redox conditions in different terrestrial environments. The O_2 fugacity $f(O_2)$ of these buffers can be expressed as a function of temperature (Fig. 3A), and then phase diagrams can be drawn. The quartz-hematite and the quartz-fayalite-magnetite buffers define the most common $f(O_2)$ ranges existing in the crust and uppermost mantle. These buffers are a reference for displaying the redox state of multiple valence elements (Fig. 3B):

$$2Fe_3O_4 + 0.5O_2 = 3Fe_2O_3 \text{ (Hematite-magnetite)} \quad (1)$$

$$3Fe_2SiO_4 + O_2 = 2Fe_3O_4 + 3SiO_2 \text{ (Quartz-fayalite-magnetite)} \quad (2)$$

The fluids associated with the rocks in their porous volume make an essential contribution to the chemistry of natural systems as essential reactants, mass transport media for solvated ionic species, organic molecules and complexes. They are also heat carriers as well as pressure buffers. These fluids are dominantly aqueous in most of the liquid water stability regions on Earth where it is ubiquitous. Other major fluid components may be dominant in more local environments, such as hydrocarbons in gas and/or liquid states in sedimentary basins, gaseous or supercritical CO_2 in magmatic systems and deep crustal or mantle rocks. These three major fluid components tend to interact together in complex multiple phases and immiscible systems. They also interact strongly with their hosting rocks through mineral alteration processes governed by pH, redox and temperature (pressure) destabilization, which are discussed latter in Section 3 for materials synthesis. In aqueous media, pH buffering, as for redox buffering, is mainly driven by the rock forming minerals together with the composition of the surrounding fluid (single phase liquid or two-phase gas-liquid system). pH buffering is operated by most favorable hydration/dehydration reactions of the main oxide phases in the rock, such as for a large portion of the sialic crust:

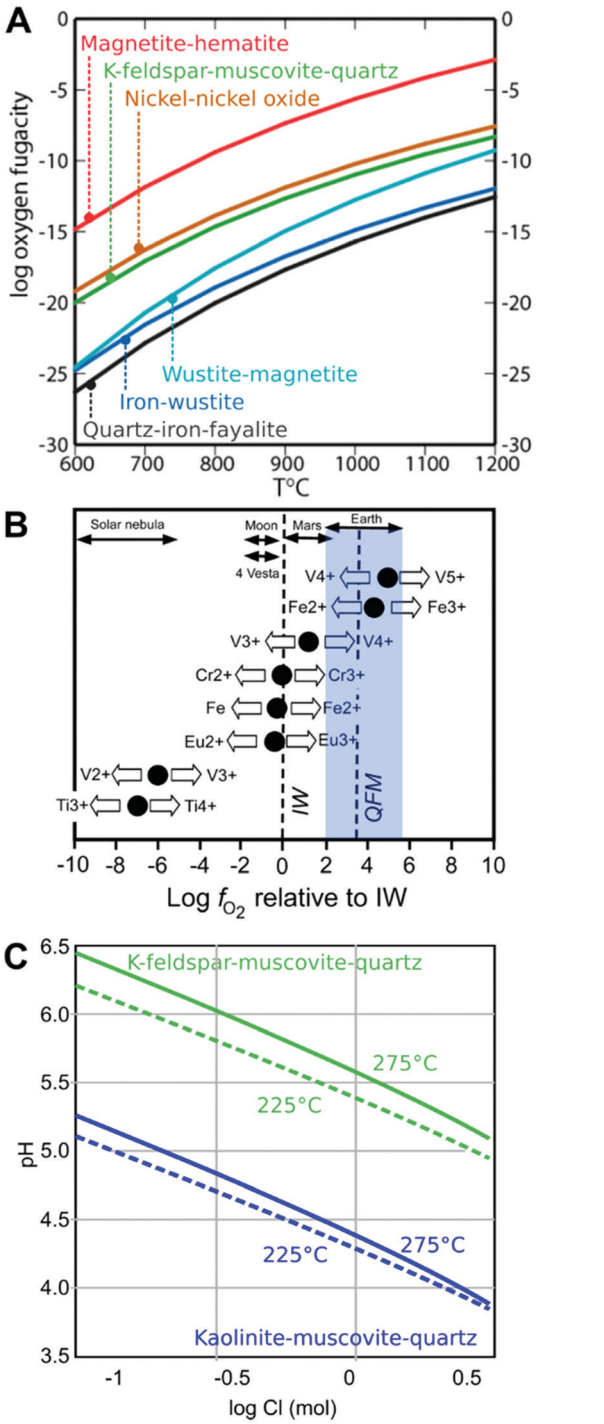

Fig. 3 (A) $f(O_2)$ *versus* temperature plot of the representative mineral redox buffers suitable for describing various terrestrial environments. Adapted with permission of De Gruyter from ref. 13. (B) Valence of different chemical elements as a function of the redox potential plotted in $f(O_2)$ relative to the iron-wustite buffer. The blue area corresponds to Earth conditions. Adapted with permission of the Mineralogical Society of America from ref. 14 and 15. (C) Example of the pH buffering ranges in the continental crust as a function of the fluid's chloride content for assemblages K-feldspar-muscovite-quartz and kaolinite-muscovite-quartz as a function of fluid chlorinity (log[Cl]) at 275 and 225 °C and at pressures on the boiling curve of water. Inspired by ref. 16.

$$3KAlSi_3O_8 + 2H^+ = KAl_3Si_3O_{10}(OH)_2 + 6SiO_2 + 2K^+$$

Hence, the K^+/H^+ composition of the coexisting fluid can be driven by charge compensating anions in the fluid (typically chlorides or bicarbonates) and by the local temperature (Fig. 3C). Again, this process is employed in aqueous materials synthesis discussed in Section 3.

The ranges of pressures and temperatures in the Earth's systems are represented with the lithostatic and geothermal gradients, which express the weight of the column of a rock as a function of depth, and the temperature gradient in a given geological context. Fig. 4A displays the generally accepted lithostatic and geothermal gradients across the different reservoirs mentioned above.[17] Two additional domains are indicated. The first one is the ocean domain, and the second one is the ''transient'' domain representing mantle intrusions in the crust and subaerial magmatic structures (volcanoes). One finds the expected correlation between pressure and temperature where the concept of ''the deeper the hotter'' generally stands for most of the Earth's domains, except for the oceans and the transient domain. The phase diagram of water is superimposed on this pressure–temperature diagram. Water, which is stable in its liquid state from atmospheric down to crustal conditions, is supercritical at deeper levels, as observed in some of the deepest hydrothermal vents detected (Fig. 4A).

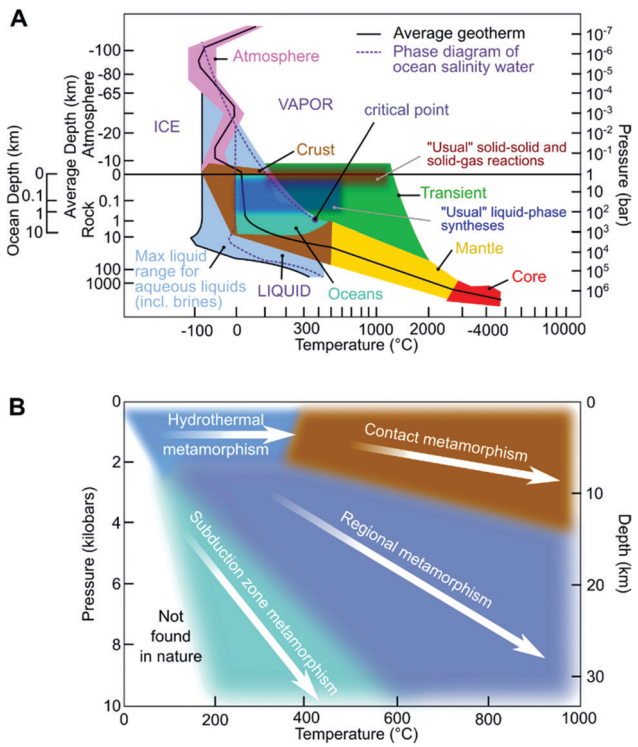

Fig. 4 (A) Pressure–temperature–depth (altitude) relationships on Earth. The different ranges corresponding to the four envelopes of the Earth, with complementary oceanic and transient domains. The phase diagram of water is superimposed. (B) The different domains of metamorphism in a temperature–pressure/depth space.

Besides the large-scale gradients of pressure and temperature on Earth, more localized conditions may induce strong temperature and/or pressure anomalies in geological media (Fig. 4A and B). This results in metamorphic rocks, which are formed from pre-existing rocks that undergo structural changes in response to not only the modifications of temperature, pressure, and differential stress, but also the contact with hydrothermal fluids. Four of these more localized environments are (i) magmatic systems, (ii) hydrothermal systems, (iii) seismic events, and (iv) meteorite impacts. Magmatic systems exist whenever a melt is expelled outside of its pyrolith into a host rock. The magma injection induces a sudden heat input together with a potential drastic chemical imbalance for the host rock, which subsequently undergoes alteration in a closed or open system, leading to the so-called contact metamorphism (Fig. 4B).[18] Such steep heating and cooling profiles are directly involved in recent materials synthesis approaches, highlighted in Section 5 (Fig. 1). Hydrothermal metamorphism occurs in hydrothermal systems, which for geologists are created when ''water is hot''. This implicitly points to systems where the temperature of the fluids is higher than that of the host rock (geotherm temperature). These conditions are generally associated with the periphery of a magmatic system or with peculiar deep convection of surface fluids. Hydrothermal systems are usually open. Extensive dissolution and reprecipitation occur in hydrothermal fluids, promoted by temperature, which can destabilize minerals and the host rocks by bringing them into other areas of the phase diagrams. Again, these processes are among the foundations of aqueous hydrothermal (Section 3) and supercritical (Section 4) materials synthesis (Fig. 1). Hydrothermal systems, according to the chemist's definition, relate to conditions where the temperature of a chemical system containing water is higher than the boiling point at ambient pressure.[19] While the geosciences and chemistry definitions diverge, both relate to the physical and chemical roles of water at high temperature in achieving specific reaction conditions. Seismic events and meteorite impacts are extremely fast phenomena involving an instantaneous release of tremendous pressure on geological media. Such a dramatic transient increase in pressure can be related to mechanochemistry, as suggested by Bolm *et al.*[20] who investigated mechanochemistry as a way to initiate prebiotic transformations for the generation of biogenic molecules, especially α-amino acids through α-aminonitriles. This relationship between mechanochemistry and especially meteorite impacts was further drawn by Huskić and Friščić who synthesized metal organic frameworks (MOFs) by using mechanochemistry.[21] These authors highlighted the existence of naturally occurring MOFs and questioned their formation mechanisms. Molten salts also belong to localized environments found on Earth, where evaporites form at the base of high salinity basins (continental or marine) and become molten reaction media, where some gems can crystallize.[7,8] These media are discussed from the perspective of materials synthesis in Section 6, whereas in Section 7, we will draw on the role of a large range of pressures relevant in geoscience for the advancement of materials science (Fig. 1).

3. Thermal and hydrothermal conditions: soft chemistry

3.1. Interplay between aqueous geological processes and materials synthesis by soft chemistry

Water is an essential ingredient in the dynamic nature of terrestrial environments, both as a ubiquitous reactant and as a powerful solvent and mass transport medium. The link between materials synthesis in water and geological processes is direct, as well as the basis of aqueous chemistry for materials and nanomaterials synthesis. Hence, interested readers are encouraged to refer to prominent reports on this topic.[22] In particular, the crystallization processes of a number of transition metal oxides and sulfides, clays, zeolites, as well as metal organic frameworks have already been discussed by drawing parallels with the natural processes.[21] For chemists, hydrothermal synthesis is the formation of a solid in the presence of an aqueous medium above 100 °C and 1 atm. By extension, it also often covers the lower temperature range below 100 °C.[23–26] The term "hydrothermal" was first used in the XIX century by the British geologist Sir Roderick Murchison to describe the mimicking of natural and geothermal reactions of water at elevated temperatures and pressures, which enabled the formation of numerous minerals and rocks.[23] In 1845, the hydrothermal method was employed by E. T. Schafthual to produce fine particles of quartz.[27] Afterwards, the manufacturing process was largely exploited for producing numerous clays, silicates, oxides and hydroxide minerals. By 1900, more than 150 mineral species were synthesized including zeolites, large single quartz crystals, and diamond.[28,29] The power of the hydrothermal process as a tool to synthesize a broad range of naturally occurring minerals as man-made crystals has been highlighted in an exhaustive review by Morey and Niggli in as early as 1913.[29] The influence of several parameters, such as the pH, temperature, type and compositions of starting materials is now well rationalized.[22,30] Low temperature aqueous and hydrothermal syntheses are now well recognized for the design of a wide range of materials.

Herein, we want to stress briefly the recognized role of these experimental conditions in the structural, morphological and textural features of materials synthesized in liquid water. We take this knowledge as a foundation to highlight new trends that are currently explored for predicting reaction mechanisms. To highlight these approaches, we take the case study of manganese oxides, which provide an interesting framework to interrogate the possibility of predicting the conditions of the synthesis of metastable materials and nanomaterials.

Over 30 manganese-based crystalline and amorphous substances have been found on the Earth's surface. In contrast to iron, which is usually found as silicates in sediments, manganese is mainly fixed as manganese oxides. Manganese deposits are especially found in ocean crust nodules and form through two main pathways: abiotic oxidation at the ocean floor and biogenic processes induced by fungi and bacteria. Both processes are sensitive to pH, temperature and dissolved manganese concentration, thus impacting oxide nucleation and growth.[31]

Manganese in minerals is present in different oxidation states and usually accompanied by other cations (*i.e.* Na^+, K^+, Rb^{2+}, Mg^{2+}, Ca^{2+}, *etc.*) and water molecules, giving rise to various crystallographic structures. In most cases, MnO_2 polymorphs are built from $[MnO_6]$ octahedral units, which share corners or edges. They can be divided into three categories, all of them naturally occurring: 1D tunnel, 2D layer and 3D mesh (not shown) structures. Representative 1D and 2D structures are shown in Fig. 5. α-MnO_2, β-MnO_2, and γ-MnO_2 possess $(1 \times 1) \times (2 \times 2)$, (1×1) and $(1 \times 1) \times (1 \times 2)$ $[MnO_6]$ tunnel structures, respectively. ε-MnO_2 is an intergrowth of β- and γ-MnO_2. δ-MnO_2 belongs to 2D layered structures, while λ-MnO_2, with a spinel structure, is a 3D (1×1) mesh structure.[32,33] The α and δ polymorphs actually contain foreign species: water molecules and usually alkali or alkaline earth cations. The 2×2 large tunnels (4.6 Å) of the α polymorph can accommodate *e.g.* K^+, Ca^{2+}, Na^+, Mg^{2+}, Ba^{2+} or Pb^{2+}, while the smaller (1×1) tunnel can only host small cations such as Li^+ and H^+. The δ-MnO_2 layered structure can accommodate a vast number of metal cations and water molecules in its interlayer space, varying from 7 to 10 Å.[31,34]

Manganese oxides are studied not only as part of soils and sediments, but also because of their properties for heterogeneous catalysis in environmental remediation,[31,33,35] as supercapacitors,[36,37] and battery electrodes.[38] Control of polymorphism is important to adjust these properties. For instance, α-MnO_2 is active for the selective catalytic reduction of NO and N_2O,[39] while β-MnO_2 is active for methylene blue[40] and H_2O_2 decomposition[41]. Zhu *et al.*[42] measured the catalytic activity of MnO_2 nanorods for CO oxidation in the order α ≈ δ > γ > β-MnO_2. The particle morphology also impacts the catalytic properties of manganese oxides, by modifying

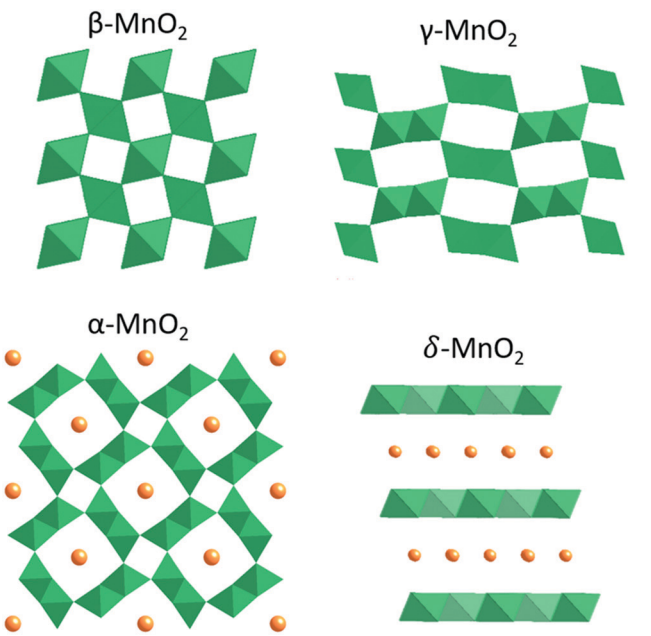

Fig. 5 Crystallographic structures of α-, β-, γ- and δ-MnO_2, showing the structural cavities built from MnO_6 octahedra.

the nature and amount of adsorption sites.[43] For instance, the particle morphology modifies the low temperature reducibility as well as the catalytic performance for toluene removal, with the following trend: nanorods > nanotubes > nanowires.[44] Therefore, it is necessary to develop methods for phase and morphology selective synthesis. We focus herein on structural control, for which significant advances in predictions have been made during the last few years.

Overall, hydrothermal synthesis is challenging in systems with rich polymorphism. This complexity originates from the non-equilibrium nature of low temperature crystallization for which different metastable phases are in competition, thus leading to complex crystallization pathways.[45]

3.2. Predicting structural evolutions through extended Pourbaix diagrams: the role of redox, acid–base conditions and particle size

Among synthesis processes adapted to reach structural control in manganese oxides, aqueous chemistry provides a very rich synthesis platform, according to three possible redox approaches: (i) Mn(II) precursor oxidation by *e.g.* $K_2S_2O_8$,[46] O_2,[34] O_3[47] or H_2O_2, (ii) Mn(VII) precursor ($KMnO_4$) reduction by water[38] or sulfates,[48] and (iii) Mn comproportionation by reacting a Mn(II) and a Mn(VII) source.[37,49–51] In these experimental approaches, structural control is rationalized *versus* thermodynamic (high temperature and long reaction time) or kinetic control (low temperature and short reaction time).[52]

Potential–pH diagrams are invaluable tools to explain the outcome of aqueous syntheses under thermodynamic control. However, a variety of parameters can impact aqueous precipitation: precursor nature and composition, surfactant concentration, pH, presence of additional ions (K^+, NH_4^+, H^+, and F^-), reaction time and temperature.[33] In particular, intercalated alkali ions modify the relative stabilities of the polymorphs, as shown by phase diagrams calculated by Chen *et al.* at 160 °C for K^+ (Fig. 6A).[53,54] In particular, the equilibrium phase evolves from β-MnO_2 to α-MnO_2 upon an increase of the potassium concentration. Another important parameter not considered in traditional Pourbaix diagrams is the size dependency of the stability of solids. Indeed, creating surface has an energetic cost. Hence, the lower the surface energy, the lower the destabilization due to a decrease in the particle size. For sufficiently small particle sizes, a thermodynamic crossover can be observed in polymorph stability, usually around 10–20 nm, where the bulk metastable phase becomes the nanoscale thermodynamic product. This has been well described for TiO_2, Fe_2O_3, and Ti_2O_3 polymorphs for instance.[55–58] The computed size-dependent phase diagram as a function of the potassium chemical potential (Fig. 6B) reveals a complex entanglement of the composition-dependent stability and several thermodynamic crossovers as a function of the particle size.

Therefore, while the usual potential–pH Pourbaix diagrams are useful for a rough estimation of the expected outcome of aqueous syntheses, one must develop extended Pourbaix diagrams to account for the composition of the liquid medium (*e.g.* presence of additives), for the size-dependency of the stability of solids, and for the metastable phases. Recently, Chen *et al.*[45] took a step forward in the construction of such diagrams in the case of

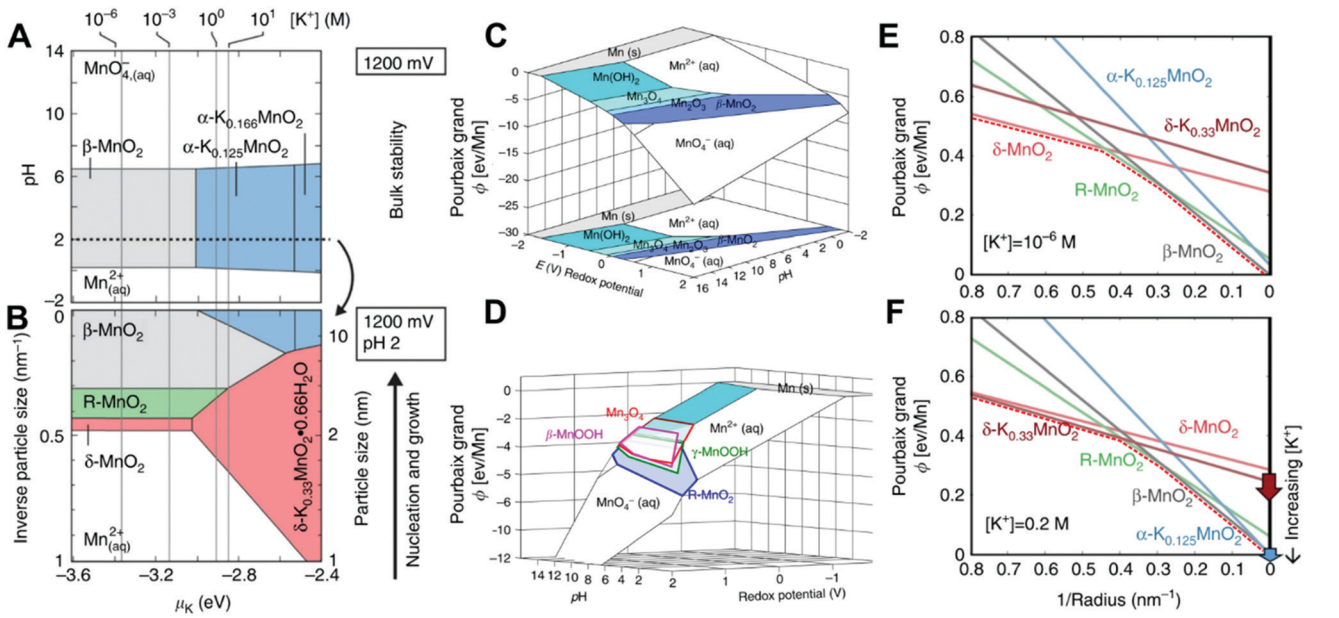

Fig. 6 Extended speciation diagrams and Pourbaix diagrams of manganese oxides: (A) K^+ chemical potential–pH diagram for bulk manganese oxides and (B) chemical potential–particle size influenced oxides. Pourbaix diagram using the Pourbaix grand potential and showing (C) the stable phases at [Mn] = 10^{-2} M and 25 °C, (D) the Pourbaix free energy surfaces of metastable β-MnOOH, γ-MnOOH, and R-MnO_2, and the full aqueous stability region of Mn_3O_4. Pourbaix grand potential–particle size projection of the size-dependent Pourbaix diagrams at (E) [K^+] = 10^{-6} M and (F) [K^+] = 0.2 M. In (E) and (F), the crystallization pathway from left to right occurs through the path of minimized Pourbaix grand potential (red dashed lines, see Fig. 7). A, B, E, and F are adapted with permission of Springer Nature from ref. 45. C and D are adapted with permission of Springer Nature from ref. 59.

manganese oxides. The authors used tabulated thermochemical data concerning the known bulk phases and used density functional theory calculations to evaluate the energetics of bulk phases missing in the databases as well as surface energies (Fig. 6B–D).[45,59] In order to account for metastable phases and size-dependency, the authors proposed to add a free energy axis to Pourbaix diagrams in the form of a grand potential named the Pourbaix grand potential (Fig. 6C and D).[45,59] This representation enables stable as well as metastable phases to be highlighted.

Free energy Pourbaix diagrams can also be used to gain insights into the reaction mechanisms of aqueous syntheses. The Ostwald–Lussac rule of stages[60,61] generally applies to manganese oxides crystallizing in water, which means that the reaction medium evolves through a series of consecutive crystallization events by increasing order of stability, from the "most unstable" metastable solid state (M in Fig. 7) to the thermodynamic product (S in Fig. 7).[45] This evolution accounts for the smaller surface energy of low stability metastable phases than that of more stable ones. The energetic cost for the formation of the solid from the supersaturated solution is then lower for metastable phases, hence driving nucleation of the low stability solids first. Free energy Pourbaix diagrams provide a direct visualization of crystallization pathways according to the Ostwald rule (Fig. 6E and F), by following the path of the minimized Pourbaix grand potential upon particle size increase. For instance, at low $[K^+]$, δ-MnO_2 nucleates first during the reaction, followed by an intergrowth of metastable γ-MnO_2 and β-MnO_2. Then, β domains grow at the expense of the γ phase, until the formation of the thermodynamic product β-MnO_2 as a single phase (Fig. 6C). In contrast, at high potassium concentration (Fig. 6F), K^+ has a structure-directing agent effect due to its intercalation into tunnel frameworks, changing the equilibrium phase from the β-MnO_2 phase to α-MnO_2, and then δ-MnO_2 upon an increase of the potassium concentration. A similar effect has been reported under hydrothermal conditions at 180 °C,[62] where the high temperature triggers a dissolution–recrystallization mechanism of poorly stable amorphous MnO_2 into α-MnO_2 or β-MnO_2, at high K^+ or high H^+ concentrations, respectively. These theoretical considerations have been experimentally confirmed by *in situ* wide-angle X-ray scattering[45] and previously observed *ex situ*.[52] Besides describing crystallization pathways, they provide a frame to rationalize changes in induction time and nucleation kinetics depending on acid–base conditions,[63] and on the relative stabilities of different polymorphs.[64]

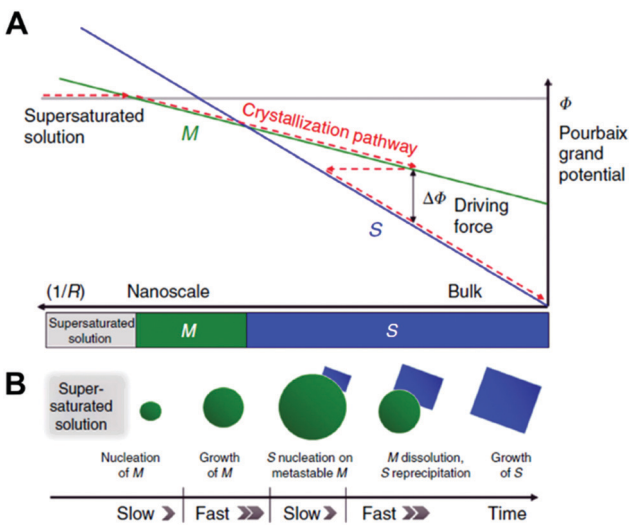

Fig. 7 Relationship between metastability and the crystallization sequence: (A) free-energy of three phases as a function of the surface-area-to-volume-ratio, 1/*R* where *R* is the radius. Gray, green and blue lines correspond to the free-energy of a supersaturated solution, a bulk metastable (M) and a bulk equilibrium phase (S), respectively. (B) The multi-stage crystallization pathway. Adapted with permission of Springer Nature from ref. 45.

3.3. Predicting structural evolutions through extended Pourbaix diagrams: ion exchange and mineral displacement

Foreign cations can be used for phase selective synthesis not only by changing the crystallization sequence as described above. Indeed, ion exchange is another important mechanism in geological processes, which again finds applications in materials synthesis. This is well demonstrated by the simple case of manganese oxides, which shows how ionic strength, an important parameter in natural crystallogenesis, can be used to control phase selectivity. For instance, ion exchange in layered δ-MnO_2 combined with hydrothermal treatment can yield a wider variety of crystal structures (Fig. 8A).[34,65,66] Interlayer sodium cations in δ-Na_xMnO_2 are first exchanged by different cations. Then, hydrothermal conditions drive the conversion to other framework structures. Here, ion exchange is combined with structural transformations that find a direct parallel with mineral replacement reactions found in geology.[67–69] Further treatment of Mg-todorokite under acidic conditions enables exchanging Mg^{2+} cations with Li, Na, K and Cs insertion, thus leading to Li-todorokite, Na-todorokite, K-todorokite and Cs-todorokite. Another example has been provided by Andris *et al.*,[70] who showed that hydrothermal treatment of δ-MnO_2 intercalated with sodium cations can lead to (2×3) and (2×4) tunnel MnO_2 structures depending on the Na^+ concentration in the hydrothermal medium (Fig. 8B). Extended Pourbaix diagrams (Fig. 6A and B for K^+) can nicely account for the rationale of these phase transformations driven by ion exchange.

A similar approach has been used recently to design new iron and titanium doped α-MnO_2 nanowires. δ-MnO_2 exhibits high tolerance to transition metal cationic doping, contrary to α-MnO_2 with its rigid 1D tunnel structure. Therefore, by doping the initial layered phase by direct synthesis and then triggering its transformation with hydrothermal treatment, we could obtain framework Fe, Ti-doped α-MnO_2[71] (Fig. 8C). Fe-doped α-MnO_2 exhibits high catalytic activity for CO oxidation.[72] In a similar approach, δ-MnO_2 could be ion exchanged directly with Cr, Fe and Co cations intercalated in the interlayer space, followed by transformation into δ-MnO_2.[46,73] The resulting α-MnO_2 nanowires showed higher performance in the catalysis of toluene degradation compared to α-MnO_2 obtained by direct hydrothermal synthesis.[74] Therefore, ion exchange and mineral

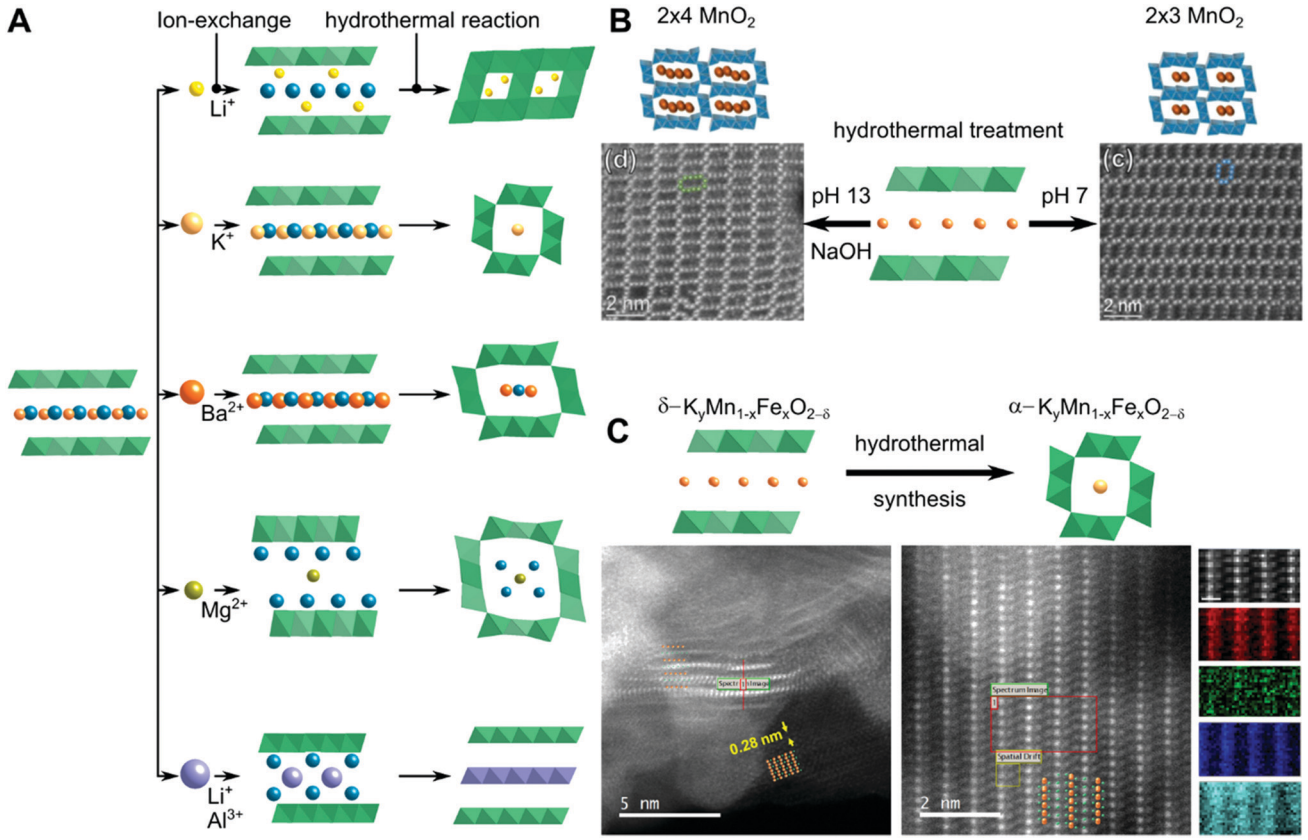

Fig. 8 (A) Ion exchange-driven transformations from Na-birnessite to tunnel and layered manganese oxides under hydrothermal conditions. Figure adapted from ref. 34 with permission of the Royal Society of Chemistry. (B) Use of cationic exchange in aqueous precipitation for the preparation of (2 × 3) and (2 × 4) MnO_2 and the corresponding scanning transmission electron microscopy (STEM)-high angle annular dark field (HAADF) images showing the columns of MnO_6 octahedra. Figure adapted with permission of Elsevier from ref. 70. (C) Fe-doped α-MnO_2 obtained by doping layered δ-MnO_2 with Fe and Ti followed by hydrothermal conversion into the (2 × 2) tunnel framework of α-MnO_2. Figure adapted from ref. 72 and 75 with permission of the Royal Society of Chemistry and SciTech, respectively.

replacement reactions provide interesting pathways to design new solids and nanoscaled solid-state phases.

3.4. Predicting structural evolutions through extended Pourbaix and phase stability diagrams: from geosciences to functional materials

The case of manganese oxides strengthens the importance of considering an extensive set of features for the solid and its surrounding environment to rationalize and predict phase selective synthesis. Free energy Pourbaix diagrams also explicitly describe how redox properties depend on the particle size. This had been experimentally assessed previously by Navrotsky *et al.*[76] for a range of transition metal oxides. The authors pointed for instance at the shrinkage of stability domains for divalent transition metal species at diameters below 10 nm. The authors raised the important role that the size dependent redox properties of nanoparticles may have played in abiotic organic synthesis and may still play in biological processes. Extended Pourbaix diagrams are also of high interest for the development of materials. In particular, they may drive the search for corrosion-resistant nanomaterials of high relevance for electrocatalysis.[77]

Further developments are required to address more complex solids with this approach. In particular, Pourbaix diagrams are emerging for multicationic oxides of relevance for electrocatalysis in fuel cells.[78] Rondinelli, Poeppelmeier *et al.*[79] also recently reported a related approach by combining computed Pourbaix diagrams and constant potential phase stability diagrams showing the dependence of phase stability *versus* the concentration of elements and the pH. Combining these two sets of data, they predicted the conditions of the synthesis of multianionic compounds by taking the case study of BiMOQ (M = Cu, Ag; Q = S, Se). The authors focused on identifying the conditions to ensure that the target phases are the thermodynamic products. They also considered metastable species and assessed the driving force for the formation of each phase. By doing so, reaction yields could be predicted and superimposed to the stability diagrams. The areas of highest yield were those with the highest probability of successful synthesis, as further confirmed by experimental synthesis.

In this section, we have revealed some mechanistic relationships between aqueous synthesis of (nano)materials and geological processes, namely dissolution–recrystallization, ion exchange and mineral replacement. We have focused on one

major evolution of protocols in water towards predictive synthesis. These breakthroughs have been made possible thanks to the input of modern calculation approaches and the consideration of size effects on the energetics of solid formation. With these advances, the ability to control polymorphism, to predict the existence of unknown phases and their synthesizability, is expected to gain in accuracy in the near future.

In some cases, aqueous synthesis may show some limits for industrial applicability. Indeed, difficulties in scaling-up the production could arise from maintaining the homogeneity of batch reaction media. Furthermore, the protocols discussed above are related to long synthesis times from a few hours to days. As a consequence, other approaches have been developed to provide fast production and the ability to precisely tune the reaction temperature and time. Some of these methods are described below.

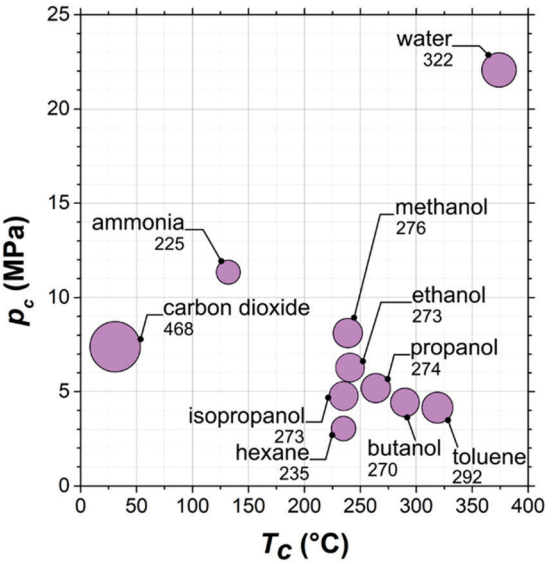

Fig. 9 Example of critical coordinates for common solvents (extracted from ref. 82): critical temperature (T_c) and critical pressure (p_c). The critical densities (ρ_c, kg m^{-3}) are written next to the liquid names. The relative surfaces of the bullets correspond to these values.

4. Supercritical hydro/solvothermal synthesis

The hydrothermal methodology may show some limits for industrial applicability, related to long synthesis times and difficulties of scaling-up the production by maintaining the homogeneity of batch reaction media. As a consequence, other approaches have been developed to provide fast, sustainable production and the ability to precisely tune reaction temperature and time. Supercritical hydrothermal flow synthesis (SHFS) is among these methods.

4.1. Supercritical conditions on the Earth

Synthesis in supercritical fluids is inspired by the high temperature and high-pressure environments that can be found in some of the deepest known hydrothermal vents, above 400 °C and ~280 bars. Despite the aqueous medium, these conditions provide a rich chemistry of non-oxide solids.[80] In particular, these regions encompass chalcopyrite ($CuFeS_2$), bornite (Cu_5FeS_4), pyrite and marcasite (FeS_2), as well as sphalerite (ZnS). Below, we discuss the main features of the SHFS in relation with the design of synthetic functional minerals.[81]

4.2. Supercritical hydrothermal flow synthesis

Supercritical fluids were discovered in 1822 by the French engineer and physicist Charles Cagniard de La Tour. For synthetic chemists, a supercritical fluid is a solvent that is used above its critical pressure and temperature (Fig. 9). Supercritical fluids exhibit intermediate properties between liquid and gas (Fig. 10A), which can be adjusted continuously from liquid-like to gas-like behaviors by just changing the pressure and temperature. At the molecular level (Fig. 10A), a supercritical fluid is composed of two kinds of domains, with gas-like and liquid-like densities, respectively. The correlation length of the reaction medium changes with pressure and temperature. As a consequence, in a supercritical solvent, chemistry can be performed as in a liquid, but in a gas-like environment. This obviously deeply impacts the precipitation and crystallization of inorganic materials.

Among the solvents listed in Fig. 9, water stands out for its specific properties. Most often, the increase of temperature at constant pressure induces a decrease of the density (Fig. 10B). For water, the direct consequence is a decrease of the dielectric constant (Fig. 10C), which enables tuning the solvation properties, as supercritical water behaves like hexane, an apolar solvent. In other words, oil is soluble in supercritical water but not salts.[85,86] Another interesting behaviour concerns the evolution of the ionic product of water (Fig. 10B), which is about three orders of magnitude higher at 250 °C than at room temperature under 250 bars. Therefore, sole water can replace acid or basic solutions under hydrothermal conditions, as in the surface treatment of ceramic fibers.[87] Around the critical temperature of water, the ionic product is falling and radical mechanisms are then favoured in supercritical hydrothermal reaction media.[88]

These properties have been exploited in many fields of applications, especially in SHFS. SHFS was first reported by Adschiri *et al.* in the beginning of the 1990s[89] and has been mainly applied to oxides.[90] Other solvents (Fig. 9) can be used to synthesize other families of materials.[82,91] The basic principle of SHFS is shown in Fig. 10D. Supercritical water is combined with a precursor solution (generally metal salts) at the mixing point, which is a key part of the process.[92] Then, the medium is carried to the supercritical reactor where hydrolysis, dehydration and inorganic polymerisation occur to produce the oxides. The reaction is very fast, a few tens of seconds. A variety of alternative processes exists, for instance, the use of a single line[93,94] or one-pot multistep processes for the design of multicomponent materials.[95] The main operating parameters are the pressure, the temperature, the residence time and the nature and concentration of metal precursors. The scientific

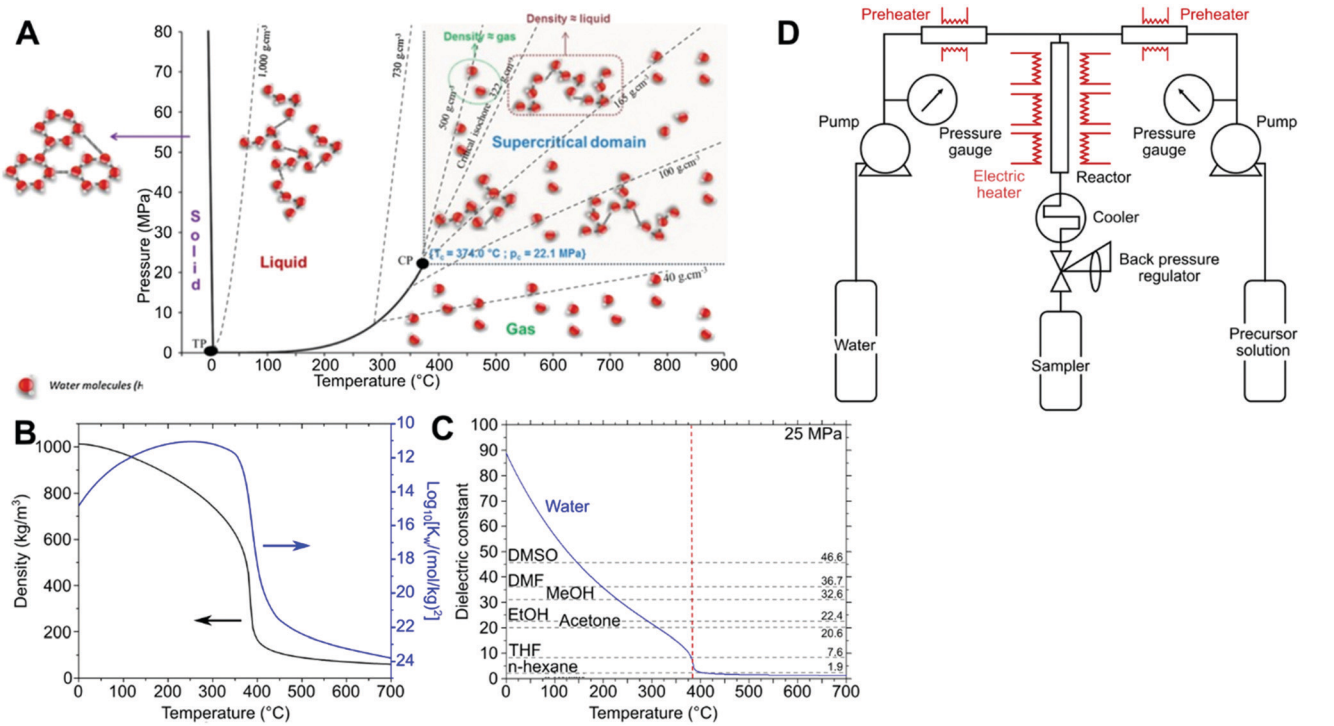

Fig. 10 (A) Pressure–temperature phase diagram of water. Adapted from ref. 83 with permission of Wiley-VCH Verlag GmbH & Co. KGaA. (B) Evolution of density and ionic product of water as a function of temperature at 25 MPa. The data were collected from the National Institute for Standards and Technology (NIST) database.[84] (C) Evolution of the dielectric constant of water as a function of temperature at 25 MPa. Comparison with common solvent values at room temperature and pressure. The red vertical line shows the critical temperature of water. Adapted with permission of Elsevier from ref. 85. (D) Schematic diagram of a SHFS reactor developed for flow synthesis of nanoparticles.

community involved in this field has investigated in the last 30 years the effect of these parameters on the characteristics of the synthesized materials in terms of structure, morphology, size distribution, and surface properties. The development of *in situ* investigations has further enabled modelling of nucleation and growth in supercritical water.[96–98] Herein we highlight recent studies on a new field of SHFS application: the synthesis of distinct nanoscaled minerals, namely phyllosilicates and inosilicates.

4.3. Supercritical hydrothermal flow synthesis of talc and other phyllosilicates

Talc is a clay mineral composed of hydroxylated magnesium silicate with the chemical formula $Si_4Mg_3O_{10}(OH)_2$.[99] It has a significant commercial importance, being used in numerous products such as paper, plastics, paints, ceramics, and construction materials and in automotive and cosmetic industries.[81] In nature, it forms from the metamorphism of magnesium-rich rocks.[100] As an example, the talc deposit located at Trimouns, in the French Pyrenees, has been formed as a consequence of 14 million years of continuous circulation of hydrothermal fluid.[101] The conditions for the formation for this deposit correspond to pressures and temperatures between 200 and 300 MPa and 300 and 350 °C,[102] respectively, hence close to the supercritical domain (Fig. 10A). Even though the composition of this mineral generally stays close to the nominal formula, substitutions can occur, *e.g.* Si substitution by Al, or Mg substitution by Fe, Mn, and Al.

Naturally occurring talc shows some limitations for industrial use, such as (i) contaminations from other minerals (carbonates, chlorite, asbestos, *etc.*); (ii) hydrophobicity, which hinders dispersion in aqueous media; and (iii) large particle size (around 2 and 100 μm after grinding), which restricts the development of polymer-based nanocomposites.[81,103] Producing synthetic talc can overcome all these limitations. The hydrothermal synthesis of talc in a batch reactor was first reported in 1989.[104] Since then, many research efforts have been made with the aim of optimising the process and reducing considerably the synthesis time from several days down to a few hours.[103,105,106] The first talc synthesis in only 10 s was reported in 2016 by Dumas *et al.*[107] who combined a continuous flow set-up with the use of supercritical water. Besides shortening the reaction times, the authors also obtained a new material, so-called nanotalc, with a high chemical purity, nanoscale particle size, and hydrophilic nature. This work demonstrated the promising role of SHFS in the rapid and versatile production of highly crystalline and pure geominerals at the nanoscale. Nanotalc was synthesized in a continuous reactor at 25 MPa by employing an aqueous solution of sodium metasilicate and a solution of magnesium acetate in acetic acid as precursors with a Si/Mg ratio equal to the Si/Mg talc ratio. A parametric XRD study showed that the talc structure was obtained only under supercritical conditions above 380 °C. The product obtained at

400 °C for 23 s showed crystallinity comparable with that of talc obtained by a conventional batch hydrothermal synthesis at 300 °C and 8.5 MPa for 2 hours.[105]

The high modularity of continuous reactors allows the scaling up of syntheses after process engineering. Hence, a pilot was further developed for producing kg scale of synthetic dried talc (*i.e.* 10 kg of gel) per day.[103,108]

The crystallization kinetics could be monitored by assessing the evolution over time of the crystal size coherency (CSC) in the direction of stacking of the structural layers (Fig. 11A).[81,109] The conventional batch hydrothermal synthesis (300 °C, 8.5 MPa) is characterized by a linear CSC increase with the reaction time. In contrast, the CSC profiles change drastically with the SHFS process (25 MPa during 20 s), as the CSC values are steady below the supercritical domain, but undergo a steep increase when accessing supercritical conditions. Similar trends are observed for the CSC accounting for the extent of the layers. These evolutions nicely account for large changes in the physicochemical properties of water under supercritical conditions, *i.e.* the drastic fall of the dielectric constant, of the density of water (Fig. 10B and C), which dramatically changes solvation, promoting the inorganic polymerization of the precursors and the growth of talc crystals.[81,110]

Synthetic talc exhibits a higher purity compared to natural specimens,[112] which is relevant especially in cosmetic and pharmacological uses.[103,113] The particle size of talc synthesized by SHFS is also decreased (Fig. 11C)[109] compared to micron scale natural grains (Fig. 11B). This ensures better dispersion in composites than natural specimens. Likewise, the thermomechanical properties surpass those of the natural counterparts, thus enabling a decrease in the loading rate when employed in paints and polymer composites.[114–116] The nanometric size and the SHFS process itself also change the wetting ability by providing hydrophilicity to the surface, thanks to a high density of particle edges (Mg–O and Si–O) and surface hydroxyl groups.[109] Such a hydrophilicity has allowed the development of the first talc filler without the use of a pre-surface coating or of compatibilizers in plastics.[115] Overall, the case of nanotalc shows that supercritical hydrothermal flow synthesis can deliver new materials with distinct surface properties, by modifying reaction mechanisms, especially nucleation and growth kinetics.

Beyond talc, the high versatility of the supercritical flow chemistry for producing phyllosilicate minerals with layered structures has been highlighted by Claverie *et al.*, in 2018,[111] who obtained a variety of solids (400 °C, 25 MPa, and 20 s) by only varying the amount of ethanol in the water/ethanol mixture used as the solvent (Fig. 11D). The proposed synthesis mechanism relies on the change in the silicon precursor solubility in the presence of ethanol, which in turn determines the formation of tetrahedral SiO_4 sheets.[111] Supercritical water was also used to obtain another clay mineral named montmorillonite (generic chemical formula: $(Na,Ca)_{0.3}(Al,Mg)_2Si_4O_{10}(OH)_2{\cdot}nH_2O$), a member of the smectite family.[117] In Nature, the minerals

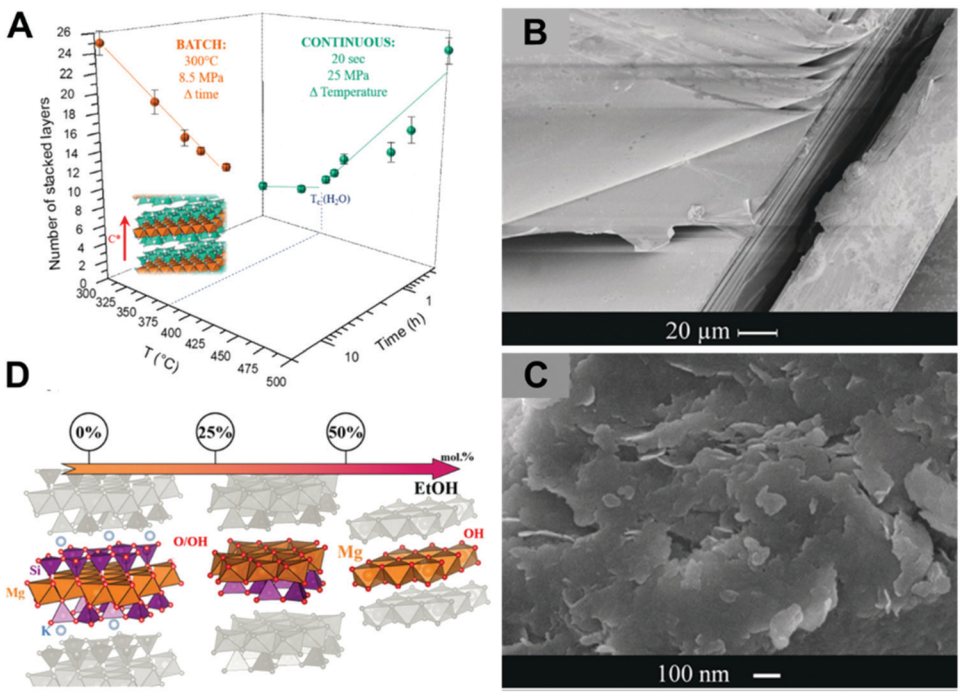

Fig. 11 Supercritical hydrothermal flow synthesis of nanotalc. (A) Evolution as a function of the synthesis time of the crystal size coherency in the direction of stacking of the structural layer direction. Data for SHFS and a conventional hydrothermal batch synthesis are reported. Reprinted from ref. 81 with permission of Wiley-VCH Verlag GmbH & Co. KGaA. Scanning electron microscopy images of (B) natural talc and (C) synthetic nanotalc synthesised by SHFS (400 °C and 25 MPa for 20 s). Reprinted from ref. 109 with permission of Wiley-VCH Verlag GmbH & Co. KGaA. (D) Crystal structures of the three distinct minerals obtained as a function of the ethanol content of a water/ethanol mixture used at 400 °C, 25 MPa for 20 s. Reprinted from ref. 111 with the permission of Cambridge University Press.

belonging to smectites commonly form as a consequence of the weathering of basic or acidic igneous rocks, or in sedimentary and metamorphic rocks.[118] As in the case of talc, synthetic montmorillonite particles obtained by a conventional hydrothermal synthesis are characterised by an average diameter of about 1 μm at least.[119] Again, subcritical conditions were not suited to form montmorillonite. By crossing the critical point of water, a foggy state with low amounts of suspended particles formed. Upon a further increase of the temperature, a milky and concentrated suspension of montmorillonite particles was obtained. The crystallization of layered montmorillonite was accompanied by faceting the particles towards the formation of the sheets expected for clays.

4.4. Supercritical hydrothermal flow synthesis of calcium silicate hydrates

Calcium silicate hydrates (CSH) form as a consequence of geological hydrothermal processes in which hyperalkaline fluids react with basic igneous rocks. They are also the products of chemical reactions during cement hydration. Indeed, the calcium silicate hydrate gel is the principal hydration product of cement paste and the primary responsible for its strength and performance. The interest in CSH minerals lies first in their complex structure still not fully elucidated, second in their potential for orthopedic applications,[120] insulating materials,[121] stabilising agents to trap impurities in wastewater and as additives for reinforced cement.[122] A significant effort has been made recently for the development of an innovative hydrothermal supercritical flow synthesis to expand the synthetic CSH mineral production towards industrial requirements.[123–125]

In 2017, Diez-Garcia *et al.* reported the first supercritical hydrothermal flow synthesis of two calcium silicate hydrate minerals, namely xonotlite and tobermorite.[123,124] Then, Musumeci *et al.* optimized the process to improve the purity, crystallinity, and quantity of the produced materials.[125,126]

Natural xonotlite is commonly found near the contact between igneous rocks and calcium bearing rocks.[127] Xonotlite is usually described using the ideal stoichiometric formula $Ca_6Si_6O_{17}(OH)_2$. Besides Ca, Si, O and H atoms, traces of Na^+, Fe^{3+}, K^+, and Mn^{2+} can occur in natural specimens. Xonotlite is one of the most stable phases of calcium silicate hydrates.[128] Its hydrothermal synthesis has been widely investigated between 150 and 250 °C,[120,129–131] especially from CaO and SiO_2 in crystalline or amorphous forms.[130,132,133] The reaction time ranges from a few hours to weeks, depending on the temperature.[134] Below 200 °C, other secondary phases are often observed. In 2018, the first supercritical hydrothermal flow synthesis of xonotlite enabled a leap forward in terms of reaction time and crystallinity.[124] Two precursor solutions were prepared by dissolving separately stoichiometric amounts of calcium nitrate tetrahydrate and sodium metasilicate nonahydrate in water. Supercritical conditions, 400 °C at 25 MPa, delivered high crystallinity xonotlite in only 7 s.[125,126] The lab-scale set-up yielded a continuous production of about 2.9 g h^{-1}.[126] Under these conditions (Fig. 12A and C), xonotlite crystallizes as flat fibres oriented along the direction of silicate chains,[125,126] approx. 10–30 μm long and 50–200 nm wide, like in conventional hydrothermal synthesis at 200 °C for 1 day.

The second calcium silicate hydrate mineral synthesised so far by a SHFS process is tobermorite. As xonotlite, tobermorite

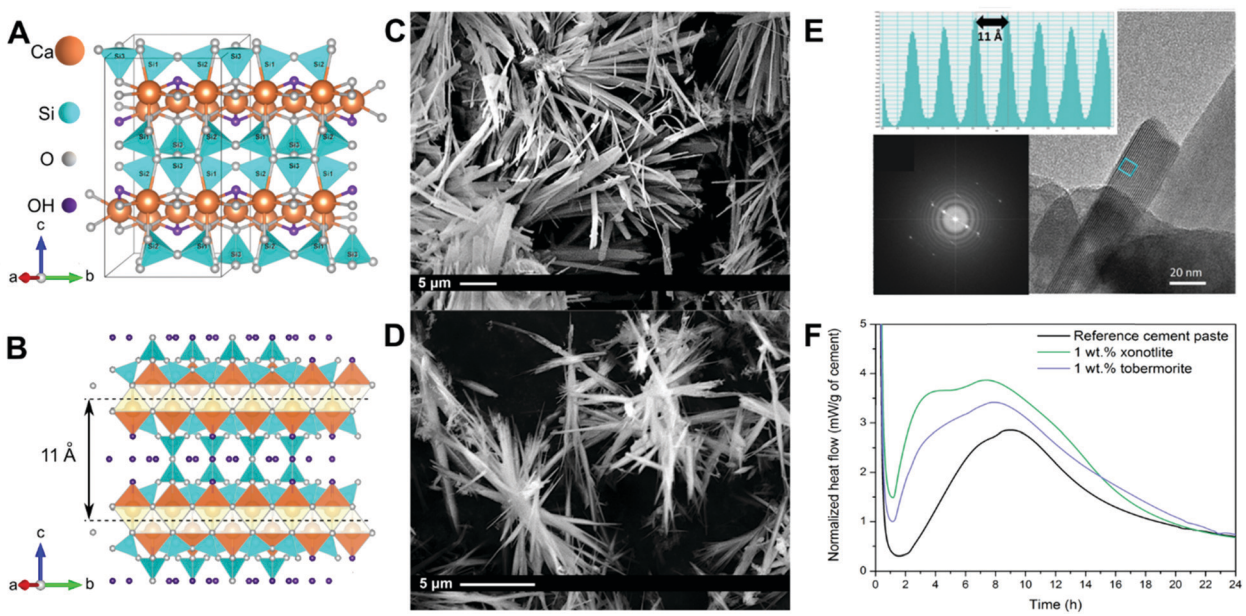

Fig. 12 Crystal structures of (A) xonotlite and (B) 11 Å tobermorite. Reprinted with permission from ref. 126. SEM images of (C) xonotlite and (D) tobermorite particles synthesised in supercritical water. Reprinted with permission from ref. 125 with permission of Wiley-VCH Verlag GmbH & Co. KGaA. (E) HRTEM image of a tobermorite nanofibre. Reprinted from ref. 123 with permission of Wiley-VCH Verlag GmbH & Co. KGaA. (F) Heat flows measured over time by calorimetry during the hydration of reference cement paste and seeded cement pastes prepared with the addition of 1 wt% of xonotlite and tobermorite. Reprinted with permission from ref. 126.

(Fig. 12B and D) is a rare and scarce mineral. It is mainly found in or near the cavities of basic rocks, or at the contact between dolerite and limestone.[135] Tobermorite has been detected in ancient Roman archaeological cementitious specimens, and is widely accepted as the origin of the durability of Roman structures.[136] Natural tobermorite commonly encompasses aluminium as a substitution of silicon. Al-substituted tobermorite is associated with pyroclastic puzzolans, and Si-poor and Al-rich species, used in Roman concrete binders. A better understanding of the tobermorite structure is crucial to better understand the CSH gel involved in cement. Depending on the degree of hydration, the basal distance between the Ca–O layers ranges from 9, to 11 and 14 Å,[137] hence yielding three structural varieties: 9 Å tobermorite, 11 Å tobermorite or 14 Å tobermorite. The variety with a closer resemblance to the cementitious CSH gel is the 14 Å tobermorite.[138] Instead, the most common and stable variety synthesized is the 11 Å one.

The metastability of tobermorite compared to xonotlite makes its synthesis challenging.[131,132,139–141] Flow chemistry enables a precise control of experimental conditions, especially the reaction time, which is difficult to achieve in batch reactors. As in Nature, the addition of aluminium during hydrothermal synthesis stabilizes tobermorite and facilitates its crystallization *versus* xonotlite.[141]

Diez-Garcia *et al.* reported the first synthesis of tobermorite under supercritical conditions (400 °C and 23.5 MPa),[123] by adding aluminium to the reaction medium. Only the use of ultrafast reactions, 7 s rather than 10 and 15 s, enabled decreasing the fraction of the xonotlite by-product.[123] Noteworthily, tobermorite was synthesized far above its stability limit (~140 °C).[139] This highlights the ability of supercritical flow chemistry to provide a fine control over reaction times and kinetics. As in Nature[142] and contrary to conventional hydrothermal synthesis,[140] SHFS delivers tobermorite nanofibres approx. 2–20 mm long and 10–20 nm wide (Fig. 12D and E).[123,125,126] XRD, TEM, solid-state nuclear magnetic resonance spectroscopy (SSNMR), Raman spectroscopy and High Pressure X-Ray Diffraction (HP-XRD) showed that the crystallinity was increased under supercritical conditions compared to conventional hydrothermal synthesis.[126] The overall morphological and structural features of the SHFS product were much more comparable to natural specimens than other synthetic samples less crystallized.[126,143] These characteristics result in enhanced mechanical properties.[126] The formation of natural tobermorite occurs at low temperature over many years, while synthetic varieties have to form in a much shorter time. As a result, the reaction temperature must be increased in the laboratory to trigger a faster crystallisation process, which increases the risk of crystallization of more stable mineral phases. Only the accurate control of the reaction time provided by flow chemistry enables achieving a precise trade-off between the growth of metastable phases and nucleation of more stable phases.

Thanks to their high purity and crystallinity, SHFS-derived xonotlite and tobermorite can be used to disclose some aspects of the calcium silicate hydrate structures still not fully understood. In particular, these model minerals improved our knowledge of the relationship between the dynamics of nano-confined water and surface chemistry in these materials.[125] Musumeci *et al.* investigated this relationship by using tobermorite as a model of the effect of the Si–OH environment on water dynamics, and xonotlite as a mineral archetype to examine the additional contribution of the Ca–OH chemical environment. The hydrogen bond network of the minerals was investigated through a combination of ^{1}H SSNMR, Raman spectroscopy and Fourier-transform infrared (FTIR) spectroscopy, and then exhaustive broadband dielectric spectroscopy measurements were carried out.[125] The authors reported three different dielectric relaxation processes in SHFS-derived xonotlite and tobermorite. The fastest process was related to the dynamics of dangling hydroxyl groups, either Ca–OH or Si–OH. A second slower relaxation process was linked to the organization of water molecules at the surface of the materials, from an ''ice-like'' ordering in the Si–OH-rich environment of tobermorite to a disordered ''liquid-like'' distribution in the Ca–OH-enriched environment of xonotlite. The third and slowest relaxation process was assigned to the simultaneous presence of bulky non-evaporable water and ions freely moving along the structures. This work enabled refining the picture of the dynamics of confined water and hydroxyl groups in calcium silicate hydrates and other water-containing materials. Because SHFS-derived tobermorite is similar to natural tobermorite, the synthetic analogs can be used to mimic the dielectric behaviour of natural specimens,[125,144] with especially a fast process at high frequency.

Among a wide range of applications, xonotlite and tobermorite can be employed as seeds for accelerating the hydration process of cement, and developing a denser and more resistant cement matrix.[126,145,146] Accelerator additives also play a relevant role in pre-cast structures where speeding up the hydration kinetics allows the removal of the mould, and the completion of the structure in shorter times, thus minimising the cost of construction. Additionally, accelerators are particularly suitable in cold environments to avoid the risk of frost damage in the cement network. The seeding effect of xonotlite and tobermorite to accelerate the early stage hydration of cement can be investigated by calorimetry (Fig. 12F). In the early stage of hydration, the nanoparticles dispersed in the cement paste act as nucleation sites, for the subsequent rapid formation of the C–S–H gel. Because of their high specific surface areas, xonotlite and tobermorite seeds accelerate the hydration process, leading to the increase of the hydration rate and heat release. In particular, the performance of xonotlite seeds is stronger than that of tobermorite nanoparticles. The different behaviours of the two nanominerals might be explained by their different Ca/Si ratios. In fact, it has been reported that the CSH nucleation rate increases with the Ca content from Ca/Si = 0.4 to 2.0.[147] Nonetheless, the existence of impurities such as portlandite and/or silica gel could also influence early hydration and result in a distorted evaluation of the actual quantity of CSH additions. Consequently, the influence of the Ca/Si ratio of seeds on cement hydration is still not fully elucidated.

4.5. Life cycle assessment of supercritical fluid-based synthesis

In the last few years, the relevance of supercritical fluid technologies has been recognised by the United States Environmental Protection Agency (US EPA) for the development of environmentally sustainable chemical processes.[148] The wide range of applications ranges from materials, semiconductors, energy, and synthetic chemistry science to waste treatment, pharmaceuticals and medical science. However, only very few contributions to understand the environmental profile of the SHFS process applied to nanoparticle synthesis have been discussed in the literature.[149–152]

To support the relevance of SHFS, the sustainability and environmental impact of this process must be addressed, thus raising a question: which method can be used to estimate how green a process is? One of the most appropriate tools for a comprehensive evaluation of the pros and cons of a manufacturing route is provided by life cycle assessment analysis (LCA), developed in the early 1960s in response to a growing concern about the limitations of energy sources and raw materials. LCA is standardised in the guidelines ISO 14040-14044 and defined as ''the compilation and evaluation of the inputs and outputs and the potential impacts of a product system through its life cycle''.[153] Therefore, LCA estimates the overall environmental impacts across precursors, solvents, and energy associated with materials processing, highlighting which contribution could be adjusted to improve the environmental profile. This analysis considers the entire life cycle of a product, from the extraction of raw materials to the end-of-life and waste disposal/recycling, through the manufacturing process and the use-phase. For each step of the product life cycle, the inputs (materials, energy, *etc.*) and the related outputs (emissions, by-products, water, *etc.*) are estimated.

Tsang *et al.* reported the first attempt to assess the environmental impact of supercritical solvothermal flow synthesis through an LCA study.[150] The authors focused on the production of $Ba_{0.6}Sr_{0.4}TiO_3$ nanoparticles in a continuous reactor maintained at 400 °C and 23 MPa, by using an ethanol–water mixture as the solvent, and barium, strontium, and titanium isopropoxides as precursors. They have shown that at the lab-scale (precursor concentration of 0.017 mol L^{-1}), the precursors account for only a minor fraction (3%) of the total impacts, while the average contribution from manufacturing, processing and ethanol disposal accounted for about 90% of the total life cycle impacts. The authors then showed that by increasing the precursor concentrations up to 0.1 and 1.0 mol L^{-1}, the average life cycle impacts decreased by nearly 81% and 95%, respectively. Additional recovery and reuse of solvents, with an efficiency of 90%, could further reduce the average life-cycle impacts by 56%. The authors also showed that by replacing ethanol with methanol, the impact could be further decreased. Note however that the large contribution of the solvents to the overall impact referred to an unoptimized lab-scale scenario. This contribution can be considerably reduced in an appropriate industrial scale facility, where a system of recovery and recycling of alcohol solvents can be implemented.

In a later work, life cycle assessment was employed to analyze the environmental profile of TiO_2 nanoparticle production *via* supercritical solvothermal flow synthesis using a water–ethanol mixture as the solvent.[152] The analysis was focused on comparing two production processes of TiO_2 nanoparticles: the supercritical fluid synthesis and the conventional precipitation method. The climate change potential and cumulative energy demand were reduced by 55% and 30%, respectively, by replacing the precipitation method by the supercritical flow process. The LCA impact was also significantly lower than that of the continuous solvothermal production of TiO_2,[151] under similar synthesis conditions, which can be explained by the use of ethanol rather than isopropanol and of higher precursor concentration in the supercritical flow process than in the conventional solvothermal synthesis, respectively. Operating at lower concentrations requires higher energy and solvent amounts for the same quantity of the product, thus resulting in an adverse effect on the environmental profile.

Recently, the cradle-to-gate environmental LCA analysis related to the SHFS of talc was evaluated by Glogic *et al.*[154] At the maximal reagents' concentration yielding 76 g L^{-1} of talc, the precursors account for 94% of the impacts. In particular, sodium metasilicate, employed as the silicon source, contributes solely to 40–60% of the total impacts, depending on the synthesis reaction. Importantly, replacing magnesium acetate by magnesium sulfate decreased the overall life cycle impacts by about 40%. In particular, the carbon dioxide impact and the cumulative energy required per kg of the produced talc could be decreased from 4.8 down to 2.6 kg and from 86 down to 34 MJ, respectively, just by changing a counter anion for more sustainable chemical precursors.

In this overview, the advantages of using supercritical water to produce a synthetic talc phyllomineral and two synthetic inominerals, xonotlite and tobermorite, in only a few seconds were highlighted. Through these case studies, we have highlighted how supercritical hydrothermal flow synthesis can be a direct approach to adjust and control the chemical composition of the synthetic nanominerals. This methodology could be used to investigate the production of other mineral families, such as sulfides, halides, carbonates, *etc*. Furthermore, despite the reduction of reaction times, SHFS allows producing model nanominerals, with high crystallinity. Hence, SHFS can disclose some uncovered aspects of mineral structures of interest for geology and environmental sciences. By providing access to minerals with modified structural and morphological features, SHFS can yield advanced functional materials, as shown for calcium silicate hydrates as additives for new cements and for lowering the environmental footprint of clinker production.

5. Quenching from high temperatures: focus on nanomaterials synthesis

5.1. Role of the cooling rate in naturally occurring crystallization: the case of volcanism

The impact of temporal temperature profiles on the solid nucleation from a melt is well exemplified by the crystallization

of igneous rocks from the cooling of lavas: the faster the cooling rate, the smaller the crystal sizes. Recently, the presence of 20–50 nm iron oxide nanoparticles in volcanic melts has been evidenced,[155] with a huge impact on the increase of magma viscosity. While nanoparticles (volume fraction below 5%) increase the propensity of the melt to maintain gas bubbles by strongly increasing its viscosity, they can also act as nucleation sites for gas bubbles. Both effects contribute to a large increase in the concentration of gas bubbles and to a lock up of the magma in the volcanic conduit, thus changing the dynamism of volcanic eruptions from effusive (*e.g.* Hawaii) to explosive behaviours (*e.g.* Mt. Etna and Tambora). Of relevance for the field of materials chemistry, iron oxide nanoparticles seem to form in the low viscosity magmas investigated, only at sufficiently high cooling rates, in the 10–20 °C s^{-1} range, when the melt is quenched from ~1300 °C to room temperature. Interestingly, such a rapid cooling also yields undercooling at 40 to 250 °C for the first 2 to 30 s spent below the liquidus. These conditions correspond to a fast magma ascent, from 5 to 50 m s^{-1}, as expected at Mt. Etna for instance. The high cooling rates and undercooling contribute to a large increase in the supersaturation and then to extensive nucleation and the formation of small objects.

5.2. Role of steep temperature profiles in nanoparticle synthesis

In colloidal synthesis, the hot injection method[156] and some quenching protocols[157] are well established to achieve size control by precisely tuning nucleation and growth processes. This is also well accepted in the metallurgy field, as a way to tune grain size and phase separation length scales, from the kinetically driven production of martensitic steels to metallic glasses. These examples are directly related to the observation made in the previous sub-section that steep temporal temperature profiles applied to liquid phase reactions favor nucleation over a short duration, hence smaller objects and more monodisperse samples.

5.3. Role of steep temperature profiles in structural control in nanomaterials

Beyond the well-recognized quenching approach used in colloidal synthesis to control size distribution by avoiding Ostwald ripening and maintaining the size focusing regime,[158] the recent emergence of nanoscaled high entropy alloys highlights the role that quenching methods can play not only in particle size control, but also in the design of complex solid-state compositions. In particular, the so-called carbothermal shock synthesis (Fig. 13) relies on extremely high heating and cooling rates by using short electrical pulses.[159] Application of this method to multimetallic nanomaterials has delivered a range of quinary, senary and septenary nanoparticles, stabilized as single fcc phases by high configurational entropy. To achieve homogeneous mixing, Yao *et al.* have used carbon nanofibers as a support and increased the temperature up to about 1700 °C with 55 ms electrical pulses and 10^5 °C s^{-1} heating/cooling rates. In particular, high cooling rates were instrumental in reaching single phases, as slower cooling resulted in phase separated nanoparticles. The technique delivered, among others, PtPdRhRuCe nanoparticles as catalysts for ammonia oxidation[159] and CoMoFeNiCu nanoparticles for ammonia decomposition catalysis.[160] Therefore, beyond control of particle and crystal domain sizes, quenching techniques provide approaches to control crystallization of new complex nanoscaled solids and materials.

6. Molten salts: focus on nanomaterials synthesis

6.1. Molten salts in nature: the case of evaporites

As mentioned in the introduction part, molten salts are involved in some geological processes. Evaporites are sedimentary rocks that crystallize from hypersaline solutions known as brines, which formed from the evaporation of saline waters in marine or non-marine environments (Fig. 14).[161] They are found mostly in hot arid deserts.[162] More than a hundred evaporite minerals are known, the most abundant ones being halides (NaCl, KCl, and $KMgCl_3{\cdot}6H_2O$), carbonates (calcium carbonates, $MgCO_3$, and $CaMg(CO_3)_2$ (dolomite)) and sulfates ($CaSO_4{\cdot}2H_2O$ (gypsum) and $CaSO_4$ (anhydrite)). Evaporites are mixtures of these salts and can undergo metamorphism, until melting when they are brought deeper in the Earth due to tectonics. Molten evaporites are then molten salts. A number of gems like rubies, emeralds and sapphire are found in metamorphized evaporites, which have undergone melting and then recrystallization upon cooling down closer to the Earth's surface. The presence of these gems in evaporites hints at their formation mechanism.[7,8] In particular, pigeon-blood rubies (Cr-doped corundum single crystals) have been proposed to form from molten evaporites at ~650 °C and ~3 kbar, where the molten salts can leach aluminium and chromium species from the surrounding marbles. For chemists, this process can then be described as a flux synthesis in a mixture of alkaline and alkaline-earth chloride and sulfate salts.

6.2. Flux growth and molten salt synthesis: from bulk crystals to nanomaterials

Inorganic molten salts have been recognized as reaction media for decades as they constitute some fluxes in the so-called flux synthesis methods, or flux growth methods.[91,92] Flux synthesis has been originally developed to grow large single crystals of a variety of solids, including oxides and intermetallics. The flux is a medium in which reagents have a significant solubility so that mass transport between reagents is enhanced, thus favoring the growth of large crystals. Solid formation proceeds either by increasing the temperature to trigger the reaction between reagents, or by cooling down the melt incorporating solubilized reagents. In the latter case, decreasing the temperature results in a decrease of the product solubility. This in turn increases the oversaturation of the melt and triggers crystal formation from homogeneous nucleation or from growth on seeds previously incorporated in the melt. Usual fluxes are molten

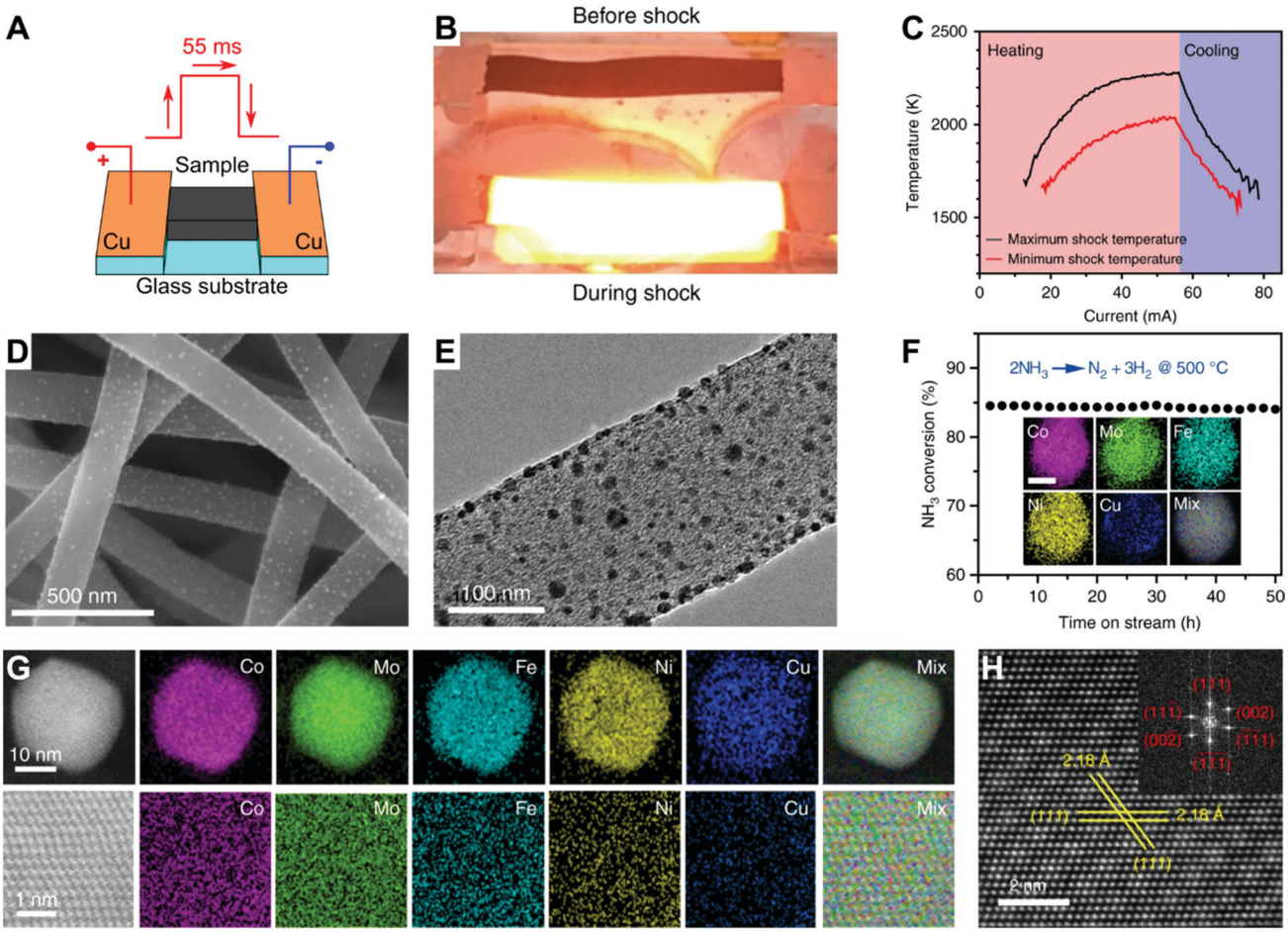

Fig. 13 Thermal shock carbothermal synthesis of high entropy alloy nanoparticles. (A) Device enabling thermal shock by electrical pulses of carbon nanofibers loaded with metal salts. Reproduced from ref. 159 with permission from The American Association for the Advancement of Science. (B) Optical photograph of the sample before and after shock, and (C) the corresponding temperature profile with heating and cooling rates of 10^5 K s^{-1}. (D) SEM and (E) TEM images of a CoMoFeCoNi alloy. (F) Ammonia decomposition catalysis on the CoMoFeCoNi alloy. (B–H) reproduced from ref. 160 with permission from Springer Nature.

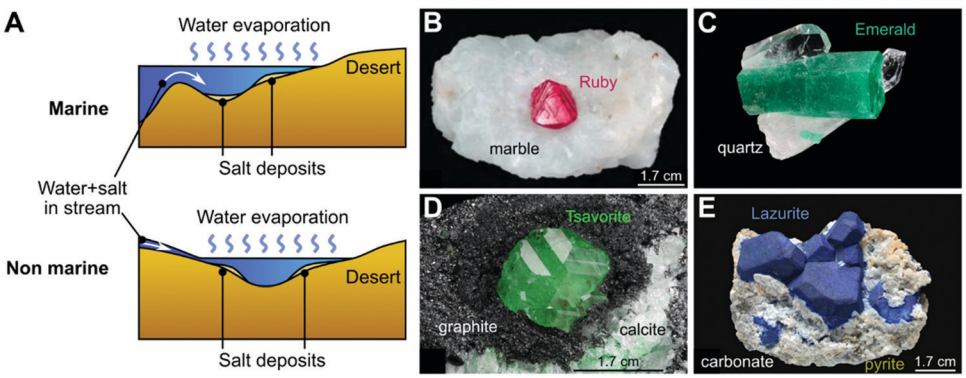

Fig. 14 (A) Marine and non-marine origins of evaporites, which can form molten salts in Nature. Metamorphic gems: (B) ruby, (C) emerald, (D) tsavorite and (E) lazurite associated with different minerals and for which the metamorphic pathways through molten salts (evaporites) have been proposed. (B) Adapted from ref. 163 with permission, (C–E) adapted from ref. 8 with permission from Springer.

metals, oxides, hydroxides, salts and their mixtures. Fluxes can also be reactive, participate in reactions and then provide elements constitutive of the final product. Because of enhanced mass transport, flux syntheses enable an increase in reaction rates compared to solid-state processes, so that reactions can be performed at lower temperature. Besides, because reaction

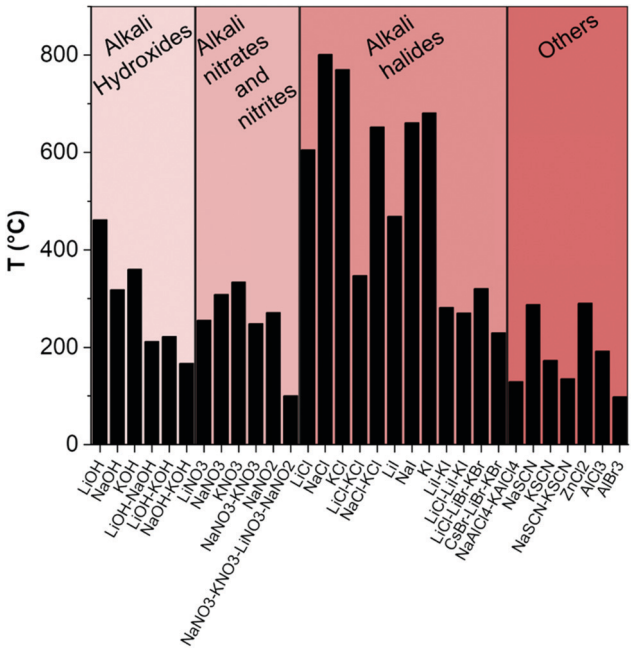

Fig. 15 Melting points of selected inorganic salts and their mixtures. The composition of most eutectic mixtures in this diagram can be found in ref. 166.

pathways strongly depend on the flux composition, the method is particular suited to reach new compounds not accessible by solid-state reactions.[164]

As in this geological case, flux synthesis in molten salts yields large crystals in the millimeter to centimeter range and then traditionally relies mostly on the thermodynamic control of solid formation, by using descriptors such as phase diagrams and solubility data to set the composition of the reaction medium for achieving the targeted product.[165] Flux syntheses in molten salts occur above the melting point of the salt or salt mixtures (Fig. 15).

Because flux growth methods towards large crystals are well described,[164] we focus herein on the synthesis of nanomaterials. For isolating nanostructured materials that are intrinsically metastable because of their high surface-to-volume ratio, the flux synthesis procedures have to move from thermodynamic control to kinetic control of reactions and of solid formation. This implies syntheses at lower temperature, shorter time, steeper heating and cooling temperature profiles, and often lower concentration of reagents in the melt. A number of reviews have been published over the last few years on the topic of molten salt synthesis of nanomaterials,[5,6,167] so that we prefer focusing herein on very specific aspects: the governing principles of molten salt synthesis of nanomaterials, how we can adapt experimental parameters to reach targeted nanomaterials, and recent advances in the field.

While flux growth methods can involve either reactions triggered by temperature increase or solidification upon cooling, to our knowledge, molten salt synthesis of nanomaterials relies exclusively on reactions occurring upon heating. This feature can be traced back to the habit of colloidal synthesis and aqueous precipitation communities to perform nano-object synthesis with reactions triggered by temperature increase, either by heating-up or by hot injection methods. This approach often ensures the narrowest size distributions for nano-objects of solids with a high melting point, including oxides, intermetallics and non-oxide ceramic materials, like *e.g.* nitrides, carbides, and borides.

6.3. Governing principles of molten salt synthesis of nanomaterials

Molten salt syntheses of nanomaterials usually proceed (Fig. 16) by intimately mixing powders of the salt(s) that will become the reaction medium above the melting point, and of the reagents, which can be salts (*e.g.* $NiCl_2$ and sodium borohydride), elements (*e.g.* carbon), or compounds (*e.g.* silica, sodium silicide, sodium borohydride, and polymers). Some examples will be detailed below. The mixed powders are then heated in conventional ovens (Fig. 16) above the melting point of the reaction medium to trigger the reaction between the precursors. After temperature dwelling, the reaction medium is cooled down; the salt solidifies, thus embedding the nano-objects. It must then be washed out, which can be performed by solubilization in water if the product is not sensitive to water exposure. If needed, few organic solvents, such as methanol, can help to bypass water sensitivity of the products, although the solubility of usual salts such as alkali halides in these solvents is orders of magnitude below the one in water, thus requiring large volumes of organic solvents for purification. This stresses out one of the two main drawbacks of molten salt synthesis: the difficulty to fully eliminate the salt reaction medium from the product and then to reach high purity materials. The second important drawback is the corrosiveness of many salts *versus* a wide range of materials. Hence, the reactor walls must be carefully selected according to the nature of the salts envisioned, while ensuring compatibility with the reagents.

Many materials developed in molten salts are also accessible through aqueous chemistry processes described above. This is the case of binary metal oxide nanomaterials, for which the interested reader is directed towards a recent report for an exhaustive view of their syntheses in molten salts.[6] In the next sub-sections, we focus on the design in molten salts of nanomaterials that are difficult to reach through other routes.

6.4. Molten salts enabling complex structures and control of oxidation states in multicationic oxide nanomaterials

Because reactions in liquids are usually faster than solid-state reactions, molten salts enable decreasing the reaction temperature for a wide range of solids, thus limiting the energy input required for crystallization, restraining crystal growth and then enabling the recovery of low dimensionality materials. This is well exemplified by the synthesis at 600 °C of 20 nm to 100 nm-thick platelets of $Sr_4Mn_3O_{10}$ from potassium permanganate and molten strontium hydroxide, acting both as molten salt medium and reagent (Fig. 17A),[168] while the solid-state synthesis requires higher temperatures. Molten salt synthesis is also a convenient route towards pyrochlore nanomaterials $A_2B_2O_7$ where

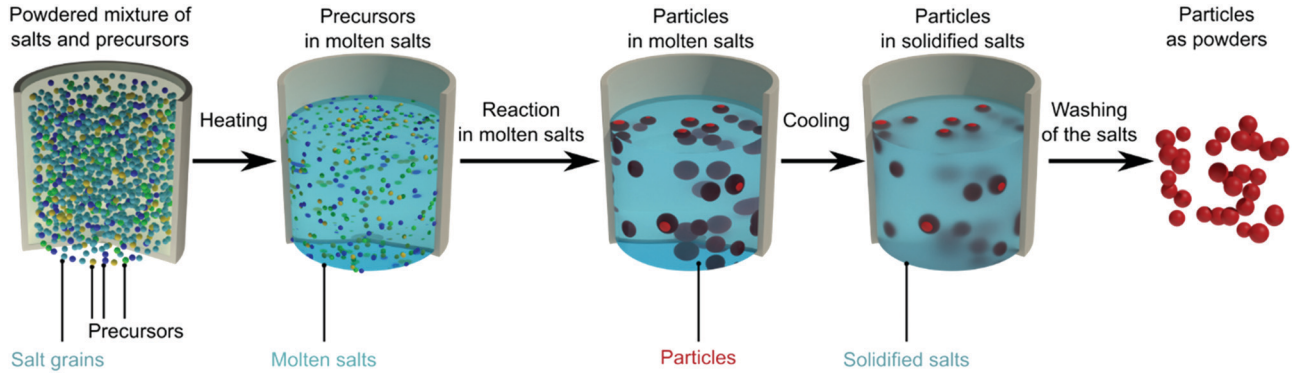

Fig. 16 Basic procedure for molten salt synthesis.

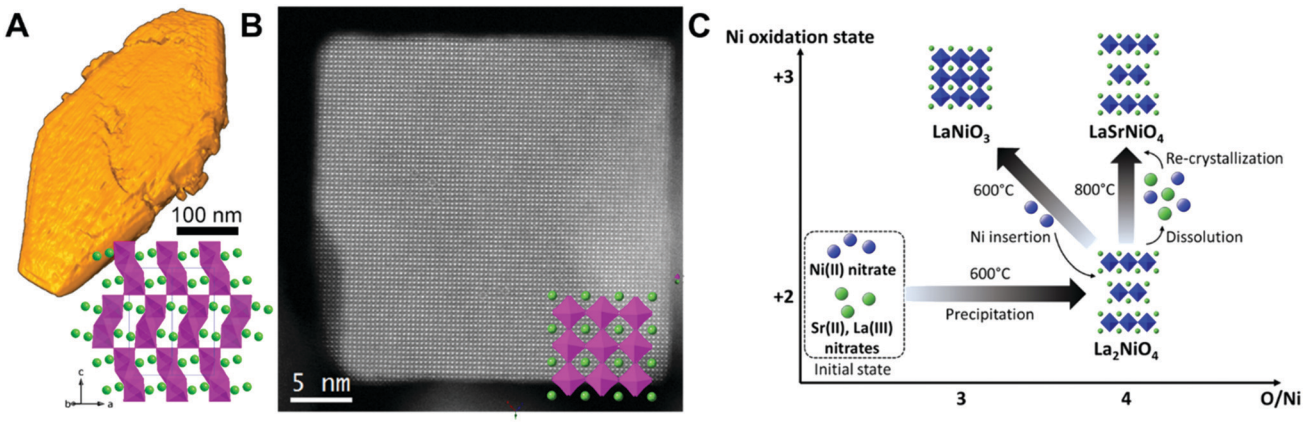

Fig. 17 Structural control in molten salt synthesis. (A) STEM tomographic reconstruction of a $Sr_4Mn_3O_{10}$ platelet obtained in molten strontium hydroxide. Reproduced from ref. 168 with permission of the Royal Society of Chemistry. (B) STEM-HAADF image of a $La_{2/3}Sr_{1/3}MnO_3$ nanocube obtained in molten KNO_3. Reproduced from ref. 169 with permission of Wiley-VCH Verlag GmbH & Co. KGaA. (C) Crystallization sequence and mechanisms from La_2NiO_4 to $LaNiO_3$ and $LaSrNiO_4$ in molten $NaNO_2$. Reproduced with permission from ref. 170. Copyright 2020 American Chemical Society.

A = La, Pr, Nd, Gd, Er, Lu, and Y and B = Ti, Zr, and Hf.[6] Most molten salt syntheses of pyrochlores have been performed in eutectic alkali nitrate mixtures ($NaNO_3$–KNO_3), enabling a decrease of reaction temperatures and a decrease in particle size compared to high temperature solid-state processes.[6]

Besides the formation of pyrochlores, molten alkali nitrates have been instrumental in reaching manganate perovskite nanomaterials, by decomposing lanthanide, alkaline earth and manganese nitrates at *ca.* 550–700 °C. Although these compounds are reachable in the same temperature range by sol–gel Pechini methods involving solid-state calcination,[171] the use of molten salts has been a way to reach higher crystallinity. In particular, by combining molten potassium nitrate with a steep temperature profile that relies on using a pre-heated oven and on temperature quenching after a plateau, we could trigger a burst of nucleation while avoiding irreversible large-scale aggregation. The procedure then delivered highly faceted $La_{2/3}Sr_{1/3}MnO_3$ nanocubes with a narrow size distribution and a high crystallinity (Fig. 17B).[169] These morphological and structural characteristics could not be achieved without the use of molten salts and without the dedicated temperature profile. These features deeply impact properties. In particular, the single crystal nanocubes exhibit new spin transport driven by surface spin disorder.[169] We have also demonstrated the very high activity and stability of these nano-objects in electrocatalysis of the alkaline oxygen reduction reaction,[172] again thanks to their high surface area and to their crystallinity. The procedure was then extended to a range of $AMnO_3$ nanocrystals, where the A sites are occupied by La, Pr, Sr, and/or Ca.[173] Noteworthily, a similar approach was reported for $BaTiO_3$ nanowires,[174] $SrTiO_3$ nanocubes,[174] and $Ca_{1-x}Sr_xTiO_3$ ($0 \leq x \leq 1$) nanocubes[175] by reacting TiO_2 with Ba, Ca and Sr oxalates and a nonionic surfactant in molten sodium chloride. The reaction involved thermal decomposition of the organic species, as in the Pechini method, but the molten salt provided a flux for better control of nucleation and growth, and then of faceting of cubic nanoparticles.

While molten alkali nitrates are sufficiently oxidizing to stabilize $Mn^{3+/4+}$ oxidation states, the ability of molten salts to provide reactive O^{2-} species can also guide the reaction pathway. The propensity of an oxosalt to deliver O^{2-} anions is described by the Lux-Flood oxo-basicity, which corresponds to the following equilibrium in the case of nitrates:[176]

$$NO_3^- \rightarrow NO_2^+ + O^{2-}$$

where NO_2^+ cations further recombine with excess NO_3^- to yield NO_2 and O_2.[176] Metal cations are then oxoacids that accept/react with O^{2-} anions to yield oxides. Direct comparison with Brønsted acid–base reactivity in aqueous synthesis indicates that an increase in the oxo-basicity of the molten salt will not only favor oxygen-rich products, but may also be used to incorporate many cations in the same compound, just like coprecipitation in basic aqueous media.[22] A good example of this ability to change reaction pathways by the oxo-basicity of the molten salt has been provided recently,[177] where the reagent ratio corresponding to the synthesis of $La_{2/3}Sr_{1/3}MnO_3$ nanocubes in molten potassium nitrate has been adjusted to match the composition of the Ruddlesden–Popper layered perovskite $La_{0.5}Sr_{1.5}MnO_4$. Despite this change of the reagent ratio, only the pseudo-cubic perovskite $La_{2/3}Sr_{1/3}MnO_3$ could be achieved at 600 °C. Increasing the temperature at 800 °C enabled partial formation of the layered perovskite, with still some unreacted A-site metal cations. In order to bring the reaction to completion, molten potassium nitrate was replaced by molten sodium nitrite, with a dissociation constant towards O^{2-} that is 10^{10} higher than for KNO_3.[176] This large increase of the oxo-basicity of the molten salt was key to enable the recovery of pure $La_{0.5}Sr_{1.5}MnO_4$. The analysis of the medium quenched at several reaction times revealed that the reaction proceeded through the formation of the pseudo-cubic perovskite, $La_{2/3}Sr_{1/3}MnO_3$, followed by its dissolution and the reprecipitation of the layered perovskite phase. Again, a direct parallel under geological crystallization conditions can be drawn, for which the primary role of the O_2 fugacity has been detailed at the beginning of this review. Interestingly, in the case of molten salt syntheses, oxygen species do not act only as oxidizing species, but also as basic species.

While the molten salt composition enables tuning of the redox properties and oxo-basicity of the melt, temperature can also play a significant role in the selection of the reaction pathway. This has been shown recently with the selective transformation of the Ruddlesden–Popper perovskite La_2NiO_4 into $LaNiO_3$ and $LaSrNiO_4$ at 600 and 800 °C, respectively (Fig. 17C).[170] Again, the analysis of quenched media at different reaction times provided information on reaction mechanisms. We have highlighted the incorporation of nickel ions into La_2NiO_4 to form $LaNiO_3$ at low temperatures with retention of particles size and morphology, while higher temperature triggered dissolution of La_2NiO_4 and re-crystallization of $LaSrNiO_4$. The case-study of nickelate perovskites also highlights the significant role of the metal oxidation state of the reagents on the course of the reactions. Indeed, nickel(II) salts yield first a $La_2Ni^{II+}O_4$ layered perovskite that evolves in a second step. Hence, the oxo-basicity of the molten salt appears as the prime driving force of solid formation. Then, the redox reactivity of the molten salt acts in the subsequent evolution of the first solid formed.

6.5. Molten salts for size and morphology control of oxide nanomaterials

Molten salts offer in some cases the ability to control particle size. This has been shown for micronic particles of lead-based perovskites $Pb(Mg_{1/3}Nb_{2/3})O_3$ and $Pb(Fe_{1/2}Nb_{1/2})O_3$ synthesized in sulfates and chlorides,[178] for which the particle size decreased with an increase in temperature, the heating rate and the concentration of precursors. These results can be interpreted by enhanced nucleation. Similar results were obtained for $NiFe_2O_4$ submicroplates[179] formed into molten NaCl–KCl, with an overall size that decreased with an increase in the concentration of metal precursors, or for spinels and pyrochlore particles, among others, with size increasing along with temperature.[6]

Occurrences of morphological control by using molten salts as reaction media are mostly related to submicronic crystals. They encompass cases of titanates,[180] zirconates,[181] ruthenates[182] and ferrites,[183] with morphologies usually adjusted by the temperature profile, the molten salt composition and the molten salt-to-transition metal precursor ratio. However, the rationale of morphological control is still to be decrypted. While several studies have ascribed specific faceting in molten salts to surface–anion interactions that modify facet energies, as in $La_{1-x}Sr_xCoO_3$ (x = 0, 0.3) perovskite submicronic crystals,[184] during the last few years Rimer *et al.* have made a significant step forward in the identification of important parameters for morphological control. The authors have studied the relationship between the nature of the molten salts and the morphology of MgO[185] and NiO[186] submicron crystals (Fig. 18) from the decomposition of several Mg and Ni hydrated or anhydrous nitrates and chlorides. The formation of MgO octahedra with high index facets {111} was enabled by the occurrence of molten reaction intermediates or media, and/or by the presence of water.[185] A similar study on NiO crystals[186] (Fig. 18A) demonstrated the ability to tune the morphology of NiO crystals between octahedral (NiO{111}), cubic (NiO{100}) and trapezohedral (NiO{311}) morphologies, exposing {111}, {100} and {311} facets, respectively. NiO{111}, NiO{100} and NiO{311} were obtained from hydrated nickel(II) nitrate in molten $LiNO_3$, $NaNO_3$:KNO_3 and NaCl:KCl eutectic mixtures, respectively. The study was recently extended to mixed cationic (Ni,Mg)O crystals,[187] highlighting the formation of solid solutions into molten NaCl:KCl eutectic mixture with crystal shapes governed by the major cation: octahedral and trapezohedral crystals for Mg-rich and Ni-rich mixed oxides, respectively. Morphological selection according to the anion and cation(s) of the molten salts was originally postulated[187] to arise from the formation of different nickel(II) complexes involved in the growth of the crystals. By using DFT modeling, Rimer *et al.*[188] proposed recently more in-depth insights into morphological control. First, by calculating the energy of the different facets, they explained the formation of NiO{111} octahedra in air, and presumably in $LiNO_3$[186] by the stabilization of these facets due to hydroxylation, where hydroxo groups arise from the hydrated nickel chloride precursor. Second, they observed that the most stabilized facets in contact with potassium chloride were the {311} facets, and that the most stabilizing configuration corresponded to a contact with crystalline potassium chloride, which can occur by ordering in molten salts in the vicinity of surfaces (Fig. 18B). Therefore, the high index morphology seems to arise from selective adsorption and ordering

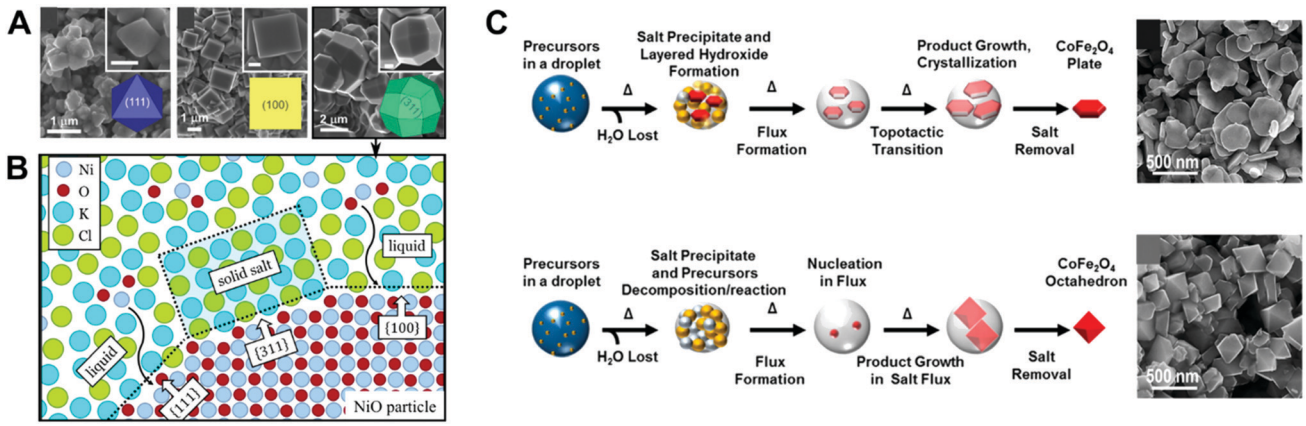

Fig. 18 Morphological control of oxide submicronic crystals in molten salts. (A) {111} octahedral, {100} cubic and {311} trapezohedral NiO crystals obtained from $Ni(NO_3)_2{\cdot}6H_2O$ in molten $LiNO_3$, $NaNO_3$–KNO_3 and NaCl–KCl, respectively. Reproduced from ref. 186 with permission of Wiley-VCH Verlag GmbH & Co. KGaA. (B) Schematized results from DFT modeling representing selective growth of NiO facets driven by adsorption of crystalline potassium chloride on the {311} facets yielding trapezohedral crystals. Reproduced from ref. 188 with permission of Wiley-VCH Verlag GmbH & Co. KGaA. (C) Morphological control by aerosol-assisted molten salt synthesis of (D) cobalt ferrite octahedra and plates. Reproduced with permission from ref. 189. Copyright 2015 American Chemical Society.

of crystalline potassium chloride on the {311} facets, which are stabilized and exhibit slower growth.

The possibility to tune the morphology of submicronic metal oxide crystals with the nature of the molten medium was also shown by combining molten salts with spray pyrolysis, as pioneered by Skrabalak *et al.*[189,190] A first example of oxides obtained with this process[190] concerns the formation of α/γ-Fe_2O_3 hexagonal plates, and α-Fe_2O_3 rhombohedral particles from α/γ-Fe_2O_3 precursor particles depending on the cation of the molten carbonate used. Shape control was associated with entangled phenomena, encompassing competition between homogeneous nucleation and seeded growth, as well as selective facet stabilization by surface–ion interactions. Aerosol-assisted molten salt synthesis was further used to selectively obtain cobalt ferrite octahedra and plates (Fig. 18C),[189] with molten sodium molybdate and sodium carbonate, respectively. In the former case, hydrated iron(III) and cobalt(II) sulfates fully dissolve in the molten medium, then crystallization of the spinel occurs during cooling down by homogeneous nucleation to yield the octahedral equilibrium shape. In molten carbonate, the precursor metal salts first react to form an Fe, Co layered double hydroxide (LDH), which transforms topotactically into the spinel. The transformation is isomorphic, yielding a spinel plate-like morphology from the intermediate LDH plates.

6.6. Molten salts for the formation of metal non-oxide nanomaterials from homogeneous mixtures

Besides oxygenated species, molten salts have also been used for about ten years as versatile reaction media to synthesise various metal non-oxides. An exhaustive list of non-oxide nanomaterials has been delivered recently by Gupta and Mao[6] and by Li *et al.*[191] Hence, below we discuss the chemical concepts underlying the ease or difficulty to perform the synthesis of the different families of materials currently accessible. We highlight the advantages and disadvantages of molten salts for these families of materials compared to more common synthesis processes, and we provide also some most recent advances in each of these families.

Ionic compounds such as metal fluorides AEF_2 (AE = Ca, Sr), LnF_3 and $NaLnF_4$ (RE = La, Ce, Y) are so stable that they can form even in the presence of an oxygen source. Hence, they are relatively simple to target by coprecipitation from metal nitrates and sodium fluoride NaF in molten nitrates ($NaNO_3$, NH_4NO_3) at 200–400 °C,[192–194] as reviewed by Fedorov and Alexandrov.[195] In particular, the NaF/Ln initial ratio, the reaction temperature and reaction time enable controlling the morphology of LnF_3 and $NaLnF_4$ and $NaBiF_4$:Yb^{3+}/Er^{3+} submicronic crystals in molten NH_4NO_3.[196,197] Upconverting $NaYF_4$:Yb^{3+}/Er^{3+} could also be achieved by using similar processes,[195] although colloidal synthesis enables more precise control of nanocrystal dispersion and size distribution thanks to organic ligands.

Fluorides set aside, the presence of oxygen during the synthesis is detrimental to the formation of most non-oxide compounds. Therefore, molten media enabling the formation of such products are usually selected to be oxygen-free. In most cases, molten alkali halides and their eutectic mixtures are prime candidates to run the synthesis of metal non-oxides. These salts are mostly described as not taking part in the reaction pathway. However, only a little is known at present of the reaction mechanisms during solid formation in such media and the rationale we have drawn above in terms of molten salt acid–base properties for oxides into oxo salts is not achieved yet in molten halides for nanomaterial synthesis. From metal chalcogenides to nitrides, silicides, carbides and borides described below, the covalency of chemical bonds increases. Hence, the requirement for energy input to trigger ordering of crystal structures, in other words crystallization, is more stringent and the temperature range of syntheses increases.

In the context of molten salt synthesis, chalcogenides encompassing sulfides, selenides and tellurides fall into a family of materials similar to fluorides in the sense that they do not require a large energy input for crystallization. Kanatzidis and coworkers nicely demonstrated the interest of performing flux synthesis of such materials to discover new compounds of complex compositions in the bulk state.[198–200] The approach has not been applied yet to the synthesis of nano-objects of new compounds, but numerous examples have already demonstrated the possibility to synthesize nanomaterials of known metal chalcogenides, mostly in molten alkali halides. Among others, technologically important materials were achieved, including $NaInS_2$[201] for solar cells (Fig. 19A and B), and two-dimensional dichalcogenides MoS_2, WS_2, TiS_2, $MoSe_2$ and WSe_2, by using K_2S and selenium as chalcogenide sources.[202]

Metal nitrides have been less explored in molten salts than fluorides and chalcogenides. The few examples reported rely on similar routes as described above, including the production of Ta_3N_5 nanoplates and octahedra photocatalysts for water splitting (Fig. 19C–F) by aerosol-assisted molten salt synthesis, using ammonia as the nitrogen source.[203] The molten salt medium enabled reaching high crystallinity, which enhanced the photocatalytic performances of the nanomaterials. Likewise, N_2 was used as the nitrogen source in a molten $NaCl–MgCl_2$ mixture to react with TiO_2 and magnesium. The latter was used as a reducing agent to scavenge oxygen and yield titanium nitride TiN nanoparticles at 600 °C.[211]

Free-standing metal silicide nanomaterials are only scarcely reported, whatever the synthesis methods. It is just recently that molten salts have been envisioned for their synthesis. Again, alkali halides are adequate molten media to trigger the reaction between oxygen-sensitive silicon sources and metal precursors. While the latter are usually metal halides,[204,212] as for most of the materials families described above, there are only a few available Si sources that can operate at temperatures between 300 and 800 °C and be maintained in a liquid medium without the need of pressurized vessels. Elemental silicon powders have been used to produce $CrSi_2$,[212] while silica has been combined with molybdenum oxide to form $MoSi_2$ nanostructures by exothermic magnesiothermal reduction in molten NaF. This procedure relates to self-propagating reactions, where the exothermicity of the reaction triggers a strong increase of the temperature of the medium.[213] More recently, the use of sodium silicide Na_4Si_4[214] has been explored (Fig. 19G–J).[204] This source of Si^{1-} species is highly reducing and can react with metal halides at relatively low temperatures, thus enabling the synthesis of nickel silicide nanocrystals.[204] Adjusting the temperature and the reagent ratio yielded selective synthesis of Ni_2Si and NiSi at 300 and 500 °C, respectively. Under oxidative and basic aqueous conditions, the nano-objects undergo surface oxidation, which yields highly active electrocatalysts for the oxygen evolution reaction, made of a shell of electrocatalytically active nickel oxyhydroxide and a core of electrically conductive silicide enabling charge percolation through the electrode. Very recently,[215] the low vapor pressure of molten alkali iodides was used on purpose to enhance the reactivity of silicon nanoparticles with metal salts. This reaction produced bimetallic nickel iron silicide nanocrystals and SiI_4 as the byproduct. The latter is volatile and could be extracted from the molten medium under dynamic vacuum while the molten salt was retained. As a result, the product was purified *in situ* and the reaction equilibrium was shifted, thus increasing the reactivity of silicon nanoparticles and conversion into multimetallic silicide nano-objects. Again, these nanoparticles undergo silicon leaching in the first atomic layers, leading to surface nickel iron oxyhydroxide that acts as a highly efficient electrocatalyst[215] of water oxidation by benefiting from electron percolation through the conductive silicide cores.

Carbides can also be produced in molten salts. The reported syntheses rely on alkali or alkaline earth halides as reaction media enabling the use of temperatures as high as 1300 °C, to deliver a wide range of binary metal carbides as well as multinary compounds such as Cr_3AlC, Ti_3AlC_2 and $(Ta_{0.25}Nb_{0.25}Ti_{0.25}V_{0.25})C$.[6,216–223] The carbon source is elemental carbon in various forms, such as graphite, nanotubes, and nanodiamonds,[222] but can also be polymers. The metal precursor can be metal salts, elemental metal, or metal oxides. Molten salt syntheses deliver carbides of high crystallinity, which is beneficial for a range of properties, for instance voltammetric detection of antibiotics.[221]

The crystallization of most boron-rich borides requires high temperature processes because of their covalency. Molten salts media offer an opportunity to decrease the synthesis temperatures and enable the recovery of nanoscaled objects. We have first demonstrated the generality of this approach by reacting sodium borohydride with metal salts into molten alkali halides,[205,206,224,225] to deliver a wide range of nanoscaled borides with various metals and metal-to-boron ratios with temperature and reagent ratios as the primary experimental levers (Fig. 19K–M). The approach has been further extended to the use of a tin melt to react elemental boron with metal chlorides and form mostly submicronic particles.[226] By delivering a range of new nanoscaled metal borides, molten salt synthesis has opened routes to investigate the role of the nanoscale on the properties of metal borides: CO_2 methanation catalysis,[225] hydrogen evolution and oxygen evolution electrocatalysis,[227,228] superhardness,[229] high-pressure phase transformations,[230] magnetism[231] and thermoelectricity,[207] among others.

While combining several metals together in the same compound is relatively simple, it is more arduous to design multianionics, since these compounds tend to decompose into their monoanionic counterparts. Hence, the synthesis of such compounds can largely benefit from a decrease in reaction temperatures, in order to facilitate their recovery. Molten salts then appear as interesting reaction media to design multianionics, such as oxynitrides $LaTaON_2$, multinary oxychlorides and oxyfluorides;[6] nonetheless, this field is still poorly explored.

In some cases, the precise selection of molten salts can be instrumental in reaching the targeted phases. This has been well exemplified by Alivisatos *et al.*,[208] who obtained Pt_3Y, Pt_3Sc and Pt_3Lu, and Au_2Y early-late intermetallic nanoparticles (Fig. 19N–O) from the reaction of the corresponding metal

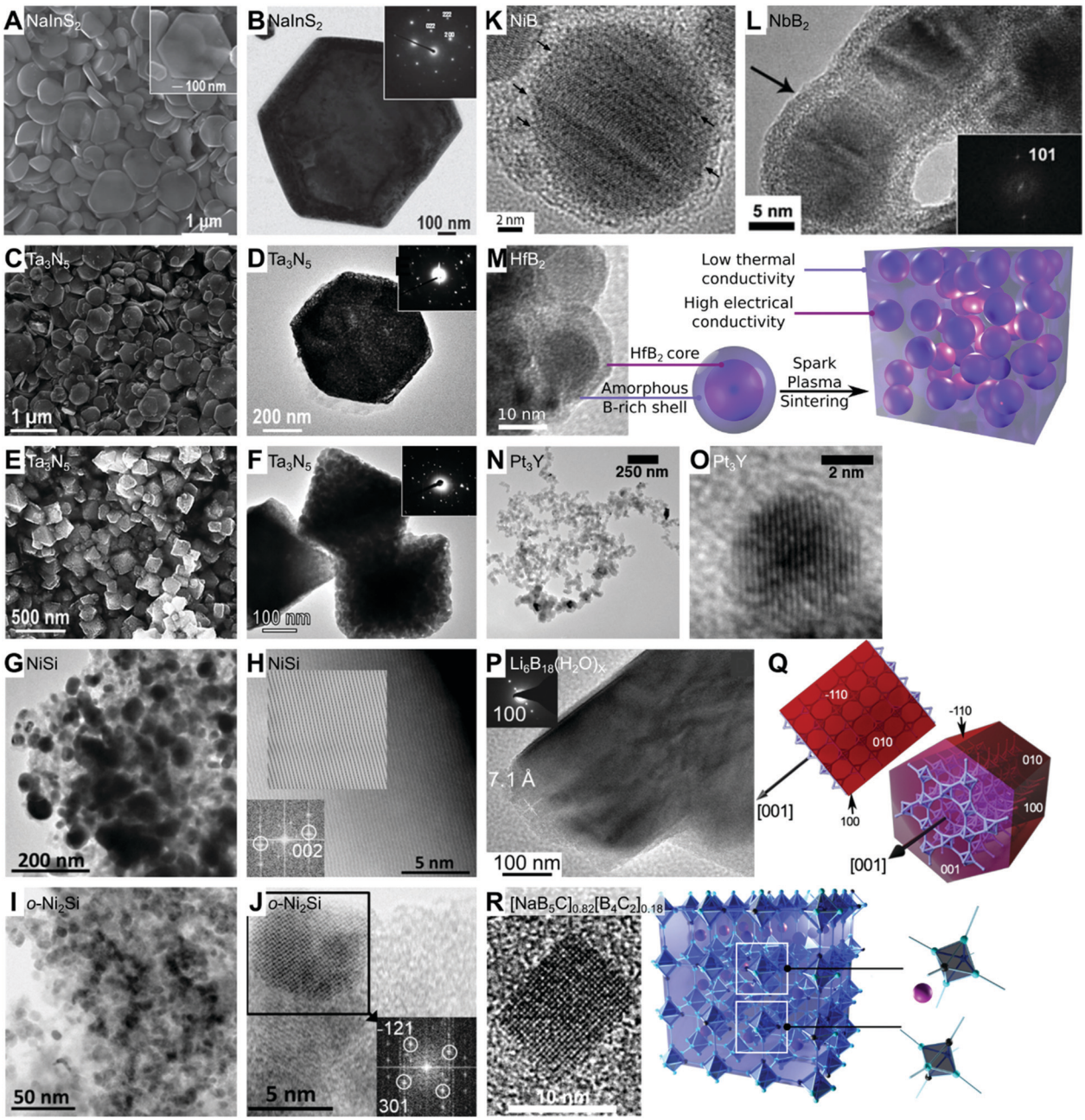

Fig. 19 SEM and TEM images of non-oxide nanomaterials synthesized in molten salts. (A and B) $NaInS_2$ platelets. Reproduced from ref. 201 with permission of Wiley-VCH Verlag GmbH & Co. KGaA. Ta_3N_5 (C and D) nanoplates and (E and F) octahedra water splitting photocatalysts. Reproduced from ref. 203. (G and H) NiSi and (I and J) *o*-Ni_2Si nanocrystals obtained in molten alkali chlorides from sodium silicide Na_4Si_4 and nickel chloride. Reproduced from ref. 204 with permission from the Royal Society of Chemistry. (K) NiB, (L) NbB_2, and (M) HfB_2 metal boride nanocrystals obtained from metal chlorides and sodium borohydride reacted in molten alkali halides. The scheme in (M) shows a bulk nanocomposite with controlled electrical and heat transport properties obtained by Spark Plasma Sintering of HfB_2 powders. Reproduced respectively from ref. 205–207 with permission from the Royal Society of Chemistry, Wiley-VCH Verlag GmbH & Co. KGaA and the American Chemical Society, copyright 2021. (N and O) Early–late intermetallic nanoparticles of Pt_3Y obtained in molten borohydrides. Reproduced with permission from ref. 208. Copyright 2017 American Chemical Society. (P) $Li_6B_{18}(Li_2O)_x$ nanorods and (Q) the corresponding crystallographic orientation, where Li^+ ions were provided by the molten LiI–KI mixture. Reproduced with permission from ref. 209. Copyright 2020 American Chemical Society. (R) $[NaB_5C]_{0.82}[B_4C_2]_{0.18}$ nanocrystals, corresponding crystallographic orientation and local order, where Na^+ were provided by molten NaI. Reproduced with permission from ref. 210. Copyright 2021 American Chemical Society.

chlorides in molten trialkylborohydrides $NaEt_3BH$ and KEt_3BH, which melt above 30 and 95 °C, respectively. Upon a first heating step at 200 °C followed by an intermediate removal of reduction by-products and further annealing at 650 °C, the expected nanoparticles could crystallize. The use of molten hydride media was required to trigger the reduction of early

metal cations with very negative redox potentials and to reach temperatures high enough to crystallize such compounds. A similar approach using molten $NaBH_4$ was proposed by Mattox *et al.*[232–234] to reach LaB_6 nanoparticles from lanthanum trichloride, although in this specific case and as described above, so much reductive media are not necessary to obtain this compound.

It is informative to note that contrary to metal oxides described above, occurrences of particle size control of non-oxides in molten salts are rare. The ability to decrease the particle size of metal borides by increasing the boron-to-metal source ratio has been described.[93] This trend was ascribed to the determinant role of nucleation for such compounds, which are hard to crystallize due to the presence of directional covalent bonds. Further work should be directed in the future to target size control comparable to the achievements of colloidal synthesis.

6.7. Molten salts for the formation of transition metal-free materials and nanomaterials

Molten salts also appear as efficient media to trigger the formation of materials free of transition metals. About a decade ago, molten alkali and zinc halides were used to synthesize a highly crystalline layered carbon nitride[167,235] from the decomposition of various organic precursors such as dicyandiamide. Afterwards, other C,N-based materials could be achieved, including covalent triazine and heptazine-based frameworks into molten $ZnCl_2$,[236] and porous or nanostructured carbons by decomposition of sugars in molten alkali halides[237] or of ionic liquids in the presence of molten mixtures of $ZnCl_2$ with alkali chlorides.[238] Other solids based on silicon could also be achieved in molten salts, such as SiC[239] and $LiSi_2N_3$,[240] the latter being obtained from melamine as the nitrogen source.

Transition metal-free B-based nanomaterials are other covalent solids for which the use of molten salts enables a decrease in the synthesis temperature and then a decrease in the particle size compared to other protocols. This is well exemplified by the synthesis of water-dispersible 5 nm BCNO nanoparticles in molten alkali halides from $NaBH_4$ and urea or guanidine.[241] Modifying the reagent ratio enables adjusting the composition of the particles and then the luminescence wavelength. By further controlling the temperature of synthesis and precursor ratio, BCN nanosheets could also be designed, with high performances for fast cycling Li-ion batteries.[242] More recently, we have shown that nanocrystals of alkali boron-based solids can be achieved in molten salts. We could obtain the first occurrence of $Li_6B_{18}(Li_2O)_x$ (Fig. 19P–Q) nanocrystals[209] where Li^+ was provided by the eutectic molten mixture LiI–KI. By using NaI as the molten medium and by adding a polymer as the carbon source, we could change the reaction pathway and obtain $[NaB_5C]_{0.82}[B_4C_2]_{0.18}$ nanocrystals[210] (Fig. 19R) with a stoichiometry that deviates from the ideal one NaB_5C reported for the bulk phase.[243,244] This shows how molten salt synthesis can drive unknown stoichiometry deviations, and then the formation of new solids at the nanoscale. These nanocrystals are efficient precursors to nanoparticles of boron carbide after removal of sodium by thermal annealing, thus paving the way to superhard materials.

6.8. Molten salts for the formation of non-oxide nanomaterials by post-modification

Some recent studies have focused on the use molten salts to modify pre-formed solids. In particular, the last few years have seen the emergence of protocols for the post-modification of solids while enabling the recovery of nanostructures, thanks to the low temperatures involved and to the dilution of reagents into a liquid medium. Two tracks can be highlighted: treatment of pre-made nano-objects and reactions of bulk solids to form nanostructures.

In the first strategy, after demonstrating the possibility to disperse nanoparticles into molten salts,[245] the group of Talapin *et al.* explored these liquids as thermal annealing media. CsBr–KBr–LiBr was used to maintain GaAs nanocrystals dispersed during treatment at 500 °C in the presence of gallium triiodide.[246] This procedure resulted in the alleviation of Ga vacancies and crystal disorder, thus yielding highly crystalline GaAs nanocrystals, which enabled the emergence of size-dependent excitonic transitions. The strategy was further applied to the design of $In_{1-x}Ga_xP$ and $In_{1-x}Ga_xAs$ ($0.2 < x < 0.9$) nanocrystals.[247] These ternary III–V semiconductors could be targeted by cation exchange in pre-synthesized InP and InAs nanocrystals, but their covalent character makes Ga^{3+} diffusion very slow. Hence, cation exchange must be thermally activated. Again, the use of molten CsBr–KBr–LiBr in which InP and InAs can be dispersed in the presence of GaI_3 at 380–450 °C enabled overcoming the diffusion energy barrier and yielded $In_{1-x}Ga_xP$ and $In_{1-x}Ga_xAs$ ($0.2 < x < 0.9$) while maintaining the nanocrystal size. The resulting ternary quantum dots exhibited composition-dependent absorption and emission features.

In the previous examples, molten halides have been used as inert liquid media. It is possible also to use the reactivity of these melts to modify the composition of pre-made solids. In 2016, Urbankowski *et al.*[248] reported the delamination of the layered nitride Ti_4AlN_3 (Fig. 20A) in a molten LiF–NaF–KF mixture. Al atoms were removed from the interlayer space as X_3AlF_6 salts (X = Li, Na, and F). Although this process indicated the occurrence of a redox reaction between the melt and intercalated Al atoms, it was only a few years later that Li *et al.*[249] investigated a similar approach by explicitly searching redox reactivity to transform layered MAX phases (Fig. 20B) – $M_{n+1}AX_n$ made of $M_{n+1}X_n$ sheets (M = transition metal, especially terminating the perimeter layers, C = carbon or nitrogen sandwiched between M layers) interleaved with A layers (A is usually a 13–16 group element) – in molten $ZnCl_2$, with Ti_3AlC_2, Ti_2AlC, Ti_2AlN, and V_2AlC. At 550 °C, Al atoms in these compounds underwent galvanic replacement by Zn atoms, thus yielding new MAX phases Ti_3ZnC_2, Ti_2ZnC, Ti_2ZnN and V_2ZnC. According to calculations, these compounds are unstable at 1300 °C, the usual temperature for MAX phase synthesis. These stability considerations support again the use of molten salts to decrease the synthesis temperature and enable the discovery of phases that could not be achieved at the high temperatures

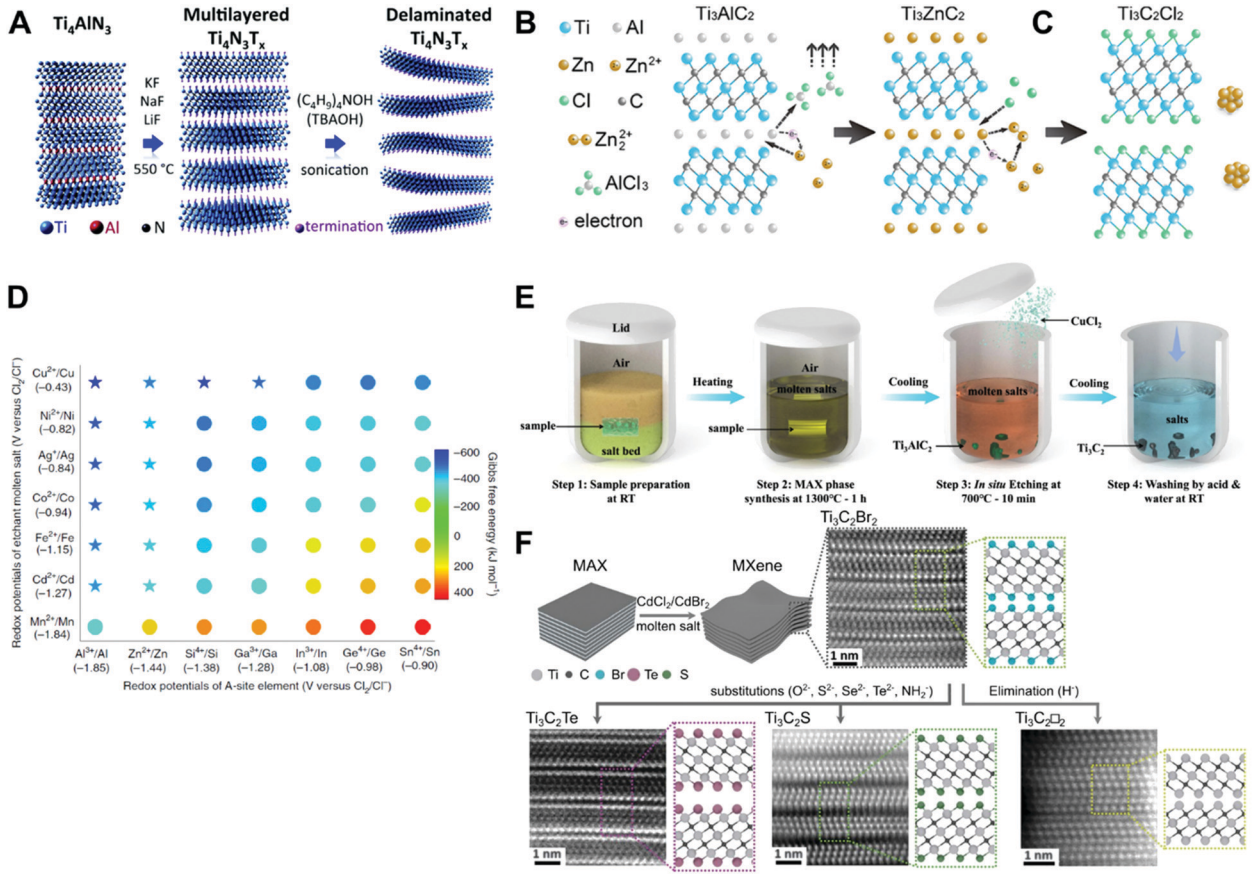

Fig. 20 Reactive molten salts for post-modification of layered MAX phases and design of new bidimensional carbides and nitrides. (A) Exfoliation of Ti_4AlN_3 in molten LiF–NaF–KF. Reproduced from ref. 248 with permission of the Royal Society of Chemistry. (B) Transformation of Ti_4AlN_3 into Ti_3ZnC_2 and (C) exfoliation of Ti_3ZnC_2 in molten $ZnCl_2$. Reproduced with permission from ref. 249. Copyright 2019 American Chemical Society. (D) Rational choice of the etching melt to delaminate MAX phases according to the redox activity of the melt. Reproduced from ref. 250 with permission of Springer Nature. (E) Combined molten salt synthesis, etching and exfoliation to produce directly $Ti_3C_2T_x$ from the constitutive elements in molten NaCl–KCl under air. Reproduced from ref. 252 with permission of Springer Nature. (F) Functionalization of MXenes in molten salts. Modified from ref. 253 with permission of The American Association for the Advancement of Science.

required for solid-state reactions. Further increase of the $ZnCl_2$-to-MAX phase triggered exfoliation of Ti_3ZnC_2 and yielded the two-dimensional $Ti_3C_2Cl_2$ MXene (Fig. 20C), a single sheet Ti_3C_2 terminated by Cl atoms. Galvanic etching in molten metal halides was further extended[250] to MAX phases such as Ti_3SiC_2, Ti_3AlCN, Nb_2AlC, Ta_2AlC and Lewis acid melts different than $ZnCl_2$: $CuCl_2$, $CdCl_2$, $FeCl_2$, $CoCl_2$, AgCl, and $NiCl_2$. The rational choice of the etching melt could be achieved based on the calculated redox potential MS^{2+}/MS – where MS is the cation of the molten salt – compared to the redox potential A^{n+}/A for the A element in the MAX phase (Fig. 20D). The approach yielded the corresponding MXenes with Cl and O terminations. $Ti_3C_2T_x$ (T = Cl and O) exhibited high electrochemical Li^+ storage capacity in a non-aqueous electrolyte, even at a high charge–discharge rate. Molten salts were also demonstrated to efficiently shield the reagents and products from oxidation by air, thus enabling the synthesis of MAX phases Ti_3SiC_2, Ti_2AlN and of the MAB phase MoAlB without the need for an inert atmosphere.[251] Then, the abilities of molten salts to etch, exfoliate and protect MAX phases from oxidation were combined (Fig. 19E) to produce directly $Ti_3C_2T_x$ from elemental Ti, Al and C in a single reaction medium NaCl–KCl mixture.[252]

As $CuBr_2$ and CuI could also be used for etching,[250] the molten salt exfoliation method opened the way to Br and I terminations instead of Cl. This strategy was further used[253] to produce *e.g.* Nb_2CCl_2 from Nb_2AlC, but also $Ti_3C_2Br_2$ from Ti_3AlC_2 etched in the molten $CdCl_2$–$CdBr_2$ mixture. While Nb_2CCl_2 showed a superconductive behavior below 6 K, the largest strength of the method lies in its chemical versatility. Indeed, the M–Cl and especially M–Br bonds are sufficiently labile to engage into further anion exchanges in molten CsBr–KBr–LiBr (Fig. 19F). For instance, Br in $Ti_3C_2Br_2$ could be exchanged with O, S, Se, Te, and NH, while treatment with LiH was claimed to eliminate terminations and yield $Ti_3C_2\square_2$. Hence, molten salts open an avenue to discover new two-dimensional materials.

In this section, after highlighting the importance of molten salts in the natural crystallization of gems, we have sketched out the basic principles underlying syntheses in molten salts. In particular, we have analysed how the chemistry of molten

salts and the nature of reagents can be adjusted to tune the structural and morphological features, hence the properties, of a wide range of nanomaterials from multicationic oxides to non-oxides. Our knowledge of reaction mechanisms in these media remains very limited and would benefit from *in situ* studies. Such methods are difficult to implement in high temperature liquids. Below, we describe high pressure materials syntheses, which make significant use of *in situ* characterization, and which could then inspire *in situ* approaches in high temperature environments.

7. High pressure transformations: focus on nanomaterial synthesis

7.1. Importance of high pressures in Earth and planetary processes

More than 99% of the Earth's mass is at pressures exceeding 1 GPa. Also, the Earth's internal temperature increases with depth until around 5000 K in the center of the core. This temperature profile is mainly due to the heat released by the spontaneous radioactive decay of ^{235}U, ^{238}U, ^{40}K, and ^{232}Th present in the mantle as well as by the frictional heat left over from the initial collisions of the planetoids that have aggregated to form present day size planet Earth. Therefore, the Earth is a ''natural extreme chemistry laboratory'' allowing for the existence of many dense minerals, for which one can study the chemical properties, structure and thermodynamic stability. Many compounds that exist deep in the Earth have significant implications for fundamental Earth sciences for three reasons. First, a better understanding of the mechanisms associated with their synthesis inside the Earth can provide information on the origin of important species. For example the synthesis of methane under the (P,T) conditions of the Earth's upper mantle is broadly studied to understand its main origin: organic or, according to the abiogenic theory, from reactions under extreme conditions between H_2O, FeC and CO_2. Second, compounds originating in the deep Earth's interior bring constrains on the models of the inner structure, chemical composition and more generally dynamic models for the formation and evolution of our planet. Third, many solids, which form deep in the Earth exhibit properties without equivalent among room pressure phases. Some high-pressure solids from the Earth's upper mantle ($<$700 km) are released to the Earth's surface *via* volcanic eruptions. Among these materials, diamond is probably the most precious material with technological implications because of its wide range of extreme properties.

7.2. Diamond: original driving force for the development of high-pressure research

Since diamond is the thermodynamic stable allotrope of carbon under high pressure, it is mainly found in the Earth under extreme conditions, *i.e.* at depths over $\sim$145 km (Fig. 21). A recent study even suggested that there are about a quadrillion tons of diamonds in the Earth's interior.[254] A tiny part of these crystals is carried to the Earth's surface from the mantle as the

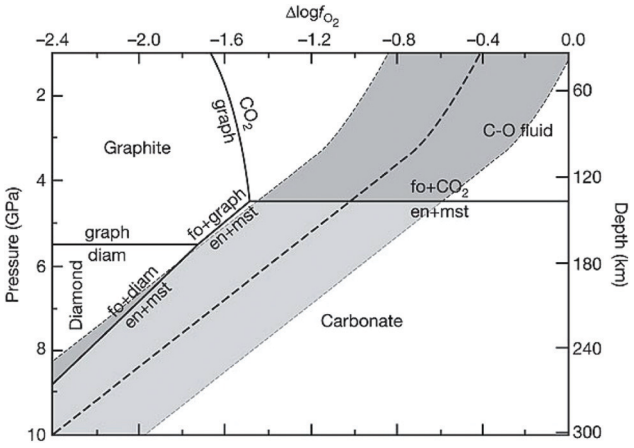

Fig. 21 Phase diagram of carbon under upper mantle conditions of pressure (and depth) *versus* the oxygen fugacity relative to the QFM buffer. The dashed line indicates the conditions with depth of a basaltic melt at a constant Fe^{3+}/Fe composition; fo: forsterite (olivine), en: enstatite (orthopyroxene), mst: magnesite, diam: diamond, graph: graphite. The various phase boundaries under melting conditions, and/or the magma ascent pathway are indicated. Duplicated from ref. 255 with permission of Springer Nature.

so-called xenocrysts – meaning ''foreign crystals'' – in volcanic rocks called kimberlites, lamproites and lamprophyre. These particular magmas not only form below 145 km to be able to collect diamond, but also rise to the surface fast enough to prevent the transformation of diamond to graphite – the thermodynamic allotrope at room pressure – or its dissolution in the molten rocks. Although only about 1% of these diamonds contain mineral inclusions such as olivines, orthopyroxenes, clinopyroxenes, garnets, spinels, sulphides or metal alloys, these inclusions play a key role in understanding and interpreting the thermobaric conditions of diamond formation, thus providing important insights into the geochemistry and mineralogy of the Earth's mantle. As a ''messenger'' from the Earth's interior, natural diamonds help Earth scientists to understand the evolution of our planet. For materials scientists, diamond is also crucial, given its exceptional properties.

Indeed, diamond is the hardest known material. It is chemically inert to most acids and alkali metals. It has remarkable high thermal and low electrical conductivities, and is optically transparent across a wide wavelength range, from the ultraviolet to the far infrared. These unique properties make diamond a material of choice for a variety of mechanical applications including abrasives, inserts and wear-resistant coatings for cutting tools, surgical blades, grinding and polishing tools and for a diverse range of optical technologies including sensors, sources, infrared windows, and light manipulators. Many other potential applications for diamond as an engineering material are possible. This has pushed scientists to no longer be satisfied with only natural diamonds but to produce them synthetically.

The effort to synthesize artificial diamond has been the driving force for the development of many innovative high pressure high temperature (HP–HT) technologies throughout

the 20th century. Thanks to these new technologies, especially the development of the ''Belt system'', diamond was produced in 1955 in thermodynamically stable regime (7.5 GPa and 2000 °C) from a carbon-rich melt.[256] Later, diamond synthesis in a metal flux (Fe, Co or Ni) was found to improve yields and enable scaling up to the industrial level. Nowadays, synthesis under extreme pressure and temperature conditions is the principal method of diamond synthesis in the industrial field with a world annual production of 3000 million carats (1 carat = 0.2 g).

From a fundamental point of view, the high-pressure technologies developed for the diamond industry led to the emergence in various academic laboratories of a vast exciting area of research where pressure opened up an additional dimension for the synthesis of new classes of dense stable or metastable compounds, whether they are crystalline, amorphous or even composite materials.

Recent advances in high-pressure materials synthesis are strongly linked to technological developments that only a few groups master. In order for the reader to catch a glimpse on the methods used to achieve the high pressures found deep inside the Earth, it appears necessary to first provide a quick survey of the most used high-pressure methods.

7.3. Main high-pressure methods for materials synthesis

High-pressure technologies can be divided into two main types of apparatuses: the diamond anvil cell (DAC) and large volume presses (LVP).

The DAC (Fig. 22) is a compact device composed of two opposed gem-quality diamond anvils, which can generate a wide range of pressures and temperatures. The scale starts from below 1 to over 600 GPa at maximum, therefore covering all the pressures of the planetary interior. For instance, the center of our planet is at 350 GPa. The high temperatures (up to 8000 K) can be achieved by additional laser (near IR or CO_2) heating or resistive heating. The pressure is measured by visible fluorescence of a known standard (usually ruby) and temperature is evaluated by measurements of the black body radiation of the sample. As diamonds are transparent over a wide range of wavelengths, the DAC can be coupled with visible light (for sample visualization and spectroscopic methods), infrared light (for heating), and most importantly X-rays and γ-rays (for probing the atomic, phononic, electronic and magnetic structures). Among the research trends using DAC, some of the hottest topics in materials science are the synthesis of room temperature superconducting materials (the current T_c record is 288 K, *i.e.*, the average surface temperature of the Earth, in a hydrogen-rich carbon material reported recently[257]) and the design of novel high energy density materials (for example LiN_5[258] or C–N–H compounds[259]). A natural field of research where DAC methods are broadly used is the science of planetary interiors as previously described in the case of the structure of our Earth. The physical and chemical properties of matter that builds essential parts of planetary mantles and cores can only be reached, captured and characterized at relevant high pressures and temperatures achievable with the DAC, particularly when bound to *in situ* synchrotron-based analytical methods,[260] but also with *ex situ* lab-scale experiments.[261] Nevertheless, the DAC has a major drawback for synthesis: the sample volume recovered is very small – in the order of 10^{-3} mm^3 for a pressure of 10 GPa and 10^{-5} mm^3 for 100 GPa –, which limits in depth physical and chemical characterization studies using in-house laboratory techniques. These small volumes also make the use of solvents much more difficult. Therefore further development of DAC devices is needed to link the principles of the protocols described in the previous sections. This is also why DAC synthesis is difficult to conceive for any industrial perspective and these research studies remain mainly of fundamental interest. A recent practical review on the DAC methods can be found in ref. 262.

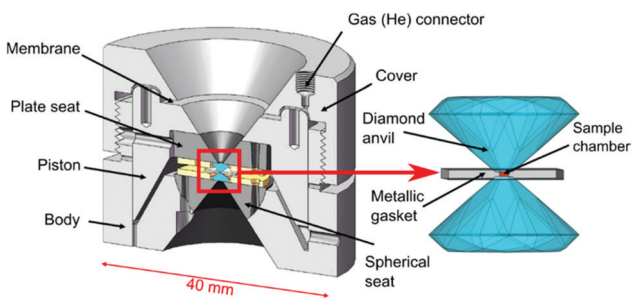

Fig. 22 Section view of a membrane diamond anvil cell.

This is not the case for large volume presses that are already widely used in industry. Large volume devices (more details can be found in various reviews[263,264]) are able to compress at least several cubic millimeter samples to pressures beyond 1 GPa. These devices use a hydraulic press following the principle of ''intensification'': a primary oil pressure is applied to the base of the piston of a press and the generated force is transmitted over a much smaller surface between the anvils, resulting in the intensification of the pressure obtained. Another important principle of LVPs is the ''hydrostaticity'' of the compression. Gaskets, prepared usually from materials with low coefficient of internal friction, fill the space between two or more hard anvils. They are crucial components ensuring the hydrostatic or quasi-hydrostatic compression since they deform in all directions, including the directions toward the sample, thereby transferring anvil pressure on the sample area. Also, these devices use resistive heating with an internal heater (graphite, chromite $LaCrO_3$, metallic foil, *etc.*) inside the gasket assembly to reach simultaneously high temperature and high pressure. Temperature measurements can be done using thermocouples, power–temperature calibration curves or internal calibrants (if coupled with *in situ* X-ray or neutron diffraction). The pressure generated in these large volume presses is reproducible, so for *ex situ* experiments, the pressure on the sample is determined by previous *in situ* established primary oil pressure calibrations, using a pressure sensor.

Large volume presses are therefore the instruments of choice for high pressure and high temperature synthesis studies (>1 GPa) because the recovered sample volumes allow all the

standard physical–chemical characterization studies of materials science. Among LVPs, three devices are widely used in academic geo- and materials sciences laboratories: the multi-anvil device, the Paris-Edinburgh press and the piston cylinder apparatus. Conditions commonly achieved with these three devices range from below 1 to 25 GPa and up to 2500 K.

The multi-anvil press has a double anvil stage arrangement: primary and secondary anvils. Basically, the outer six steel anvils are called primary anvils, driven by uniaxial compression of the press' piston. These six anvils form a cubic cavity where eight cubes (in tungsten carbide WC, cubic boron nitride c-BN or sintered diamond) can be installed as secondary anvils. The latter have truncated interior corners (Fig. 23 and 24). These truncations form an octahedral high-pressure assembly cavity where usually a Cr-doped MgO octahedron is placed. The sample assembly is installed inside this octahedron. Evidently, smaller truncations (hence a smaller octahedron) result in higher attainable pressures. There are mainly two different geometries in multi-anvil presses: the DIA geometry and the Walker one. They differ in the orientation of the cubic cavity (secondary anvils) for the compression axis, *i.e.*, the [111] direction of the cube in the Walker module (Fig. 23B), and the [100] in the DIA one (Fig. 23C). The major drawback of these multi-anvil presses, however, remains their mass (several tons) and their footprint, which prohibits any rapid installation on a conventional synchrotron diffraction station. Thus, in general, these devices are either fixed in laboratories for *ex situ* studies (where the product of the synthesis is analyzed *post mortem* under ambient conditions), or permanently installed at X-ray diffraction beamlines under synchrotron radiation, which are therefore only or largely dedicated to HP-HT measurements (*e.g.* beamline ID06 at ESRF where the 2000 tons force multi-anvil press weighs more than 6 tons (Fig. 23A).

On the contrary, the second popular large volume press is the Paris–Edinburgh press, which has reasonable dimensions and weight ($\sim 25 \times 25 \times 25$ cm^3 and 50 kg in its standard design). Initially designed for high pressure neutron diffraction studies,[265] the Paris–Edinburgh press has been adapted later for a wide range of *in situ* high (P,T) measurements as for example neutron[266] and X-ray diffraction.[267] This device is also widely used for *ex situ* synthesis in many academic laboratories with the standard "2 opposed anvils" geometry where the anvils have a special conical high-pressure cavity dedicated to the gasket and sample assembly, or with a miniaturized multi-anvil module following the Walker geometry explained above.[268] Both configurations are shown in Fig. 24, which displays on the same drawing the "2 opposed anvils" module and the "multi-anvil" Walker module.

The last-mentioned device is the piston-cylinder apparatus.[269] Similar to previously mentioned devices, it achieves high pressures using the principle of pressure amplification: converting a small load on a large piston to a relatively large load on a small piston. The uniaxial pressure is then distributed quasi-hydrostatically over the sample through deformation of the assembly materials. Sample are typically 200 mm^3 and $\sim$500 mg. Larger assemblies can reach 750 mm^3. Due to its simplicity and applicability to pressures up to 5 GPa and temperatures up to 1750 °C, the piston-cylinder apparatus has been the major experimental tool in early studies of metamorphic petrology, hydrothermal systems. It still allows more detailed studies of crustal and upper mantle lithologies and their mineral formation processes.[270]

Over the last few years, intensive efforts have been dedicated to the adaptation of large volume presses to *in situ* synchrotron X-ray diffraction for direct observation of synthesis pathways towards both stable and metastable materials under HP–HT. In these apparatuses, the samples are often surrounded by complicated opaque environments, like gaskets, anvils, *etc.* This is why innovative Soller slits system[271] and combined angle- and energy-dispersive structural analysis and refinement system (CAESAR[272]) were developed to observe only the X-ray diffraction pattern of the chemical precursors and even, by using angular X-ray diffraction (ADX), to allow Rietveld refinement of the crystal structure of solids synthesized under extreme conditions. As an illustration, Fig. 25 shows the integration of the miniaturized multi-anvil Paris–Edinburgh press, – whose operating principle has been detailed in Fig. 24 – on the ID27 beamline of ESRF. These advances made it possible to

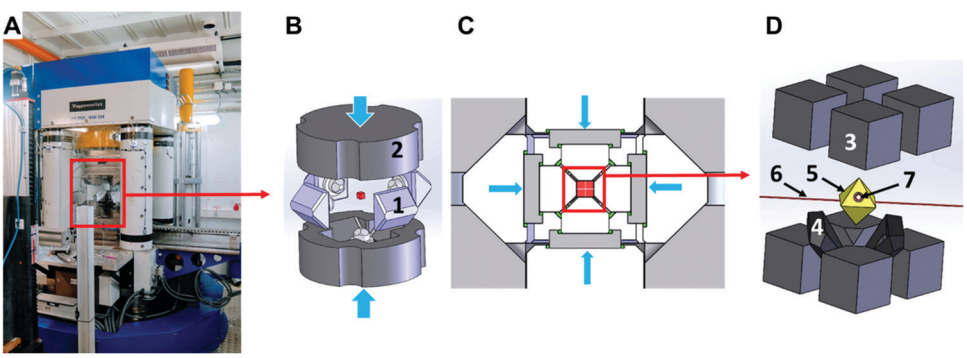

Fig. 23 (A) The multi-anvil press installed at ID06, ESRF. (B) Concept design of the multi-anvil press. (1) Steel primary anvils. (2) Secondary anvils made by eight truncated cubes. (C) Schematic view of the DIA geometry, in which the compression of the primary anvils takes place along the [001] directions of cubic assemblage of secondary cubic anvils. (D) Zoom of the secondary anvil stage. (3) Truncated cubes. (4) Gaskets. (5) Octahedral pressure medium. (6) Thermocouple. (7) Sample chamber.

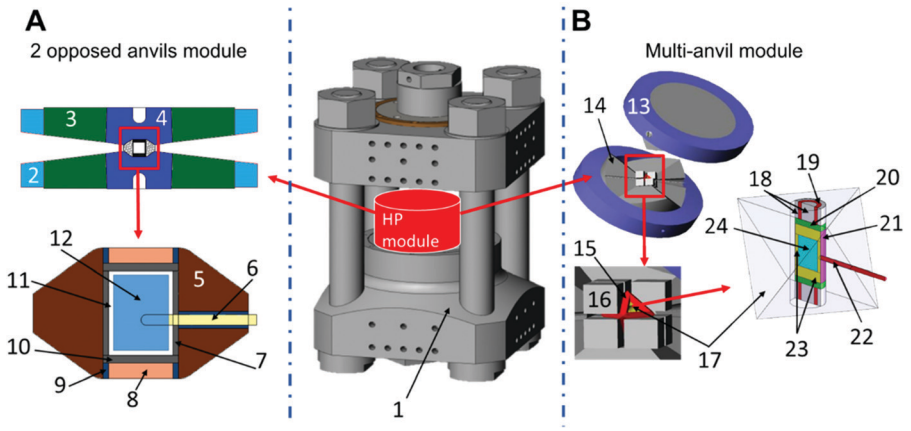

Fig. 24 Schematic diagram of the large volume Paris–Edinburgh press and details of its (A) 2 opposed anvils module and (B) multi-anvil module with Walker geometry. (1) V7 Paris–Edinburgh press. (2) Cooling device. (3) Steel binding ring. (4) Tungsten carbide WC anvils. (5) Amorphous boron epoxy gasket. (6) Coaxial thermocouple. (7) Graphite heater. (8) Insulating ceramic. (9) Electrical contacts. (10) Molybdenum disk. (11) h-BN or MgO capsule. (12) Sample. (13) Containment ring. (14) First-stage anvils. (15) Pyrophyllite gasket. (16) Second-stage anvils (WC cubes). (17) Cr-doped MgO octahedron. (18) Insulating ceramic. (19) Electrical contact. (20) Molybdenum disk. (21) Furnace (graphite, Rhenium foil or $LaCrO_3$). (22) Thermocouple. (23) Sample capsule (usually MgO or h-BN). (24) Sample.

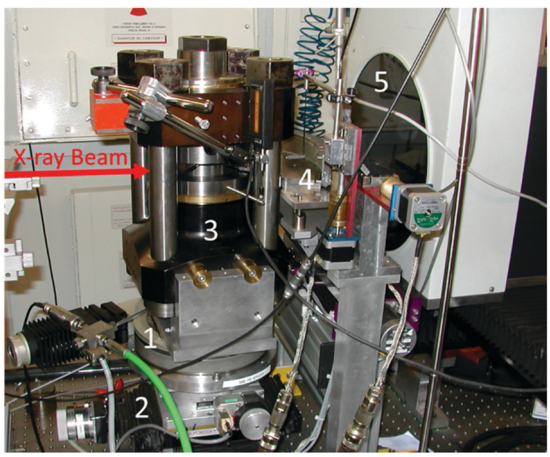

Fig. 25 Large volume Paris–Edinburgh press on the ID27 beamline of ESRF for *in situ* angular X-ray diffraction experiments: (1) Rotation motor. (2) Micrometric motors *x*, *y* and *z*. (3) Paris–Edinburgh press. (4) Soller slits. (5) CCD detector.

overcome the inherent limitations of the usual *ex situ* 'cook and look' strategy, which is a time-consuming synthesis approach. The opportunity to observe *in situ* and in real time the structural evolution of the reactants, the chemical reactions and the possible intermediate phases under extreme conditions is essential. It allows tackling these syntheses in all their complexities and establishing the – or minimizing the range of – (P,T) conditions required to synthesize a given material. It also enables better understanding of the mechanisms and the kinetics of the transformations under these extreme conditions.

7.4. Relevance of high-pressure synthesis for the synthesis of new materials

Large volume high-pressure synthesis can lead to the formation of new materials with new properties, which are very difficult to synthesize under conventional thermodynamic conditions. The present paper is not intended as a comprehensive review of the field (partial reviews already exist[273–275]), but rather to highlight the diversity of new inorganic compounds and materials recently synthesized at high pressures. These materials can have useful mechanical, superconductive, energetic, magnetic, electronic, optical or thermoelectric properties, with great values for potential technological applications. For illustration and understanding of the connection between the geological field and the chemical field, Fig. 26 displays the (P,T) conditions of the synthesis of some remarkable compounds mentioned above, in relation to the average geothermal gradient.

As a first example of hot topic, intensive research is focused on the discovery of new superhard materials by synthesizing new compounds, with a stronger performance than diamond for applications, including higher thermal and chemical stabilities.[273] The B–C–N–O system is a natural choice for such an exploration, as it encompasses many diamond-like and boron-rich compounds formed by three-dimensional networks of strong covalent bonds, responsible for high hardness. In the last few years, it has been possible to synthesize under high pressure new superhard materials (*i.e.*, materials with Vickers microhardness exceeding 40 GPa) like γ-boron[276] and c-BC_5[277] (Fig. 27). Importantly, some entanglement with the field of nanomaterials chemistry and physics has started to emerge, as evidenced by pressure-induced nanostructuration of diamond[278,279] and cubic boron nitride[280,281] (Fig. 27). By virtue of the Hall–Petch effect,[282,283] the decrease in grain size down to dozens of nm results in substantial increase in hardness compared to polycrystalline microstructured materials. These developments have led to extremely hard bulk nanostructured materials.

The search for new superconducting materials is rather the field of very high pressures achieved by DAC technology. Nonetheless and as a second hot topic, several new compounds with

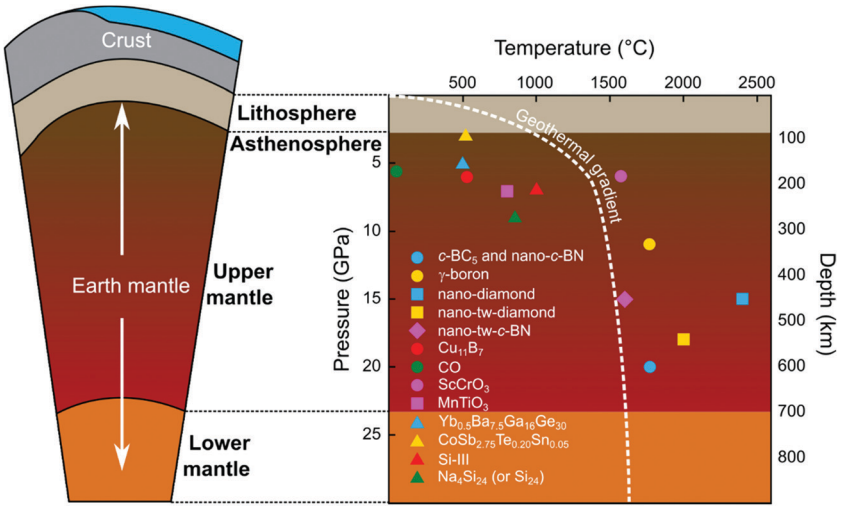

Fig. 26 Pressure and temperature domains of Earth's upper mantle, accessible by large volume devices discussed in the text for high-pressure synthesis. Dashed line: the Earth's mean geotherm; the other symbols indicate typical (*P*,*T*) conditions where new materials can be synthesized. The corresponding references are given in the text.

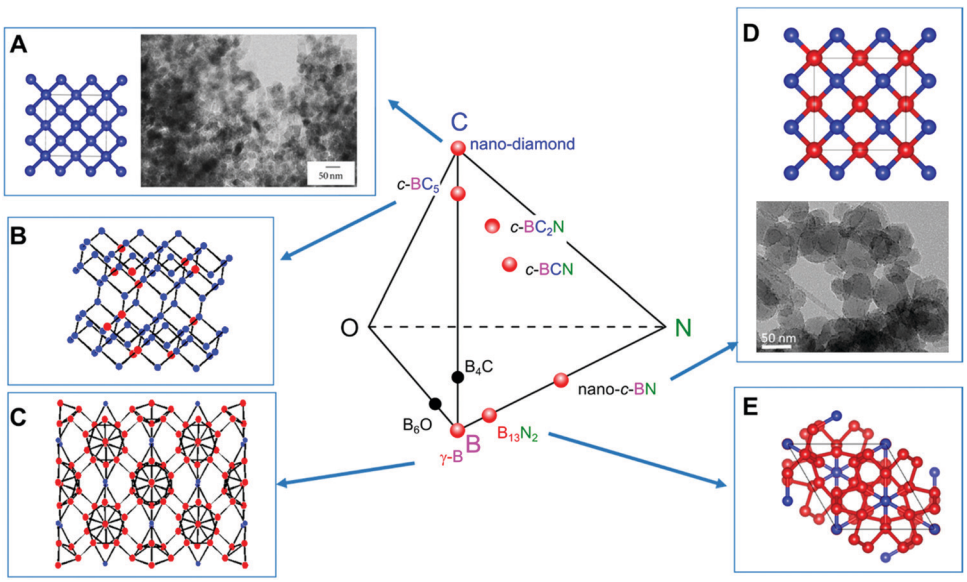

Fig. 27 Crystal structures of some superhard phases in the B–C–N–O quaternary system and TEM image of superhard bulk nanostructured materials. Phases discovered in the last two decades are shown with red spots. (A) Structure and TEM image of nano-diamond sample synthesised at 22 GPa and 1400 °C. Reproduced from ref. 284 with permission. (B) Structure of cubic BC_5 (synthesised at 20 GPa and 2200 K) with boron atoms that are randomly distributed throughout the diamond-like lattice. (C) Crystal structure of γ-B synthesised at 12 GPa and 2000 K. Two oppositely charged sublattices are marked by different colors. (D) Structure and TEM image of nano-cBN synthesised at 20 GPa and 1770 K. (E) Structure of $B_{13}N_2$ synthesised at 5.3 GPa and 2600 K. Boron, carbon and nitrogen atoms are in purple, blue and green colors. In (C), boron atoms belonging to the cationic and anionic networks are light and dark purple, respectively.

interesting critical transition temperatures T_c have recently been obtained in large quantities at moderate pressures (<10 GPa), thus among which a new chlorine compound $Sr_{3-x}Ca_xCu_2O_{4+\delta}Cl_{2-y}$,[285] $Cu_{11}Bi_7$,[286] a series of new iron (nickel)-based compounds[287] and $ReFeAsO_{1-x}H_x$.[288]

The third topic deals with the large volume high-pressure synthesis of high energy density materials. In particular, a new polymerized compound encompassing CO groups connected with single bonds has received significant attention.[289] This material, recoverable under ambient conditions, is a promising material for energy storage, since it has exceptionally high energy "available" in a low mass. Among the potential fields of application, the aerospace domain would strongly benefit from this material.

Under high pressure, it is also possible to synthesize new multiferroic materials such as $BiMnO_3$, $BiAlO_3$, $BiGaO_3$, $BiFeO_3$,[275] and new interesting phases in oxides like $MnMO_3$ (M = Ti, Sn)),[290] $ScCrO_3$ and $InCrO_3$.[291]

In the field of photonics and photovoltaics, the recent high-pressure synthesis of silicon Si-III has been performed at pressure as low as 7 GPa in the Na–Si system.[292] Optical measurements have shown that Si-III is not a semimetal, unlike what previous reports had claimed, but a direct narrow-bandgap semiconductor with a plasma wavelength near 11 μm, suggesting potential for infrared plasmonic applications.[293] Likewise, recent high-pressure studies on phase transformations in the Na–Si system[294] revealed a number of interesting routes to new and identified silicon compounds: Na_4Si_4 and intermetallic clathrates Na_8Si_{46}, $Na_{24}Si_{136}$ and Na_4Si_{24}. In particular, sodium evaporation from Na_4Si_{24} by moderate heating (100 °C) in vacuum leads to a new allotrope of silicon, orthorhombic *o*-Si_{24}, with a zeolite structure.[295] The variety of the properties associated with this new phase (*e.g.* quasi-direct bandgap of ~1.3 eV) make it promising for future optoelectronics applications, including solar energy conversion.

Finally, high-pressure synthesis has also a significant advantage to produce new heavily doped semiconductors, which are excellent thermoelectric materials. For example, two compounds synthesized under extreme conditions, $Yb_{0.5}Ba_{7.5}Ga_{16}Ge_{30}$ and $CoSb_{2.75}Te_{0.20}Sn_{0.05}$, have remarkable figures of merit *ZT* of *ca.* 1.[296,297]

This brief illustration of new compounds that cannot be formed with traditional liquid-phase and solid-state chemistries demonstrates that high-pressure synthesis has become a viable and promising method to design new functional materials. In the near future, next generation targets will concern classes of emergent complex materials, including the control of interfaces of the nanoscale. For instance, the unusual combination of high temperature solution synthesis of metal boride nanocrystals in molten salts with subsequent thermobaric treatments was used recently to create new nanocomposites of ternary borates.[298] These phases contain nano-inclusions of metal borides separated from each other by a few nanometers in an also-nanostructered borate matrix. This study validates a new approach linking synthesis of inorganic nanomaterials and high-pressure synthesis to yield nanocomposites made of exceptional phases not reachable under ambient conditions. This approach paves the way to advanced nanocomposite materials which could combine the best properties of each component and will inspire the design of a new class of multifunctional materials with advanced mechanical, electronic, magnetic, optical, thermal and thermoelectric properties for a wide range of applications.

8. Conclusions and perspectives

In this review, we have stressed how the state-of-the-art materials syntheses are paralleled by geological phenomena and how these syntheses techniques can be considered as being inspired from geology. Such synthesis methods have been known for centuries, such as aqueous precipitation, which is undergoing a renewal, thanks to calculation and data mining,[299] as described in the related section of this review. Other synthesis approaches have only emerged over the last few years (*e.g.* application of thermal shocks and of molten salt syntheses to nanomaterials). In all cases, their current and future development should benefit from strengthening the link between materials synthesis and geosciences. For instance, geology offers more complex and diverse physicochemical conditions than only those sketched in this review.[300] The analysis methods used by geologists may also be useful for the materials chemist, especially for the development of *in situ* studies at high temperatures.[301] Besides materials and nanomaterials synthesis, one may also wonder if geology could also deliver conditions to tune or exacerbate materials properties. For instance, some geological conditions are a nice playground to develop original catalysts and catalysis conditions, materials recycling[86,302,303] and could as well be scrutinized as energy conversion devices.[304]

The synthesis conditions developed in this review and more widely in the frame of geoinspiration are in most cases exempt of organic solvents and of ligands, traditionally used in colloidal synthesis of nano-objects. Therefore, scrutinizing geological phenomena in the context of materials synthesis appears as a virtuous approach towards enhanced sustainability of chemical synthesis. This last point is obviously of high importance given the challenges that we are currently facing.

Last but not least, it is possible to foresee a feedback loop, where geoinspired synthesis could also provide new insights into geological processes and rock formation, as pointed out by Hochela[305,306] and more recently by Genova *et al.*[155] Likewise, analytical tools of materials chemists may be of interest for geologists. Overall, this review shows how straightforward the connections between both fields can be made and how cross-fertilization could enrich materials synthesis and geosciences, together.

Conflicts of interest

There are no conflicts to declare.

Acknowledgements

This work has been supported by the European Research Council (ERC) Consolidator Grant GENESIS under the European Union's Horizon 2020 research and innovation program (grant agreement no 864850).

References

1 C. Sanchez, H. Arribart, M. Madeleine and G. Guille, *Biomimetism and bioinspiration as tools for the design of innovative materials and systems*, 2005.
2 M. M. Unterlass, *Biomimetics*, 2017, **2**, 8.
3 H. M. Moura and M. M. Unterlass, *Biomimetics*, 2020, **5**, 29.
4 A. E. Phillips, *Philos. Trans. R. Soc., A*, 2019, **377**, 20190153.
5 D. Portehault, S. Delacroix, G. Gouget, R. Grosjean and T.-H.-C. Chan-Chang, *Acc. Chem. Res.*, 2018, **51**, 930–939.
6 S. K. Gupta and Y. Mao, *J. Phys. Chem. C*, 2021, **125**, 6508–6533.

7 V. Garnier, G. Giuliani, D. Ohnenstetter, A. E. Fallick, J. Dubessy, D. Banks, H. Q. Vinh, T. Lhomme, H. Maluski, A. Pêcher, K. A. Bakhsh, P. van Long, P. T. Trinh and D. Schwarz, *Ore Geol. Rev.*, 2008, **34**, 169–191.

8 G. Giuliani, J. Dubessy, D. Ohnenstetter, D. Banks, Y. Branquet, J. Feneyrol, A. E. Fallick and J. E. Martelat, *Miner. Deposita*, 2018, **53**, 1.

9 **https://openpress.usask.ca/physicalgeology/chapter/3-1-earths-layers-crust-mantle-and-core-2/**.

10 **https://www.blendswap.com/blends/view/46815**.

11 K. Hirose, B. Wood and L. Vočadlo, *Nat. Rev. Earth Environ.*, 2021, **2**, 645–658.

12 R. G. Trønnes, M. A. Baron, K. R. Eigenmann, M. G. Guren, B. H. Heyn, A. Løken and C. E. Mohn, *Tectonophysics*, 2019, **760**, 165–198.

13 B. R. Frost, *Oxide Minerals: Petrologic and Magnetic Significance*, De Gruyter, 1991, pp. 1–10.

14 J. J. Papike, J. M. Karner and C. K. Shearer, *Am. Mineral.*, 2005, **90**, 277–290.

15 C. K. Shearer, J. J. Papike and J. M. Karner, *Am. Mineral.*, 2006, **91**, 1565–1573.

16 B. W.-D. Yardley and R. J. Bodnar, *Geochemical Perspectives*, 2014, **3**, I-127.

17 E. G. Jones and C. H. Lineweaver, *Astrobiology*, 2010, **10**, 349–361.

18 S. Marshak, *Earth Portrait of a Planet*, Norton & Company, New York, 2012.

19 D. E. White, *Bull. Geol. Soc. Am.*, 1957, **68**, 1637–1658.

20 C. Bolm, R. Mocci, C. Schumacher, M. Turberg, F. Puccetti and J. G. Hernández, *Angew. Chem., Int. Ed.*, 2018, **57**, 2423–2426.

21 I. Huskić and T. Friščić, *Philos. Trans. R. Soc., A*, 2019, **377**(2149), 20180221.

22 J.-P. Jolivet, *Metal Oxide Chemistry and Synthesis: From Solution to Solid State*, Wiley, Chichester, 2000.

23 M. Yoshimura and K. Byrappa, *J. Mater. Sci.*, 2008, **43**, 2085–2103.

24 G. Demazeau, *J. Mater. Chem.*, 1999, **9**, 15–18.

25 G. Demazeau, *J. Mater. Sci.*, 2008, **43**, 2104–2114.

26 T. Adschiri, Y. Hakuta and K. Arai, *Ind. Eng. Chem. Res.*, 2000, **39**, 4901–4907.

27 K. F.-E. Schafthaul, *Gelehrte Anzeigen Bayer Akal*, 1845, 557–593.

28 R. M. Barrer, *J. Chem. Soc.*, 1948, 2158–2163.

29 G. W. Morey and P. Niggli, *J. Am. Chem. Soc.*, 1913, **35**, 1086–1130.

30 D. Zhang, C.-H. Zhou, C.-X. Lin, D.-S. Tong and W.-H. Yu, *Appl. Clay Sci.*, 2010, **50**, 1–11.

31 S. Zhu, S. H. Ho, C. Jin, X. Duan and S. Wang, *Environ. Sci.: Nano*, 2020, **7**, 368–396.

32 C. Sun, Y. Zhang, S. Song and D. Xue, *J. Appl. Crystallogr.*, 2013, **46**, 1128–1135.

33 R. Yang, Y. Fan, R. Ye, Y. Tang, X. Cao, Z. Yin and Z. Zeng, *Adv. Mater.*, 2021, **33**, 2004862.

34 Q. Feng, H. Kanoh and K. Ooi, *J. Mater. Chem.*, 1999, **9**, 319–333.

35 B. Chen, B. Wu, L. Yu, M. Crocker and C. Shi, *ACS Catal.*, 2020, **10**, 6176–6187.

36 X. Xie, C. Zhang, M. B. Wu, Y. Tao, W. Lv and Q. H. Yang, *Chem. Commun.*, 2013, **49**, 11092–11094.

37 X. Bai, X. Tong, Y. Gao, W. Zhu, C. Fu, J. Ma, T. Tan, C. Wang, Y. Luo and H. Sun, *Electrochim. Acta*, 2018, **281**, 525–533.

38 T. T. Truong, Y. Liu, Y. Ren, L. Trahey and Y. Sun, *ACS Nano*, 2012, **6**, 8067–8077.

39 J. Shan, Y. Zhu, S. Zhang, T. Zhu, S. Rouvimov and F. Tao, *J. Phys. Chem. C*, 2013, **117**, 8329–8335.

40 W. Zhang, Z. Yang, X. Wang, Y. Zhang, X. Wen and S. Yang, *Catal. Commun.*, 2006, **7**, 408–412.

41 W. Zhang, H. Wang, Z. Yang and F. Wang, *Colloids Surf., A*, 2007, **304**, 60–66.

42 S. Liang, F. Teng, G. Bulgan, R. Zong and Y. Zhu, *J. Phys. Chem. C*, 2008, **112**, 5307–5315.

43 W. Yang, Y. Zhu, F. You, L. Yan, Y. Ma, C. Lu, P. Gao, Q. Hao and W. Li, *Appl. Catal., B: Environ.*, 2018, **233**, 184–193.

44 F. Wang, H. Dai, J. Deng, G. Bai, K. Ji and Y. Liu, *Environ. Sci. Technol.*, 2012, **46**, 4034–4041.

45 B. R. Chen, W. Sun, D. A. Kitchaev, J. S. Mangum, V. Thampy, L. M. Garten, D. S. Ginley, B. P. Gorman, K. H. Stone, G. Ceder, M. F. Toney and L. T. Schelhas, *Nat. Commun.*, 2018, **9**, 2553.

46 S. Ching, J. P. Franklin and C. M. Spencer, *Polyhedron*, 2013, **58**, 53–59.

47 N. Kijima, H. Yasuda, T. Sato and Y. Yoshimura, *J. Solid State Chem.*, 2001, **159**, 94–102.

48 H. Peng, H. Fan, J. Sui, C. Wang, W. Zhang and W. Wang, *ChemistrySelect*, 2020, **5**, 869–874.

49 X. Wu, F. Yang, H. Dong, J. Sui, Q. Zhang, J. Yu, Q. Zhang and L. Dong, *J. Electroanal. Chem.*, 2019, **848**, 113332.

50 D. Gangwar and C. Rath, *Appl. Surf. Sci.*, 2021, **557**, 149693.

51 L. K. Mcleod, G. H. Spikes, R. J. Kashtiban, M. Walker, A. V. Chadwick, J. D.-B. Sharman and R. I. Walton, *Dalton Trans.*, 2020, **49**, 2661–2670.

52 D. Portehault, S. Cassaignon, E. Baudrin and J.-P. Jolivet, *J. Mater. Chem.*, 2009, **19**, 2407.

53 B.-R. Chen, W. Sun, D. A. Kitchaev, J. S. Mangum, V. Thampy, L. M. Garten, D. S. Ginley, B. P. Gorman, K. H. Stone, G. Ceder, M. F. Toney and L. T. Schelhas, *Nat. Commun.*, 2018, **9**, 2553.

54 D. A. Kitchaev, S. T. Dacek, W. Sun and G. Ceder, *J. Am. Chem. Soc.*, 2017, **139**, 2672–2681.

55 A. Navrotsky, *Proc. Natl. Acad. Sci. U. S. A.*, 2004, **101**, 12096–12101.

56 A. Navrotsky, *J. Chem. Thermodyn.*, 2007, **39**, 1–9.

57 E. Tronc, C. Chanéac and J. P. Jolivet, *J. Solid State Chem.*, 1998, **139**, 93–104.

58 S.-I. Ohkoshi, Y. Tsunobuchi, T. Matsuda, K. Hashimoto, A. Namai, F. Hakoe and H. Tokoro, *Nat. Chem.*, 2010, **2**, 539–545.

59 W. Sun, D. A. Kitchaev, D. Kramer and G. Ceder, *Nat. Commun.*, 2019, **10**, 573.

60 W. Ostwald, *Zeitschrift für Physikalische Chemie*, 1897, **22U**, 289–330.
61 S. Y. Chung, Y. M. Kim, J. G. Kim and Y. J. Kim, *Nat. Phys. 2009 5:1*, 2008, **5**, 68–73.
62 X. Huang, D. Lv, H. Yue, A. Attia and Y. Yang, *Nanotechnology*, 2008, **19**, 225606.
63 B. R. Chen, W. Sun, D. A. Kitchaev, K. H. Stone, R. C. Davis, G. Ceder, L. T. Schelhas and M. F. Toney, *J. Mater. Chem. A*, 2021, **9**, 7857–7867.
64 W. Sun and G. Ceder, *CrystEngComm*, 2017, **19**, 4576–4585.
65 Q. Feng, K. Yanagisawa and N. Yamasaki, *J. Porous Mater.*, 1998, **5**(2), 153–162.
66 Q. Feng, H. Kanoh, Y. Miyai and K. Ooi, *Chem. Mater.*, 2002, **7**, 1722–1727.
67 A. Putnis, *Mineral. Mag.*, 2002, **66**, 689–708.
68 J. F. Banfield, W. W. Barker, S. A. Welch and A. Taunton, *Proc. Natl. Acad. Sci. U. S. A.*, 1999, **96**, 3404–3411.
69 J. Brugger, A. McFadden, C. E. Lenehan, B. Etschmann, F. Xia, J. Zhao and A. Pring, *Chimia*, 2010, **64**, 693–698.
70 R. Andris, P. Ridley, B. W. Byles, D. A. Cullen, K. L. More and E. Pomerantseva, *Script. Mater.*, 2021, **195**, 113713.
71 I. Gómez-Recio, A. Azor-Lafarga, M. L. Ruiz-González, M. Hernando, M. Parras, J. J. Calvino, M. T. Fernández-Díaz, D. Portehault, C. Sanchez and J. M. González-Calbet, *Chem. Commun.*, 2020, **56**, 4812–4815.
72 I. Gómez-Recio, H. Pan, A. Azor-Lafarga, M. L. Ruiz-González, M. Hernando, M. Parras, M. T. Fernández-Díaz, J. J. Delgado, X. Chen, D. G. Jiménez, D. Portehault, C. Sanchez, M. Cabero, A. Martínez-Arias, J. M. González-Calbet and J. J. Calvino, *ACS Catal.*, 2021, 15026–15039.
73 Y. Kim, Y. Hong, M. G. Kim and J. Cho, *Electrochem. Commun.*, 2007, **9**, 1041–1046.
74 X. Zhang, Y. Yang, Q. Zhu, M. Ma, Z. Jiang, X. Liao and C. He, *J. Colloid Interface Sci.*, 2021, **598**, 324–338.
75 A. Azor, I. Gomez-Recio, L. Ruiz-Gonzalez, M. Parras and J. M. Gonzalez-Calbet, *J. Chem. Sci. Eng.*, 2019, **2**, 61–69.
76 A. Navrotsky, C. Ma, K. Lilova and N. Birkner, *Science*, 2010, **330**, 199–201.
77 L.-F. Huang, J. R. Scully and J. M. Rondinelli, *Ann. Rev. Mater. Res.*, 2019, **7**, 44.
78 A. M. Patel, J. K. Nørskov, K. A. Persson and J. H. Montoya, *Phys. Chem. Chem. Phys.*, 2019, **21**, 25323–25327.
79 L. N. Walters, C. Zhang, V. P. Dravid, K. R. Poeppelmeier and J. M. Rondinelli, *Chem. Mater.*, 2021, **33**, 2726–2741.
80 A. P. Webber, S. Roberts, B. J. Murton and M. R.-S. Hodgkinson, *Geochem., Geophys., Geosyst.*, 2015, **16**, 2661–2678.
81 M. Claverie, M. Diez-Garcia, F. Martin and C. Aymonier, *Chem. – Eur. J.*, 2019, **25**, 5814–5823.
82 C. Aymonier, G. Philippot, A. Erriguible and S. Marre, *J. Supercrit. Fluids*, 2018, **134**, 184–196.
83 A. Loppinet-Serani, C. Aymonier and F. Cansell, *J. Chem. Technol. Biotechnol.*, 2010, **85**, 583–589.
84 E. W. Lemmon, M. O. McLinden and D. G. Friend, *Thermophysical Properties of Fluid Systems in the NIST Chemistry WebBook*, National Institute of Standards and Technology, Gaithersburg MD, 1998.
85 T. Voisin, A. Erriguible, D. Ballenghien, D. Mateos, A. Kunegel, F. Cansell and C. Aymonier, *J. Supercrit. Fluids*, 2017, **120**, 18–31.
86 E. Duverger-Nédellec, T. Voisin, A. Erriguible and C. Aymonier, *J. Supercrit. Fluids*, 2020, **165**, 104977.
87 L. Henry, N. Biscay, C. Huguet, S. Loison and C. Aymonier, *Green Chem.*, 2020, **22**, 8308–8315.
88 M. Carrier, A. Loppinet-Serani, C. Absalon, C. Aymonier and M. Mench, *Biomass Bioenergy*, 2012, **43**, 65–71.
89 T. Adschiri, K. Kanazawa and K. Arai, *J. Am. Ceram. Soc.*, 1992, **75**, 2615–2618.
90 J. A. Darr, J. Zhang, N. M. Makwana and X. Weng, *Chem. Rev.*, 2017, **117**, 11125–11238.
91 C. Aymonier, A. Loppinet-Serani, H. Reverón, Y. Garrabos and F. Cansell, *J. Supercrit. Fluids*, 2006, **38**, 242–251.
92 E. Lester, P. Blood, J. Denyer, D. Giddings, B. Azzopardi and M. Poliakoff, *J. Supercrit. Fluids*, 2006, **37**, 209–214.
93 C. Slostowski, S. Marre, O. Babot, T. Toupance and C. Aymonier, *Langmuir*, 2012, **28**, 16656–16663.
94 C. Slostowski, S. Marre, O. Babot, T. Toupance and C. Aymonier, *Langmuir*, 2014, **30**, 5965–5972.
95 O. Pascu, S. Marre, B. Cacciuttolo, G. Ali, L. Hecquet, M. Pucheault, V. Prevot and C. Aymonier, *ChemNanoMat*, 2017, **3**, 614–619.
96 G. Philippot, K. M.-Ø. Jensen, M. Christensen, C. Elissalde, M. Maglione, B. B. Iversen and C. Aymonier, *J. Supercrit. Fluids*, 2014, **87**, 111–117.
97 T. Voisin, A. Erriguible, G. Philippot, D. Ballenghien, D. Mateos, F. Cansell, B. B. Iversen and C. Aymonier, *Chem. Eng. Sci.*, 2017, **174**, 268–276.
98 T. Voisin, A. Erriguible, G. Aubert and C. Aymonier, *Ind. Eng. Chem. Res.*, 2018, **57**, 2376–2384.
99 S. W. Bailey, *Clays Clay Mineral.*, 1969, **17**, 355–371.
100 G. M. Friedman, *Nature*, 1965, **207**, 283–284.
101 P. Boulvais, P. de Parseval, A. D'Hulst and P. Paris, *Mineral. Petrol.*, 2006, **88**, 499–526.
102 S. D. Parseval Polvé and D. Saint Blanquat, *Terra Nova*, 1999, **11**, 30–37.
103 M. Claverie, A. Dumas, C. Carême, M. Poirier, C. Le Roux, P. Micoud, F. Martin and C. Aymonier, *Chem. – Eur. J.*, 2018, **24**, 519–542.
104 A. Decarreau, H. Mondésir and G. Besson, *C. R. Acad. Sci., Ser. II: Mec., Phys., Chim., Sci. Terre Univers*, 1989, **308**, 301–306.
105 A. Dumas, F. Martin, E. Ferrage, P. Micoud, C. le Roux and S. Petit, *Appl. Clay Sci.*, 2013, **85**, 8–18.
106 F. Martin, C. Aymonier, S. Einloft, C. Carême, M. Poirier, M. Claverie, M. A. Prado, G. Dias, C. Quilfen, G. Aubert, P. Micoud, C. le Roux, S. Salvi, A. Dumas and S. Féry-Forgues, *J. Geochem. Explor.*, 2019, **200**, 27–36.
107 A. Dumas, M. Claverie, C. Slostowski, G. Aubert, C. Careme, C. Le Roux, P. Micoud, F. Martin and C. Aymonier, *Angew. Chem., Int. Ed.*, 2016, **128**, 10022–10025.
108 M. Claverie, Université de Bordeaux, 2018.
109 A. Dumas, M. Claverie, C. Slostowski, G. Aubert, C. Careme, C. Le Roux, P. Micoud, F. Martin and C. Aymonier, *Angew. Chem.*, 2016, **128**, 10022–10025.

110 A. Dumas, M. Mizrahi, F. Martin and F. G. Requejo, *Cryst. Growth Des.*, 2015, **15**, 5451–5463.
111 M. Claverie, F. Martin, C. Careme, C. le Roux, P. Micoud, O. Grauby and C. Aymonier, *Clay Miner.*, 2018, **53**, 497–503.
112 S. Fitzgerald, E. Harty, T. K. Joshi and A. L. Frank, *Am. J. Ind. Med.*, 2019, **62**, 385–392.
113 R. Zazenski, W. H. Ashton, D. Briggs, M. Chudkowski, J. W. Kelse, L. Maceachern, E. F. Mccarthy, M. A. Nordhauser, M. T. Roddy, N. M. Teetsel, A. B. Wells and S. D. Gettings, *Regul. Toxicol. Pharmacol.*, 1995, **21**, 218–229.
114 M. Yousfi, S. Livi, A. Dumas, C. le Roux, J. Crépin-Leblond, M. Greenhill-Hooper and J. Duchet-Rumeau, *J. Colloid Interface Sci.*, 2013, **403**, 29–42.
115 M. Yousfi, S. Livi, A. Dumas, J. Crépin-Leblond, M. Greenhill-Hooper and J. Duchet-Rumeau, *RSC Adv.*, 2015, **5**, 46197–46205.
116 M. Yousfi, S. Livi, A. Dumas, J. Crépin-Leblond, M. Greenhill-Hooper and J. Duchet-Rumeau, *J. Appl. Polym. Sci.*, 2014, **131**, 40453.
117 M. Hosseinpour, S. J. Ahmadi, A. Charkhi and S. A. Allahyari, *J. Supercrit. Fluids*, 2014, **95**, 236–242.
118 H. Harder, *Clay Miner.*, 1977, **12**, 281–288.
119 P. Andrieux and S. Petit, *Appl. Clay Sci.*, 2010, **48**, 5–17.
120 X. Li and J. Chang, *J. Mater. Sci.*, 2006, **41**, 4944–4947.
121 G. Wei, Y. Liu, X. Zhang, F. Yu and X. Du, *Int. J. Heat Mass Trans.*, 2011, **54**, 2355–2366.
122 N. M.-P. Low and J. J. Beaudoin, *Cem. Concr. Res.*, 1993, **23**, 1016–1028.
123 M. Diez-Garcia, J. J. Gaitero, J. S. Dolado and C. Aymonier, *Angew. Chem., Int. Ed.*, 2017, **56**, 3162–3167.
124 M. Diez-Garcia, J. J. Gaitero, J. I. Santos, J. S. Dolado and C. Aymonier, *J. Flow Chem.*, 2018, **8**, 89–95.
125 V. Musumeci, G. Goracci, P. Sanz Camacho, J. S. Dolado and C. Aymonier, *Chem. – Eur. J.*, 2021, **27**, 11309–11318.
126 V. Musumeci, University of Bordeaux and University of the Basque Country, 2021.
127 C. Hejny and T. Armbruster, *Z. Kristallogr. - Cryst. Mater.*, 2001, **216**, 396–408.
128 Y. Kudoh and Y. Takéuchi, *Mineral. J.*, 1979, **9**, 349–373.
129 E. Spudulis, V. Šavareika and A. Špokauskas, *Mater. Sci.*, 2013, **19**, 190–196.
130 L. Black, K. Garbev and A. Stumm, *Adv. Appl. Ceram.*, 2009, **108**, 137–144.
131 S. Shaw, S. M. Clark and C. M.-B. Henderson, *Chem. Geology*, 2000, **167**, 129–140.
132 S.-Y. Hong and F. P. Glasser, *Cem. Concr. Res.*, 2004, **34**, 1529–1534.
133 M. R. Hansen, H. J. Jakobsen and J. Skibsted, *Inorg. Chem.*, 2003, **42**, 2368–2377.
134 K. Speakman, *Mineral. Mag.*, 1968, **36**, 1090–1103.
135 S. Merlino, E. Bonaccorsi and T. Armbruster, *Eur. J. Mineral.*, 2001, **13**, 577–590.
136 M. D. Jackson, J. Moon, E. Gotti, R. Taylor, S. R. Chae, M. Kunz, A.-H. Emwas, C. Meral, P. Guttmann, P. Levitz, H.-R. Wenk and P. J.-M. Monteiro, *J. Am. Ceram. Soc.*, 2013, **96**, 2598–2606.
137 S. Merlino, E. Bonaccorsi and T. Armbruster, *Am. Mineral.*, 1999, **84**, 1613–1621.
138 I. G. Richardson, *Cem. Concr. Res.*, 2004, **34**, 1733–1777.
139 S. A.-S. E⁄-Hemaly, T. Mitsuda and H. F.-W. Taylor, *Cem. Concr. Res.*, 1977, **7**, 429–438.
140 X. Huang, D. Jiang and S. Tan, *J. Eur. Ceram. Soc.*, 2003, **23**, 123–126.
141 T. Mitsuda and H. F.-W. Taylor, *Cem. Concr. Res.*, 1975, **5**, 203–209.
142 T. Mitsuda, K. Sasaki and H. Ishida, *J. Am. Ceram. Soc.*, 1992, **75**, 1858–1863.
143 J. Li, W. Zhang, K. Garbev, G. Beuchle and P. J.-M. Monteiro, *Cem. Concr. Res.*, 2020, **136**, 106170.
144 M. Monasterio, J. J. Gaitero, H. Manzano, J. S. Dolado and S. Cerveny, *Langmuir*, 2015, **31**, 4964–4972.
145 G. Land and D. Stephan, *Cem. Concr. Compos.*, 2015, **57**, 64–67.
146 J. J. Thomas, H. M. Jennings and J. J. Chen, *J. Phys. Chem. C*, 2009, **113**, 4327–4334.
147 G. Land and D. Stephan, *Cem. Concr. Compos.*, 2018, **87**, 73–78.
148 U.S. Environmental Protection Agency (USEPA), *Life cycle assessment: Principles and practice*, 2006.
149 Y. Xu, V. Musumeci and C. Aymonier, *React. Chem. Eng.*, 2019, **4**, 2030–2054.
150 M. Tsang, G. Philippot, C. Aymonier and G. Sonnemann, *Green Chem.*, 2016, **18**, 4924–4933.
151 P. Caramazana-González, P. W. Dunne, M. Gimeno-Fabra, M. Zilka, M. Ticha, B. Stieberova, F. Freiberg, J. McKechnie and E. H. Lester, *Green Chem.*, 2017, **19**, 1536–1547.
152 M. P. Tsang, G. Philippot, C. Aymonier and G. Sonnemann, *ACS Sustainable Chem. Eng.*, 2018, **6**, 5142–5151.
153 ISO - ISO 14040:2006 - Environmental management—Life cycle assessment — Principles and framework, **https://www.iso.org/standard/37456.html**, (accessed December 29, 2021).
154 E. Glogic, M. Claverie, M. Jubayed, V. Musumeci, C. Carême, F. Martin, G. Sonnemann and C. Aymonier, *ACS Sustainable Chem. Eng.*, 2021, **9**(49), 16597–16605.
155 D. di Genova, R. A. Brooker, H. M. Mader, J. W.-E. Drewitt, A. Longo, J. Deubener, D. R. Neuville, S. Fanara, O. Shebanova, S. Anzellini, F. Arzilli, E. C. Bamber, L. Hennet, G. la Spina and N. Miyajima, *In situ observation of nanolite growth in volcanic melt: A driving force for explosive eruptions*, 2020, vol. 6.
156 C. B. Murray, D. J. Norris and M. G. Bawendi, *J. Am. Chem. Soc.*, 2002, **115**, 8706–8715.
157 M. P. Boneschanscher, W. H. Evers, J. J. Geuchies, T. Altantzis, B. Goris, F. T. Rabouw, S. A.-P. van Rossum, H. S.-J. van der Zant, L. D.-A. Siebbeles, G. van Tendeloo, I. Swart, J. Hilhorst, A. V. Petukhov, S. Bals and D. Vanmaekelbergh, *Science*, 2014, **344**, 1377–1380.
158 Y. Yin and A. P. Alivisatos, *Nature*, 2005, **437**, 664–670.
159 H. Xie, F. Chen, A. Nie, T. Pu, M. Rehwoldt, D. Yu, M. R. Zachariah, C. Wang, R. Shahbazian-Yassar, J. Li and L. Hu, *Science*, 2018, **1494**, 1489–1494.

160 P. Xie, Y. Yao, Z. Huang, Z. Liu, J. Zhang, T. Li, G. Wang, R. Shahbazian-Yassar, L. Hu and C. Wang, *Nat. Commun.*, 2019, **10**, 4011.
161 J. K. Warren, *Earth-Sci. Rev.*, 2010, **98**, 217–268.
162 S. Lugli, *Encyclopedia Earth Sci. Series*, 2009, 1150–1156.
163 G. Giuliani, L. A. Groat, A. E. Fallick, I. Pignatelli and V. Pardieu, *Minerals*, 2020, **10**, 597.
164 M. G. Kanatzidis, R. Pöttgen and W. Jeitschko, *Angew. Chem., Int. Ed.*, 2005, **44**, 6996–7023.
165 D. E. Bugaris and H. C. zur Loye, *Angew. Chem., Int. Ed.*, 2012, **51**, 3780–3811.
166 **https://www.crct.polymtl.ca/fact/documentation/ftsalt/ftsalt_figs.htm**, accessed May 2022.
167 X. Liu, N. Fechler and M. Antonietti, *Chem. Soc. Rev.*, 2013, **42**, 8237–8265.
168 I. N. González-Jiménez, A. Torres-Pardo, S. Rano, C. Laberty-Robert, J. C. Hernández-Garrido, M. López-Haro, J. J. Calvino, Á. Varela, C. Sanchez, M. Parras, J. M. González-Calbet and D. Portehault, *Mater. Horiz.*, 2018, **5**, 480–485.
169 H. Le Thi N'Goc, L. D.-N. Mouafo, C. Etrillard, A. Torres-Pardo, J.-F. Dayen, S. Rano, G. Rousse, C. Laberty-Robert, J. G. Calbet, M. Drillon, C. Sanchez, B. Doudin and D. Portehault, *Adv. Mater.*, 2017, **29**, 1604745.
170 F. Gonell, C. Sanchez-Sanchez, V. Vivier, C. Laberty-Robert and D. Portehault, *ACS Appl. Nano Mater.*, 2020, **3**, 7482–7489.
171 R. Epherre, E. Duguet, S. Mornet, E. Pollert, S. Louguet, S. Lecommandoux, C. Schatz and G. Goglio, *J. Mater. Chem.*, 2011, **21**, 4393–4401.
172 F. Gonell, C. M. Sanchez-Sanchez, V. Vivier, C. Méthivier, C. Laberty-Robert and D. Portehault, *Chem. Mater.*, 2020, **32**, 4241–4247.
173 F. Gonell, N. Alem, P. Dunne, G. Crochet, P. Beaunier, C. Méthivier, D. Montero, C. Laberty-Robert, B. Doudin and D. Portehault, *ChemNanoMat*, 2019, **5**, 358–363.
174 Y. Mao, S. Banerjee and S. S. Wong, *J. Am. Chem. Soc.*, 2003, **125**, 15718–15719.
175 Y. Mao and S. S. Wong, *Adv. Mater.*, 2005, **17**, 2194–2199.
176 H. Al Raihani, B. Durand, F. Chassagneux, D. H. Kerridge and D. Inman, *J. Mater. Chem.*, 1994, **4**, 1331.
177 F. Gonell, C. Sanchez-Sanchez, V. Vivier, C. Méthivier, C. Laberty-Robert and D. Portehault, *Chem. Mater.*, 2020, **32**, 4241–4247.
178 K. Hyun Yoon, Y. Soo Cho and D. Heon Kangs, *Review Molten salt synthesis of lead-based relaxors*, 1998, vol. 33.
179 G. Huang, X. Du, F. Zhang, D. Yin and L. Wang, *Chem. – Eur. J.*, 2015, **21**, 14140–14145.
180 E. K. Akdogan, R. E. Brennan, M. Allahverdi and A. Safari, *J. Electroceram.*, 2006, **16**, 159–165.
181 H. Zhou, Y. Mao and S. S. Wong, *Chem. Mater.*, 2007, **19**, 5238–5249.
182 A. L. Tiano, A. C. Santulli, C. Koenigsmann, M. Feygenson, M. C. Aronson, R. Harrington, J. B. Parise and S. S. Wong, *Chem. Mater.*, 2011, **23**, 3277–3288.
183 G. Ji, X. Lin, Y. Sun, S. A. Ali Trimizi, H. Su and Y. Du, *CrystEngComm*, 2011, **13**, 6451–6456.
184 X. Wang, K. Huang, L. Yuan, S. Li, W. Ma, Z. Liu and S. Feng, *ACS Appl. Mater. Interfaces*, 2018, **10**, 28219–28231.
185 M. D. Susman, H. N. Pham, A. K. Datye, S. Chinta and J. D. Rimer, *Chem. Mater.*, 2018, **30**, 2641–2650.
186 M. D. Susman, H. N. Pham, X. Zhao, D. H. West, S. Chinta, P. Bollini, A. K. Datye and J. D. Rimer, *Angew. Chem., Int. Ed.*, 2020, **59**, 15119–15123.
187 M. D. Susman, S. Chinta and J. D. Rimer, *Chem. Mater.*, 2021, **33**, 3155–3163.
188 R. Cheula, M. D. Susman, D. H. West, S. Chinta, J. D. Rimer and M. Maestri, *Angew. Chem., Int. Ed.*, 2021, **60**(48), 25391–25396.
189 J. Fu, C. J. Desantis, R. G. Weiner and S. E. Skrabalak, *Chem. Mater.*, 2015, **27**, 1863–1868.
190 A. K.-P. Mann, J. Fu, C. J. Desantis and S. E. Skrabalak, *Chem. Mater.*, 2013, **25**, 1549–1555.
191 S. Li, J. Song, Y. Che, S. Jiao, J. He and B. Yang, *Energy Environ. Mater.*, DOI: **10.1002/EEM2.12339**.
192 X. Huang, L. Jiang, Q. Xu, X. Li and A. He, *RSC Adv.*, 2017, **7**, 41190–41203.
193 X. Huang, L. Xiong and X. Qiu, *CrystEngComm*, 2018, **21**, 182–189.
194 P. Fedorov, M. Mayakova, V. Voronov, A. Baranchikov and V. Ivanov, *J. Fluorine Chem.*, 2019, **218**, 69–75.
195 P. P. Fedorov and A. A. Alexandrov, *J. Fluorine Chem.*, 2019, **227**, 109374.
196 X. Huang, L. Jiang, Q. Xu, X. Li and A. He, *RSC Adv.*, 2017, **7**, 41190–41203.
197 X. Huang, L. Xiong and X. Qiu, *CrystEngComm*, 2018, **21**, 182–189.
198 M. G. Kanatzidis and Y. Park, *J. Am. Chem. Soc.*, 1989, 3767–3769.
199 D. P. Shoemaker, Y.-J. Hu, D. Y. Chung, G. J. Halder, P. J. Chupas, L. Soderholm, J. F. Mitchell and M. G. Kanatzidis, *Proc. Natl. Acad. Sci. U. S. A.*, 2014, **111**, 10922–10927.
200 M. G. Kanatzidis, *Inorg. Chem.*, 2017, **56**, 3158–3173.
201 A. K.-P. Mann, S. Wicker and S. E. Skrabalak, *Adv. Mater.*, 2012, **24**, 6186–6191.
202 H. Jin, Z. Hu, T. Li, L. Huang, J. Wan, G. Xue and J. Zhou, *Adv. Funct. Mater.*, 2019, **29**, 1900649.
203 J. Fu and S. E. Skrabalak, *J. Mater. Chem. A*, 2016, **4**, 8451–8457.
204 R. Kumar, M. Bahri, Y. Song, F. Gonell, C. Thomas, O. Ersen, C. Sanchez, C. Laberty-Robert and D. Portehault, *Nanoscale*, 2020, **12**, 15209–15213.
205 G. Gouget, P. Beaunier, D. Portehault and C. Sanchez, *Faraday Discussions*, 2016, **191**, 511–525.
206 D. Portehault, S. Devi, P. Beaunier, C. Gervais, C. Giordano, C. Sanchez and M. Antonietti, *Angew. Chem., Int. Ed.*, 2011, **50**, 3262–3265.
207 G. Gouget, D. Bregiroux, R. Grosjean, D. Montero, S. Maier, F. Gascoin, C. Sanchez and D. Portehault, *Chem. Mater. Chem. Mater.*, 2021, **33**(6), 2099–2109.
208 J. S. Kanady, P. Leidinger, A. Haas, S. Titlbach, S. Schunk, K. Schierle-Arndt, E. J. Crumlin, C. H. Wu and A. P. Alivisatos, *J. Am. Chem. Soc.*, 2017, **139**, 5672–5675.

209 S. Delacroix, Y. le Godec, C. Coelho-Diogo, C. Gervais, I. Génois, P. le Griel and D. Portehault, *Inorg. Chem.*, 2020, **18**, 2–7.

210 S. Delacroix, F. Igoa, Y. Song, Y. le Godec, C. Coelho-Diogo, C. Gervais, G. Rousse and D. Portehault, *Inorg. Chem.*, 2021, **60**(7), 4252–4260.

211 X. Kan, J. Ding, H. Zhu, C. Deng and C. Yu, *Powder Technol.*, 2017, **315**, 81–86.

212 M. Godfroy, A. Russel, F. Mercier, M. Granier, T. Jarrosson, C. Niebel, F. Serein Spirau, R. Viennois and M. Beaudhuin, *Mater. Lett.*, 2019, **247**, 7–10.

213 V. A. Mukhanov, P. S. Sokolov, Y. le Godec and V. L. Solozhenko, *J. Superhard Mater.*, 2013, **35**, 415–417.

214 Y. Song, I. Gómez-Recio, R. Kumar, C. C. Diogo, S. Casale, I. Génois and D. Portehault, *Dalton Trans.*, 2021, **50**, 16703–16710.

215 Y. Song, S. Casale, A. Miche, D. Montero, C. Laberty-Robert and D. Portehault, *J. Mater. Chem. A*, 2022, **10**, 1350–1358.

216 S. Ning, T. Wen, B. Ye and Y. Chu, *J. Am. Ceram. Soc.*, 2020, **103**, 2244–2251.

217 Z. Pang, X. Zou, S. Li, W. Tang, Q. Xu and X. Lu, *Adv. Eng. Mater.*, 2020, **22**, 1901300.

218 A. Liu, Q. Yang, X. Ren, F. Meng, L. Gao, M. Gao, Y. Yang, T. Ma and G. Wu, *Ceram. Int.*, 2020, **46**, 6934–6939.

219 H. Liu, Y. Wang, L. Yang, R. Liu and C. Zeng, *J. Mater. Sci. Technol.*, 2020, **37**, 77–84.

220 Y. Wang, H. L. Zhang, H. J. Liu and C. L. Zeng, *Mater. Res. Lett.*, 2019, **7**, 361–367.

221 O. Malina, P. Jakubec, J. Kašlík, J. Tuček and R. Zbořil, *Nanoscale*, 2017, **9**, 10440–10446.

222 C. Cao, H. Ling, N. Murali and X. Li, *Materialia*, 2019, **7**, 100425.

223 X. Liu, N. Fechler and M. Antonietti, *Chem. Soc. Rev.*, 2013, **42**, 8237–8265.

224 S. Carenco, D. Portehault, C. Boissière, N. Mézailles and C. Sanchez, *Chem. Rev.*, 2013, **113**, 7981–8065.

225 G. Gouget, D. Debecker, A. Kim, G. Olivieri, J.-J. Gallet, F. Bournel, C. Thomas, O. Ersen, S. Moldovan, C. Sanchez, S. Carenco and D. Portehault, *Inorg. Chem.*, 2017, **56**, 9225–9234.

226 P. R. Jothi, K. Yubuta and B. P.-T. Fokwa, *Adv. Mater.*, 2018, 1704181.

227 J. L. Ma, N. Li, Q. Zhang, X. B. Zhang, J. Wang, K. Li, X. F. Hao and J. M. Yan, *Energy Environ. Sci.*, 2018, **11**, 2833–2838.

228 W. Hong, S. Sun, Y. Kong, Y. Hu and G. Chen, *J. Mater. Chem. A*, 2020, **8**, 7360–7367.

229 J. Lei, S. Hu, C. L. Turner, K. Zeng, M. T. Yeung, J. Yan, R. B. Kaner and S. H. Tolbert, *ACS Nano*, 2019, **13**, 10036–10048.

230 R. Grosjean, Y. le Godec, S. Delacroix, G. Gouget, P. Beaunier, O. Ersen, D. Ihiawakrim, O. Kurakevych, C. Chaneac and D. Portehault, *Dalton Trans.*, 2018, **47**, 7634–7639.

231 S. Khoshsima, Z. Altıntaş, M. Schmidt, M. Bobnar, M. Somer and Ö. Balcı, *J. Alloys Compds.*, 2019, **805**, 471–482.

232 T. M. Mattox, A. Agrawal and D. J. Milliron, *Chem. Mater.*, 2015, **27**, 6620–6624.

233 T. M. Mattox, S. Chockkalingam, I. Roh and J. J. Urban, *J. Phys. Chem. C*, 2016, **120**, 5188–5195.

234 C. Groome, I. Roh, T. M. Mattox and J. J. Urban, *ACS Omega*, 2017, **2**, 2248–2254.

235 M. J. Bojdys, J.-O. Müller, M. Antonietti and A. Thomas, *Chem. – Eur. J.*, 2008, **14**, 8177–8182.

236 G. Zhang, L. Lin, G. Li, Y. Zhang, A. Savateev, S. Zafeiratos, X. Wang and M. Antonietti, *Angew. Chem., Int. Ed.*, 2018, **57**, 9372–9376.

237 X. Liu and M. Antonietti, *Carbon*, 2014, **69**, 460–466.

238 N. Fechler, T.-P. Fellinger and M. Antonietti, *Adv. Mater.*, 2013, **25**, 75–79.

239 X. Liu, M. Antonietti and C. Giordano, *Chem. Mater.*, 2013, **25**, 2021–2027.

240 F. Liang, L. Tian, H. Zhang, F. Liang, S. Liu, R. Cheng and S. Zhang, *RSC Adv.*, 2016, **6**, 68615–68618.

241 W. Lei, D. Portehault, R. Dimova and M. Antonietti, *J. Am. Chem. Soc.*, 2011, **133**, 7121–7127.

242 W. Lei, S. Qin, D. Liu, D. Portehault, Z. Liu and Y. Chen, *Chem. Commun.*, 2013, **49**, 352–354.

243 B. Albert and K. Schmitt, *Chem. Commun.*, 1998, 2373–2374.

244 B. Albert and K. Schmitt, *Chem. Mater.*, 1999, **11**, 3406–3409.

245 H. Zhang, K. Dasbiswas, N. B. Ludwig, G. Han, B. Lee, S. Vaikuntanathan and D. V. Talapin, *Nature*, 2017, **542**, 328–331.

246 V. Srivastava, W. Liu, E. M. Janke, V. Kamysbayev, A. S. Filatov, C. J. Sun, B. Lee, T. Rajh, R. D. Schaller and D. V. Talapin, *Nano Lett.*, 2017, **17**, 2094–2101.

247 V. Srivastava, V. Kamysbayev, L. Hong, E. Dunietz, R. F. Klie and D. V. Talapin, *J. Am. Chem. Soc.*, 2018, **140**, 12144–12151.

248 P. Urbankowski, B. Anasori, T. Makaryan, D. Er, S. Kota, P. L. Walsh, M. Zhao, V. B. Shenoy, M. W. Barsoum and Y. Gogotsi, *Nanoscale*, 2016, **8**, 11385–11391.

249 M. Li, J. Lu, K. Luo, Y. Li, K. Chang, K. Chen, J. Zhou, J. Rosen, L. Hultman, P. Eklund, P. O.-Å. Persson, S. Du, Z. Chai, Z. Huang and Q. Huang, *J. Am. Chem. Soc.*, 2019, **141**, 4730–4737.

250 Y. Li, H. Shao, Z. Lin, J. Lu, L. Liu, B. Duployer, P. O.-Å. Persson, P. Eklund, L. Hultman, M. Li, K. Chen, X. H. Zha, S. Du, P. Rozier, Z. Chai, E. Raymundo-Piñero, P. L. Taberna, P. Simon and Q. Huang, *Nat. Mater.*, 2020, **19**, 894–899.

251 A. Dash, R. Vaßen, O. Guillon and J. Gonzalez-Julian, *Nat. Mater.*, 2019, **18**, 465–470.

252 G. Ma, H. Shao, J. Xu, Y. Liu, Q. Huang, P.-L. Taberna, P. Simon and Z. Lin, *Nat. Commun.*, 2021, **12**, 5085.

253 V. Kamysbayev, A. S. Filatov, H. Hu, X. Rui, F. Lagunas, D. Wang, R. F. Klie and D. V. Talapin, *Science*, 2020, **369**, 979–983.

254 J. M. Garber, S. Maurya, J.-A. Hernandez, M. S. Duncan, L. Zeng, H. L. Zhang, U. Faul, C. McCammon, J.-P. Montagner, L. Moresi, B. A. Romanowicz, R. L. Rudnick

and L. Stixrude, *Geochem., Geophys., Geosyst.*, 2018, **19**, 2062–2086.
255 R. Dasgupta and M. M. Hirschmann, *Nature*, 2006, **440**, 659–662.
256 F. P. Bundy, H. T. Hall, H. M. Strong and R. H. Wentorfjun, *Nature*, 1955, **176**, 51–55.
257 E. Snider, N. Dasenbrock-Gammon, R. McBride, M. Debessai, H. Vindana, K. Vencatasamy, K. V. Lawler, A. Salamat and R. P. Dias, *Nature*, 2020, **586**, 373–377.
258 D. Laniel, G. Weck, G. Gaiffe, G. Garbarino and P. Loubeyre, *J. Phys. Chem. Lett.*, 2018, **9**, 1600–1604.
259 E. Horvath-Bordon, R. Riedel, P. F. McMillan, P. Kroll, G. Miehe, P. A. van Aken, A. Zerr, P. Hoppe, O. Shebanova and I. McLaren, *Angew. Chem.*, 2007, **119**, 1498–1502.
260 G. Fiquet, A. L. Auzende, J. Siebert, A. Corgne, H. Bureau, H. Ozawa and G. Garbarino, *Science*, 2010, **329**, 1516–1518.
261 M. A. Baron, O. T. Lord, R. Myhill, A. R. Thomson, W. Wang, R. G. Trønnes and M. J. Walter, *Earth Planet. Sci. Lett.*, 2017, **472**, 186–196.
262 S. Anzellini and S. Boccato, *Crystals*, 2020, **10**, 459.
263 H. Huppertz, *Z. Kristallogr. - Cryst. Mater.*, 2004, **219**, 330–338.
264 R. C. Liebermann, *High Pressure Res.*, 2011, **31**, 493–532.
265 J. M. Besson, R. J. Nelmes, G. Hamel, J. S. Loveday, G. Weill and S. Hull, *Phys. B*, 1992, **180**, 907–910.
266 Y. le Godec, M. T. Dove, S. A.-T. Redfern, M. G. Tucker, W. G. Marshall, G. Syfosse and J.-M. Besson, *High Pressure Res.*, 2001, **21**, 263–280.
267 M. Mezouar, T. le Bihan, H. Libotte, Y. le Godec and D. Häusermann, *J. Synchrotron Radiat.*, 1999, **6**, 1115–1119.
268 Y. le Godec, G. Hamel, V. L. Solozhenko, D. Martinez-Garcia, J. Philippe, T. Hammouda, M. Mezouar, W. A. Crichton, G. Morard and S. Klotz, *J. Synchrotron Radiat.*, 2009, **16**, 513–523.
269 F. R. Boyd and J. L. England, *J. Geophys. Res.*, 1960, **65**, 741–748.
270 M. A. Baron, R. Stalder, J. Konzett and C. A. Hauzenberger, *Phys. Chem. Miner.*, 2015, **1**, 53–62.
271 G. Morard, M. Mezouar, S. Bauchau, M. Álvarez-Murga, J.-L. Hodeau and G. Garbarino, *Rev. Sci. Instrum.*, 2011, **82**, 23904.
272 Y. Wang, T. Uchida, R. von Dreele, M. L. Rivers, N. Nishiyama, K. Ichi Funakoshi, A. Nozawa and H. Kaneko, *J. Appl. Crystallogr.*, 2004, **37**, 947–956.
273 Y. le Godec, A. Courac and V. L. Solozhenko, *J. Appl. Phys.*, 2019, **126**, 151102.
274 P. F. McMillan, *Nat. Mater.*, 2002, **1**, 19–25.
275 E. Gilioli and L. Ehm, *IUCrJ*, 2014, **1**, 590–603.
276 A. R. Oganov, J. Chen, C. Gatti, Y. Ma, Y. Ma, C. W. Glass, Z. Liu, T. Yu, O. O. Kurakevych and V. L. Solozhenko, *Nature*, 2009, **457**, 863–867.
277 V. L. Solozhenko, O. O. Kurakevych, D. Andrault, Y. le Godec and M. Mezouar, *Phys. Rev. Lett.*, 2009, **102**, 15506.
278 T. Irifune, A. Kurio, S. Sakamoto, T. Inoue and H. Sumiya, *Nature*, 2003, **421**, 599–601.
279 Q. Huang, D. Yu, B. Xu, W. Hu, Y. Ma, Y. Wang, Z. Zhao, B. Wen, J. He and Z. Liu, *Nature*, 2014, **510**, 250–253.
280 V. L. Solozhenko, O. O. Kurakevych and Y. Le Godec, *Adv. Mater.*, 2012, **24**, 1540–1544.
281 Y. Tian, B. Xu, D. Yu, Y. Ma, Y. Wang, Y. Jiang, W. Hu, C. Tang, Y. Gao, K. Luo, Z. Zhao, L.-M. Wang, B. Wen, J. He and Z. Liu, *Nature*, 2013, **493**, 385–388.
282 N. J. Petch, *J. Iron Steel Inst.*, 1953, **174**, 25.
283 A. Nagakubo, H. Ogi, H. Sumiya and M. Hirao, *Appl. Phys. Lett.*, 2014, **105**, 081906.
284 L. Fang, H. Ohfuji and T. Irifune, *J. Nanomater.*, 2013, 201845.
285 C.-Q. Jin, X.-J. Wu, P. Laffez, T. Tatsuki, T. Tamura, S. Adachi, H. Yamauchi, N. Koshizuka and S. Tanaka, *Nature*, 1995, **375**, 301–303.
286 S. M. Clarke, M. Amsler, J. P.-S. Walsh, T. Yu, Y. Wang, Y. Meng, S. D. Jacobsen, C. Wolverton and D. E. Freedman, *Chem. Mater.*, 2017, **29**, 5276–5285.
287 P. M. Shirage, K. Miyazawa, M. Ishikado, K. Kihou, C. H. Lee, N. Takeshita, H. Matsuhata, R. Kumai, Y. Tomioka, T. Ito, H. Kito, H. Eisaki, S. Shamoto and A. Iyo, *Phys. C*, 2009, **469**, 355–369.
288 H. Hosono and S. Matsuishi, *Curr. Opin. Solid State Mater. Sci.*, 2013, **17**, 49–58.
289 M. J. Lipp, W. J. Evans, B. J. Baer and C.-S. Yoo, *Nat. Mater.*, 2005, **4**, 211–215.
290 A. Aimi, T. Katsumata, D. Mori, D. Fu, M. Itoh, T. Kyomen, K. Hiraki, T. Takahashi and Y. Inaguma, *Inorg. Chem.*, 2011, **50**, 6392–6398.
291 A. A. Belik, D. A. Rusakov, T. Furubayashi and E. Takayama-Muromachi, *Chem. Mater.*, 2012, **24**, 3056–3064.
292 O. O. Kurakevych, Y. le Godec, W. A. Crichton, J. Guignard, T. A. Strobel, H. Zhang, H. Liu, C. Coelho Diogo, A. Polian and N. Menguy, *Inorg. Chem.*, 2016, **55**, 8943–8950.
293 H. Zhang, H. Liu, K. Wei, O. O. Kurakevych, Y. le Godec, Z. Liu, J. Martin, M. Guerrette, G. S. Nolas and T. A. Strobel, *Phys. Rev. Lett.*, 2017, **118**, 146601.
294 Z. Jouini, O. O. Kurakevych, H. Moutaabbid, Y. le Godec, M. Mezouar and N. Guignot, *J. Superhard Mater.*, 2016, **38**, 66–70.
295 M. Guerette, M. D. Ward, K. A. Lokshin, A. T. Wong, H. Zhang, S. Stefanoski, O. Kurakevych, Y. le Godec, S. J. Juhl and N. Alem, *Cryst. Growth Des.*, 2018, **18**, 7410–7418.
296 B. Sun, X. Jia, J. Zhao, Y. Li, H. Liu and H. Ma, *Inorg. Chem.*, 2018, **57**, 3323–3328.
297 Y. Jiang, X. Jia and H. Ma, *Mod. Phys. Lett. B*, 2017, **31**, 1750261.
298 R. Grosjean, Y. le Godec, S. Delacroix, G. Gouget, P. Beaunier, O. Ersen, D. Ihiawakrim, O. O. Kurakevych, C. Chanéac and D. Portehault, *Dalton Trans.*, 2018, **47**, 7634–7639.
299 Z. Wang, O. Kononova, K. Cruse, T. He, H. Huo, Y. Fei, Y. Zeng, Y. Sun, Z. Cai, W. Sun and G. Ceder, 2021, arXiv:2111.10874.
300 A. Navrotsky and K. Lilova, *ACS Earth Space Chem.*, 2021, **5**, 1812.

301 D. R. Neuville, L. Hennet, P. Florian and D. de Ligny, *Rev. Mineral. Geochem.*, 2014, **78**, 779–800.
302 C. Crouzet, F. Brunet, N. Recham, A. L. Auzende, N. Findling, V. Magnin, J. H. Ferrasse and B. Goffé, *Front. Earth Sci.*, 2017, **5**, 86.
303 T. Voisin, A. Erriguible and C. Aymonier, *Sci. Adv.*, 2020, **5**, eaaz7770.
304 M. Yamamoto, R. Nakamura and K. Takai, *ChemElectroChem*, 2018, **5**, 2162.
305 M. F. Hochella, S. K. Lower, P. A. Maurice, R. L. Penn, N. Sahai, D. L. Sparks and B. S. Twining, *Science*, 2008, **319**, 1631–1635.
306 M. A. Carabello, F. M. Michell and M. F. Hochella Jr, *Am. Mineral.*, 2015, **100**, 14–25.